Bimetallic core@shell nanostructures of galvanic metals for improved catalysis

Thesis submitted for the award of degree of

Doctor of Philosophy

Submitted by:

Aadil Bathla
(Regn. No. 901609016)

Under the Supervision of

Dr. Bonamali Pal
Professor

SCHOOL OF CHEMISTRY AND BIOCHEMISTRY
THAPAR INSTITUTE OF ENGINEERING AND TECHNOLOGY
PATIALA-147004

Certificate

This is to certify that the work embodied in this thesis entitled "**Bimetallic core@shell nanostructures of galvanic metals for improved catalysis**" has been carried out by Mr. Aadil Bathla under my supervision and guidance in the School of Chemistry and Biochemistry, Thapar Institute of Engineering and Technology, Patiala. The candidate completed all the conditions required for the fulfillment of the award of the Degree of Philosophy.

I also certified that the work represented in this thesis is original and has not been submitted in part or full for the award of any degree in any other University or Institute.

Dr. Bonamali Pal
Professor and Supervisor
School of Chemistry and Biochemistry
Thapar Institute of Engineering and Technology
Patiala-147004

Dr. Amjad Ali 18/06/2020
Professor and Head
School of Chemistry and Biochemistry
Thapar Institute of Engineering and Technology
Patiala-147004

Candidate's Declaration

I, hereby declare that the work presented in the thesis entitled **"Bimetallic core@shell nanostructures of galvanic metals for improved catalysis"**, in fulfillment of the requirement for the award of the Degree of Doctor of Philosophy, School of Chemistry and Biochemistry, Thapar Institute of Engineering and Technology, Patiala, is an authentic record of my own work carried out under the supervision of Dr. Bonamali Pal, Professor and Former Head, School of Chemistry and Biochemistry, Thapar Institute of Engineering and Technology, Patiala, India. The matter embodied in this thesis has not been submitted in part or full to any other university or institute for the award of any degree in India or Abroad.

Aadil Bathla

Aadil Bathla

Dr. Bonamali Pal
Professor and Supervisor
School of Chemistry and Biochemistry
Thapar Institute of Engineering and Technology
Patiala-147004

Dedicated

To

My Father

Acknowledgement

The completion of this thesis would not have been possible without the support and encouragement of several special people. Hence, I would like to take this opportunity to show my gratitude to those who have assisted me in a myriad of ways.

I would first like to express my heartfelt thanks to my research supervisor **Dr. Bonamali Pal, Professor**. A more supportive and considerate supervisor, I couldn't have wished for. He convincingly guided and encouraged me to be professional and do the right thing even when the road got tough. He was prepared to sit and listen to my troubles and always made me feel as if my work mattered. Without his persistent help, the goal of this project would not have been realized. I would also like to thank **Dr. Satnam Singh, Professor** who helped and directed me on the right path with his valuable suggestions. My sincere thanks also go to **Mr. Chander Thakur**, and office staff **Mr. Mayank** for their cooperation, support, and help.

I sincerely acknowledge the **Department of Science and Technology (DST)**, Dean R & SP **Dr. Rafat Siddique**, and TIET, Patiala for providing financial support.

I wish to express my sincere appreciation to **Dr. Amjad Ali**, Professor, and Head, School of Chemistry and Biochemistry, Thapar Institute of Engineering and Technology, Patiala. I would also like to thank my doctoral committee experts **Dr. Vijay Luxami**, **Dr. Davinder Kumar**, and **Dr. Bhaskar Chandra Mohanty** who were involved in the validation survey for this research project. Their fruitful suggestions and endless encouragement help me to represent my research work in a better way.

I would like to thanks my seniors **Dr. Rayees Ahmad Rather**, **Dr. Yuvraj Garg, Dr. Amit Mishra, Mr. Gulshan Kumar, Mr. Santosh Kumar Rath, Dr. Vagish Dwibedi,** and **Dr. Nandan Sarkar** for their knowledgeable help and also thankful to my collogues **Mrs. Smriti Thakur, Mrs. Sakshi Bhardwaj, Manpreet Kaur Aulkh, Vanshita Goel, Pawandeep Kaur, Shagun Kainth, Ruby Priya** and **Shivali Gupta**. Special thanks to my hostel mates **Piyush Sharma, Davinder Maan, Devendra Sillu, Ashok Thakur, Arun Rana, Ajay Sharma,** and **Kaushlendra Pandey** for their precious friendship and for making this journey easier.

The help from different institutes and laboratories like SAI Lab TIET, Punjab University Chandigarh, NIPER Mohali, IISER Mohali, Sprint testing solutions Mumbai, etc. are highly acknowledged.

I can't put my thoughts or feelings into words to show my heartfelt gratitude to my father **Mr. Raj Kumar Bathla**. He encouraged me to set my dreams and work hard to make them true. Though he is not physically present here but emotionally he is always with me and his thoughts gave me the strength to face every tough situation. I wish I could convey how much it means to me having you all here, but words fail me at the moment. One strong person who comes in my life is my mother **Mrs. Shashi Kanta**. She has been a constant source of support and encouragement and has made an untold number of sacrifices for the entire family and especially for me. She is a great inspiration for me.

Word fails to express my gratitude from the depth of my heart for my loving brother **Mr. Abhinav Bathla**, sister-in-law **Mrs. Alisha Grover**, my sweet Lill girl **Shanvi Bathla** and all family members who provided me relentless encouragement, prayer, pure love, and unmatched affection that made this work to reach this destination.

Besides this, I am thankful to the persons who knowingly and unknowingly helped me during the successful completion of this work.

Aadil Bathla

Aadil Bathla

Table of Contents

CHAPTER- 2

UV-light responsive selective hydrogenation of carbonyl compounds using bimetallic Pd@Ni-mesoporous TiO_2 nanocatalyst

CHAPTER- 3

Enhanced co-catalysis of bimetallic Cu(core)@Zn(shell) imparted to (001) faceted TiO_2 for selective quinoline hydrogenation

CHAPTER- 4

Photocatalytic vs. catalytic hydrogenation of industrially important unsaturated aldehydes using Pd(core)@Au(shell)/TiO_2 nanostructure

List of Abbreviations

a.u.	Arbitrary unit
APT	Pd@Au-TiO_2
BET	Brunauer Emmett Teller
BJH	Barrett-Joyner-Halenda
CB	Conduction band
CAL	Cinnamaldehyde
COAL	Crotonaldehyde
DI	Deionizer
DRS	Diffuse reflectance spectroscopy
EDS	Energy dispersive X-ray specroscopy
FESEM	Field emission scanning electron microscopy
GC-MS	Gas chromatography-Mass spectroscopy
GC-FID	Gas chromatography-Flame Ionization Detector
4-HBZ	4-hydroxybenzaldehyde
HPLC	High pressure liquid chromatography
HRTEM	High resolution transmission electron microscopy
8-HTHQ	1,2,3,4-tetrahydroquino-8-ol
8-HQu	8-hydroxyquinoline
IPA	Isopropyl alcohol
JCPDS	Joint committee on powder diffraction standards
L	Length
M	Metal
mL	Milli-litre
mM	Milli molar
Mol	Mole
8-MTHQ	8-methyl-1,2,3,4-tetrahydroquinoline
8-MQu	8-methylquinoline
mTiO_2	Mesoporous-TiO_2

4-NBZ	4-nitrobenzaldehyde
Nm	Nanometre
NPs	Nanoparticles
NSs	Nanosheets
NS	Nanosphere
PL	Photoluminescence
PNT	Pd@Ni-TiO_2
P25	Commercially available-TiO_2
PVP	Polyvinylpyrrolidone
RT	Room temperature
SAED	Selected area electron diffraction
SEM	Scanning electron microscopy
SPR	Surface plasmon resonance
STEM	Scanning transmission electron microscopy
TEM	Transmission electron microscopy
TGA	Thermogravimetric analysis
UV	Ultraviolet
µl	Micro-liter
µM	Micro molar
VB	Valance band
Vis	Visible
wt%	Weight percentage
XPS	X-ray photoelectron spectroscopy
XRD	X-ray diffraction spectroscopy
ZCT	Cu@Zn-TiO_2

List of Symbols

e^-	Electron
h^+	Hole
$OH^\cdot$	Hydroxyl radical
E_g	Band gap
Å	Angstrom
α	Absorption coefficient
A	Absorbance
°	Degree
λ	Wavelength
%	Percentage
μ	Micro
Ɵ	Theta
H	Hour
Φ	Work function
E_o	Electrode potential
m	Meter
g	Gram
mg	Milligram
Ef	Fermi energy
V	Volt
d	Distance
s	Second
C	Concentration
ν	Frequency
μmol	Micromol

Abstracts

Chapter-1

This chapter describes the brief introduction and importance of bimetallic nanoparticles over the monometallic counterparts. The role of reduction potential values in the synthesis of bimetallic core@shell nanostructure via galvanic displacement reaction and synergistic interactions between the two different metals is systematically explained in this chapter. Moreover, significance of bimetallic-TiO_2 nanocomposites in the selective hydrogenation of different unsaturated compounds and methodology used for the accomplishment of proposed objective has been discussed.

Chapter-2

This chapter deals with the formation of bimetallic Pd@Ni core-shell nanostructure where Pd serves as a core and Ni serves as a shell. Three different types of bimetallic Pd@Ni were formed by varying the weight ratio of Pd and keeping the amount of Ni constant (Pd:Ni 1:1, 2:1, and 3:1). The as-prepared nanocatalysts were examined for the catalytic and photocatalytic hydrogenation of benzaldehydes compared to their monometallic analogues. The co-catalytic activity was determined by impregnation of bimetallic Pd@Ni nanostructure (having different Pd:Ni weight ratio) on the surface of pre-synthesized mesoporous titanium dioxide ($mTiO_2$) and abbreviated as PNT-1 ($Pd_1@Ni_1$-TiO_2), PNT-2 ($Pd_2@Ni_1$-TiO_2), and PNT-3 ($Pd_3@Ni_1$-TiO_2) respectively. The deposition of mono and bimetallic nanocatalyst on the surface of TiO_2 leads to several modifications. The bimetallic PNT-3 ($Pd_3@Ni_1/mTiO_2$) displayed large surface area (212 m^2g^{-1}), low-recombination rate of the electron and hole pairs and exhibted distinctive properties as compared to their corresponding monometallic (Pd and Ni) analogues. The hydrogenation reaction was analyzed under UV-light irradiation and also in the dark with continuous flow of hydrogen. Kinetic measurements revealed that under UV-light radiation synthesized bimetallic PNT-3 photocatalyst displays higher rate constant $k = 5.31 \times 10^{-1}$ h^{-1} for the selective hydrogenation than its monometallic analogues. The superior activity of bimetallic composites occurs due to the reduction in the barrier height (decrease in work function) which leads to efficient transfer of electron at the bimetallic/$mTiO_2$ interface.

Chapter-3

Bimetallic nanostructures have gained immense importance owing to their enhanced co-catalytic effect in improving photocatalytic activity of TiO_2 for various applications relative to monometallic ones. However, the use of bimetallic core@shell catalyst/nanocatalyst for hydrogenation of important industrial organic compounds is not much explored relative to conventional metal catalysts. In this respect, the present study demonstrated the synthesis of core@shell (Cu@Zn) nanostructure based on their galvanic interactions. TEM analysis confirmed the formation of Cu@Zn nanoparticles with a shell thickness of 195 nm. It was observed that with increasing Cu:Zn weight ratio (1:1, 2:1, and 3:1) the average hydrodynamic size increases from 198 to 267 nm. These Cu@Zn nanostructures showed superior co-catalytic activity after impregnation on (001) faceted titanium nanosheets (surface area = 73 m^2g^{-1}) for the selective hydrogenation of quinoline under visible light radiation. The optimized Cu@Zn(3:1)/TiO_2 photocatalyst showed enhanced conversion, selectivity, and higher rate constant ($k = 2.1 \times 10^{-1}h^{-1}$) compared to Cu and Zn-$TiO_2$ nanocomposites. The superior activity of Cu@Zn-TiO_2 photocatalyst was attributed to the synergistic interaction occurring at bimetallic-TiO_2 interface which effectively promotes the transfer of electron and hydride ion (H^-) for quinoline hydrogenation. The conventional hydrogenation of quinoline required high temperature, solvents, expensive bases and involved multistep procedure. Therefore, the use of Cu@Zn-TiO_2 photocatalyst might be a greener approach for the selective hydrogenation of industrial important unsaturated organic compounds under visible light radiation.

Chapter-4

In this chapter, Pd@Au core-shell supported TiO_2 nanostructures were synthesized via galvanic replacement reaction and were examined for their catalytic/ photocatalytic activities. Three different types of bimetallic Pd@Au nanostructure were synthesized by varying Pd:Au weight ratio i.e. (1:1), (1:2) and (1:3). DLS measurements revealed that with increasing Au weight ratio, the hydrodynamic size increased from 126 to 157 nm. The co-existence of absorption characteristic of Pd and Au in the UV-Visible spectra suggests the successful synthesis of bimetallic nanostructure. STEM and EDS mapping further confirmed the formation of Pd@Au nanostructure with inner Pd core and outer Au shell. Bimetallic Pd@Au nanocatalyst displayed superior activity and selectivity for the cinnamaldehyde hydrogenation than monometallic

analogues. However, when Pd@Au nanostructures were utilized as co-catalyst after impregnation on the surface of TiO_2, a significant improvement in the hydrogenation reaction was observed under solar radiation relative to catalytic conditions. The photocatalytic performance of Pd@Au-TiO_2 was found to be varied as a function of shell thickness and the optimized APT-2 (Pd_1@Au_2-TiO_2) photocatalyst exhibited higher rate constant (2.3×10^{-1} $h^{-1)}$ for cinnamaldehyde hydrogenation. The co-catalytic effect of Pd@Au at bimetallic-TiO_2 hetero-junction effectively migrate the electrons and hydride ions for hydrogenation reaction.

CHAPTER- 1

Introduction and literature review

Section-A

1.1 Introduction

1.1.1 Transition metal nanocatalysis

Transition metal nanoparticles have achieved remarkable attention as catalysts for a variety of organic and inorganic reactions such as oxidation, reduction, cross-coupling, electron transfer, and hydrogenation reactions [1-5]. The superior catalytic performance of these nanoparticles is attributed to their small size and higher surface to volume ratio relative to their bulk parent materials [6, 7]. Metal nanoparticles displayed superior shape and size dependent properties. Therefore, the percentage yield and selectivity of industrially important reactions can be achieved by modifying the size and morphology of the nanoparticles. Suchomel *et al.* [8] reported the synthesis of Au nanoparticles in the size range of 6-22 nm. It was observed that smaller size Au nanoparticles exhibited higher activity and selectivity for the reduction of 4-nitrophenol. Mondal *et al.* [9] reported the fabrication of Pd nanoparticles in a porous organic polymer (POP) for catalytic hydrogenation of alkenes. It was found that the POP supported Pd nanoparticles having size 8 nm showed superior catalytic activity for alkene hydrogenation at room temperature. Similarly, Bathla *et al.* [10] studied size dependent catalytic activity of Polyvinylpyrrolidone (PVP) caped three different sized Ni nanoparticles. It was observed that nickel nanoparticles with small size exhibited higher activity for C-C cross coupling and selective hydrogenation of unsaturated aldehydes. Won *et al.* [11] reported the formation of different shaped gold nanoparticles i.e. Au-nanorods (Au-NRs) and Au-nanospheres (Au-NSs). It was found that Au-NRs show higher sensitivity for hydrogen peroxide detection than Au-NSs. Helmlinger *et al.* [12] examined the influence of silver nanoparticle morphology like nanospheres, nanoplatelets, nanocubes and nanorods on the antibacterial activities. Similarly, Xu *et al.* [13] studied the effect of different shape Ag nanoparticles for the oxidation of styrene and observed that {100} faceted Ag nanocubes display 14 times higher catalytic activity than nanospheres and nanoplates. Moreover, metal nanoparticles were also employed as co-catalyst after impregnation on the surface of the semiconductors for various photocatalytic applications.

Gogoi *et al.* [14] reported Ag-TiO_2 as an effective photocatalyst for hydrogen production through water splitting reaction. Wang *et al.* [15] examined the photocatalytic reduction of CO_2 to methane using Au-TiO_2 plasmonic heterojunction. Deng *et al.* [16] reported the synthesis of Ni nanoparticles loaded onto nitrogen doped graphitic carbon nitride (g-C_3N_4) for efficient hydrogen evolution reaction (HER) under light radiation. Kenna *et al.* [17] reported that sulfide modified Pd-TiO_2 catalyst exhibited superior activity and selectivity for the acetylene hydrogenation.

1.1.2 Importance of bimetallic nanostructure over monometallic

In spite of the large number of catalytic applications, a single metal nanocatalyst is not able to accomplish the activity and selectivity requirements for the reactions. These specific properties of metal nanoparticles can be improved by depositing another metal on the surface of first metal. Bimetallic nanostructures are a new class of materials, which are composed of two different metals and would exhibit a combination of the properties originated from two different metals. The incorporation of one metal over another not only improves the functionality, stability and dispersibility, but also reduces the consumption of expensive material. Various physiochemical and optical properties of bimetallic nanostructure can be modified by varying size, shape and composition of bimetallic nanoparticles. The bimetallic nanostructures can have various architectures including alloy, nanowires, dendrite, and core-shell etc. In recent years, bimetallic core-shell nanocomposites consisting of two different metals (Au@Ag, Ag@Au, Pd@Ni, Au@Cu, Pd@Cu, Au@Pd) have gained considerable attention in the area of catalysis [18, 19]. These nanocatalysts exhibit distinctive electronic and chemical properties compared to their parent metals. The improvement in their catalytic performance arise due to (i) the electronic or ligand effect [20, 21] in which charge transfer occurs **(Scheme-1.1)** between two different metals resulting in the modification of electronic properties of the first metal.

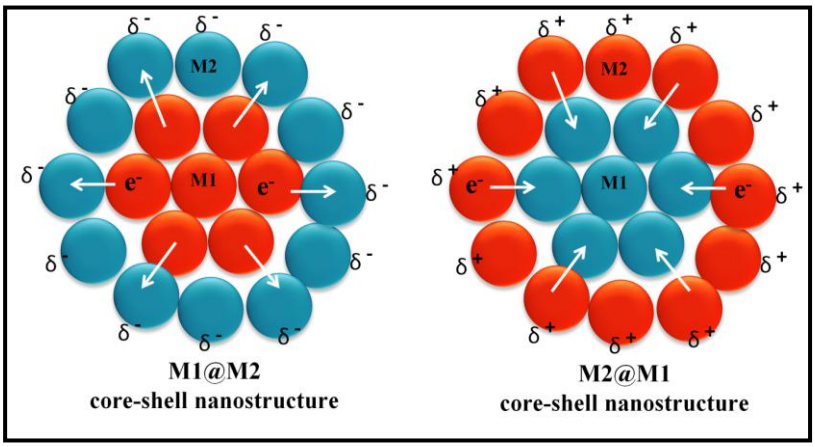

Scheme-1.1: Interfacial charge transfer process in bimetallic core@shell and inverse core@shell nanostructures.

(ii) an ensemble or geometric effect [22] in which addition of second metal on the surface of first metal provides new surface active sites (iii) each metal element promotes different elementary reaction steps resulting to a bi-functional mechanism. Monga *et al.* [23] explored the effect of shapes of bimetallic Au@Ag nanostructures resulting in superior photo-activity for the nitro aromatic reduction than the monometallic counterparts. Hong *et al.* [24] reported that bimetallic Au-Pd supported on SBA-15 displayed superior catalytic activity for the benzyl alcohol oxidation than monometallic (Au and Pd) nanocomposites. Thanh *et al.* [25] reported that CuAg@Ag core-shell nanostructure supported over graphene nanosheet displayed superior activity for the oxygen reduction reaction (ORR) in basic medium. The synergistic interaction between CuAg@Ag and graphene nanosheet made such a unique nanocatalyst that displayed comparable catalytic activity with the commercial available Pt/C catalyst. Haldar *et al.* [26] synthesized Au@Ag core-shell nanostructure for the catalytic reduction of 4-nitrophenol to 4-aminophenol. It was observed that the catalytic efficiency varied by varying the size of core. Vysakh *et al.* [27] reported the synthesis of Au@Ni core-shell nanostructure and observed that bimetallic nanocatalyst having nickel shell (1-2 nm) and Au core (6-10 nm) exhibited higher catalytic activity for the hydrogenation of p-nitrophenol in comparison to monometallic Au and Ni nanoparticles. Monga *et al.* [28] studied the co-catalytic activity of bimetallic core-shell and inverse core-shell structure of Ag and Cu impregnated over TiO_2 for the photo-oxidation and photo-reduction activity relative to monometallic counterparts. Wang *et al.* [29] reported the synthesis of Au@Pd supported on SiO_2 for the selective oxidation of benzyl alcohol. Ma *et al.* [30] reported that the bimetallic Cu-Pd nanocatalyst is highly effective catalyst for the electroreduction of CO_2 to hydrocarbons. Bustamante *et al.* studied the comparative catalytic activity of mono and bimetallic Cu-Ni nanoparticles for the water gas shift reaction. It was observed that bimetallic Cu-Ni nanocatalyst was more active and displayed enhanced stability for the number of catalytic cycles relative to monometallic ones. Liao *et al.* [31] reported Pd@Zn core-shell nanostructure for the hydrogenation of CO_2 via low pressure methanol route.

1.1.3 Galvanic displacement method

Various methods like photochemical, successive reduction, template synthesis, potentiostatic, electrochemical deposition, and two-step reduction have been employed to synthesize core-shell nanostructures [18, 32-36]. These methods resulted in the formation of alloy and other hetero-nanostructures like alloy, dumbbell, and hollow core-shell nanostructure.

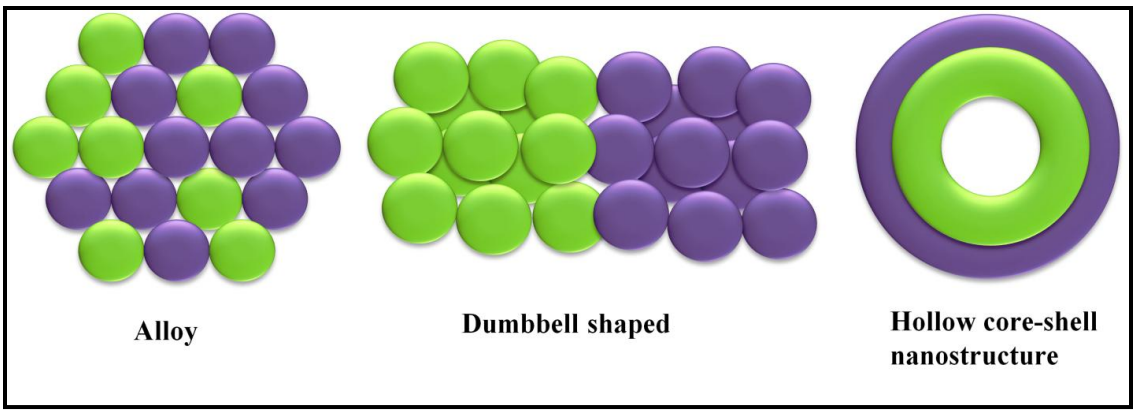

Scheme-1.2: Different shapes of bimetallic nanostructures.

However, the co-reduction method based on galvanic displacement reaction is widely employed for the synthesis of core-shell nanostructures [37]. In this case, two metallic precursors are added simultaneously and the reduction potentials of metals played a significant role in determining the final structural design. Metals having dissimilar reduction potentials are reduced in a consecutive manner in the presence of suitable reducing agent (ascorbic acid, hydrazine, sodium borohydride etc.). Metal ions with more positive reduction potential tend to be reduced at a faster rate and serve as a core whereas metal with lower potential are reduced later and make a shell over the core metal nanoparticles leading to the formation of core-shell nanostructure [38]. The reduction potential value of different metals with standard hydrogen electrode is given as

Oxidized form		Reduced form	E^0 (V)
$Zn^{2+} + 2e^-$	⟶	Zn	**-0.76**
$Ni^{2+} + 2e^-$	⟶	Ni	**-0.26**
$H^+ + e^-$	⟶	$1/2\ H_2$	**0.00**
$Cu^{2+} + 2e^-$	⟶	Cu	**+0.34**
$Ag^+ + e^-$	⟶	Ag	**+0.80**
$Pd^{2+} + 2e^-$	⟶	Pd	**+0.91**
$Au^{3+} + 3e^-$	⟶	Au	**+1.50**

vs. E^0 (SHE) ↓

Jiang *et al*. [39] reported the formation of Au@Ag core-shell nanostructure by galvanic interaction caused by the difference in reduction potentials of the two soluble metal salts ($E^0_{Ag^+/Ag}$ = +0.80 eV Vs SHE; $E^0_{Au^{3+}/Au}$ = +0.93 eV Vs SHE). Fu et *al.* [40] studied the galvanic

interaction between Au and Pd metal ions leading to the formation of Au@Pd core-shell nanostructure based on their reduction potential ($E^0_{Au^{2+}/Au}$ = +1.42 eV Vs SHE; $E^0_{Pd^{2+}/Pd}$ = +0.91 eV Vs SHE). Wu *et al.* [41] reported the synthesis of bimetallic Cu@Pt nanostructure by galvanic replacement reaction and observed that Cu@Pt display superior performance for oxygen reduction reaction relative to monometallic counterparts. Yang *et al.* demonstrated the formation of Ag@Au core-shell nanocubes via galvanic replacement reaction between $AgNO_3$ and $HAuCl_4$ and studied for its enhanced SERS activity [42].

1.1.4 Bimetallic-TiO_2 photocatalysis

Bimetallic nanoparticles are widely employed as co-catalyst for various organic transformations like hydrogenation of alkenes, alkynes, ketones and aldehydes [43-45]. The deposited monometallic/bimetallic nanoparticles act as a photo-sensitizer and enhance the charge transfer process from the conduction band of the semiconductor to the surface of metal nanoparticle (NP). Therefore, metal/semiconductor hetero-junction becomes a key factor for making a highly active photocatalyst. Out of various semiconductors, titanium dioxide (TiO_2) is an effective, non-toxic, highly stable, promising semiconductor material and capture huge attention in the area of photocatalysis and other organic transformation reactions like oxygen reduction reaction, hydrogenation of carbonyl compounds, and different biological activities [46-49]. The major drawback regarding the titanium dioxide is a wide energy band gap (3.2 eV) which limits its photocatalytic activity under visible light radiation. Efforts have been made to fabricate the complex M-TiO_2 catalytic system containing different plasmonic metals (Cu, Au, etc.) that effectively activate and improve the photocatalytic activity of TiO_2 under visible light irradiation. Shiraishi *et al*. [50] reported the photocatalytic production of hydrogen peroxide from ethanol using Au-Ag bimetallic loaded TiO_2 photocatalyst. Monga *et al.* [51] reported the formation of core-shell and inverse core-shell of Cu and Au deposited on TiO_2 for photocatalytic reduction of nitro-aromatics under visible light radiation. Crake *et al.* [52] reported the gas phase photoreduction of CO_2 using TiO_2/C_3N_4 nanocomposite under UV-Visible light radiation. Similarly, Rather *et al.* [53] reported the sunlight driven photocatalytic hydrogen evolution from water using Au-Pt loaded TiO_2 nanosheets. The superior catalytic/photocatalytic activity of bimetallic nanocomposites relative to monometallic ones arise due to shifting in their work function and enhancement in the life time of charge carriers which promotes efficient charge transfer from the CB of TiO_2 and enriches the electron density over the M1@M2 reaction active

center. **Scheme-1.3** shows the comparative charge transfer process occurs in the case of mono/bimetallic-TiO_2 nanocomposites.

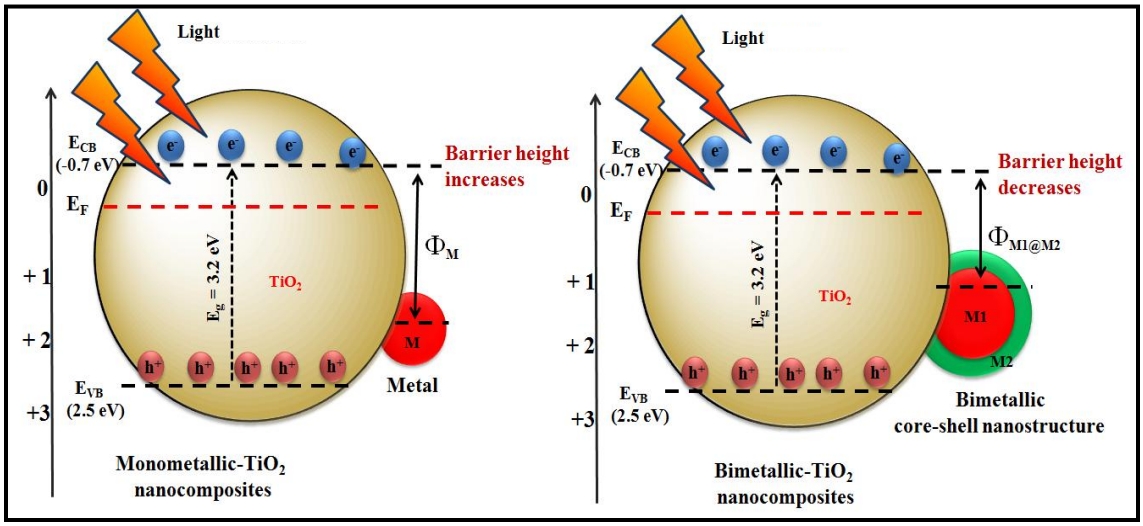

Scheme-1.3: Charge transfer process in the case of mono/bimetallic-TiO_2 nanocomposites.

1.1.5 Hydrogenation reaction

The hydrogenation of carbonyl group (C=O) is commercially important step for a large number of applications and mostly used in the formation of various drugs, paints, pesticides and polymers. Although both mono and bimetallic catalysts have been used for this purpose, bimetallic catalyst exhibits a particular interest because of its superior activity, stability, and selectivity [54-56]. The bimetallic nanostructure catalysts have gained particular interest in the field of hydrogenation. Luo *et al.* [57] investigated the PdAu and PtAu alloy nanostructures for the allyl alcohol hydrogenation and observed that PdAu nanostructure exhibited enhanced activity relative to PtAu alloy nanostructure. Kathyayini *et al.* [58] reported the catalytic selective hydrogenation of unsaturated aldehydes using Cu based bimetallic nanocatalyst supported on multiwall carbon nanotubes and found that Cu-Ni exhibited superior activity as compared to other nanocatalysts. Han *et al.* [59] reported that bimetallic Pd-Ru supported on gamma alumina exhibited superior activity for hydrogenation of 2-ethylanthraquinone than monometallic nanocatalysts. Shao *et al*. [60] studied the catalytic activity of Pd-Au bimetallic nanostructure supported on carbon nanotubes for the selective hydrogenation of phenyl acetylene and observed that bimetallic nanocatalyst exhibited superior selectivity relative to monometallic ones.

The photocatalytic hydrogenation of organic compounds using semiconductor photocatalysis attracted a lot of interest. Zhu *et al.* [61] reported the co-catalytic activity of Au and Cu incorporated on ZrO_2 for the selective hydrogenation of nitro aromatics under visible light radiation. Zhang *et al.* [62] reported that Pt/MesoTiO_2-SiO_2 nano composite was a highly effective catalyst for the selective hydrogenation of cinnamaldehyde. Zhou *et al.* [63] reported the photocatalytic hydrogenation of CO_2 to methane using Pd/Ce-TiO_2 nanocomposite under visible light radiation. Yamashita *et al.* [64] studied the chemo selective hydrogenation of nitro styrene using bimetallic Pd-Ag nanoparticles supported on mesoporous silica under visible light radiation. Yang *et al.* [65] reported the photocatalytic hydrogenation of cinnamaldehyde using the Au/SiC nanocatalyst under visible light radiation.

Section-B

1.2 Research Gaps

From literature survey, we came across the fact that different kinds of bimetallic nanostructure are available like alloy or intermetallic compounds which are different in their atomic ordering, subcluster with two interfaces, spheres with dendrites, dumbbell-shaped, and core-shell nanostructure having one or multiple shells. But the formation of spherical core-shell nanostructure by galvanic interactions between the two different metals (Ni, Pd, Cu, Zn, Au, and Ag) is rarely reported. Based on the literature review following points need to be explored for improving the catalytic and co-catalytic activity of bimetallic nanostructures.

(a) Core-shell and inverse core-shell nanostructures formed by galvanic interactions are very important compared to alloy nanostructure. By systematic tuning the core size or shell thickness, the catalytic efficiency of bimetallic nanocatalyst of galvanic metals can be improved.

(b) The nature of metal core and shell thickness, chemical composition, particle size and shape that affect the catalytic selective hydrogenation of unsaturated organic compounds in comparison to monometallic nanoparticles are not investigated for maximum efficiency.

(c) These core-shell (M1@M2) bimetallic nanostructures can be used as a good co-catalyst to improve the TiO_2 photocatalytic activity for the organic hydrogenation reaction under light radiation. The research work related to the photocatalytic hydrogenation by core-shell co-catalyst is not investigated widely.

In order to overcome the above mentioned facts following objectives were designed for the synthesis of bimetallic core-shell nanostructures to study the selective hydrogenation of unsaturated organic compounds. The research work also focused on studying the photocatalytic activity of bimetallic nanostructure under UV/Visible or solar radiation as compared to their monometallic counterparts.

1.3 Objectives

1. Preparation and characterization of core-shell bimetallic nanostructure (M1@M2) by galvanic interaction between the metals (Ni, Pd, Cu, Zn, Au, and Ag)
2. To study the catalytic hydrogenation of unsaturated organic compounds with synthesized bimetallic nanocatalysts as compared to their monometallic counterparts
3. To prepare and characterize M1@M2/TiO_2 nanocomposites for studying their co-catalytic activity for the selective hydrogenation reactions.

Section-C

1.4 Methodology

1.4.1 Synthesis of bimetallic core-shell nanostructure:

Based upon reduction potential value of metals, the bimetallic core-shell (M1@M2) nanostructures were synthesized by one pot co-reduction method. In a standard procedure, two metallic precursors were added at the same time followed by the addition of suitable reducing agent (Ascorbic acid, Hydrazine, $NaBH_4$ etc.). The metal ions having more positive reduction potential are reduced first and serve as a core and on other hand the metals with lower reduction potential make a shell over the reduced metal nanoparticles depending upon the galvanic interaction between the two metal ions in the presence of suitable stabilizing agent as shown in **Scheme-1.4**. The shell thickness coated on the metal core can be controlled by adding different amount of M_2 salt solution to the fixed amount of core solution.

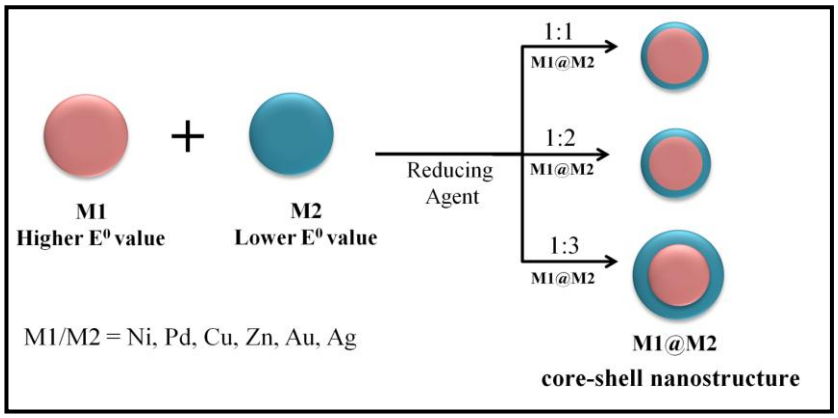

Scheme-1.4: Schematic representation of formation of bimetallic core-shell (M1@M2) nanostructure.

1.4.2 Preparation of bimetallic-semiconductor (TiO_2) nanocomposites

The synthesis of bimetallic as well as monometallic/TiO_2 nanocomposites was carried out by wet impregnation method. The as-prepared TiO_2 (200 mg) was dispersed in distilled water (20 ml) using ultrasonic treatment for 20 min. The required amount of bimetallic and monometallic metal nanoparticles (1 to 3 wt % with respect to TiO_2) was added to the mixture and stirred for 24 hours. The resulting nanocomposite was centrifuged, washed several times with water, ethanol and dried at 25 ^oC for further analysis. The schematic representation for the synthesis of mono/bimetallic-TiO_2 nanocomposites is given below (**Scheme-1.5**).

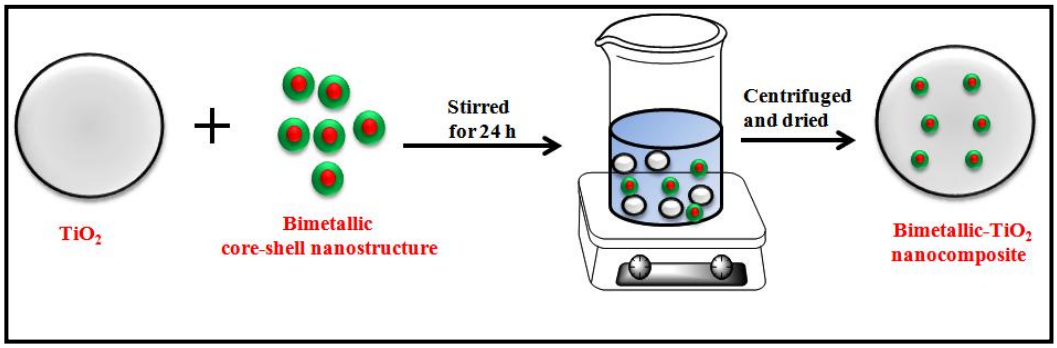

Scheme-1.5: Schematic procedure for the synthesis of bimetallic-TiO_2 nanocomposites.

1.5 Characterization techniques

Different modified and self planned synthetic procedures were used in the formation of desired bimetallic core@shell nanostructure and TiO_2 nanocomposites (experimental details are specified in the respective chapters). The as-prepared nanocatalysts were analyzed by using various optical, surface and structural determining characterization techniques. The detailed descriptions of different techniques are discussed below:

1.5.1 UV-Vis spectroscopy

The absorption properties of as-prepared liquid sample of nanocatalysts were analyzed by UV-2450, Shimadzu within the wavelength range of 190-1100 nm. The optical properties of powder solid sample of mono/bimetallic-TiO_2 nanocomposites were determined with diffuse reflectance spectroscopy (DRS, Avantes) using barium sulfate ($BaSO_4$) as an internal standard. Also, the band gap of bare titanium dioxide (TiO_2) and metal/bimetal doped titanium dioxide was determined by using Tauc plot equation.

1.5.2 Dynamic light scattering (DLS)

DLS analyzer was used to measure the average hydrodynamic size of mono/bimetallic nanostructures. The measurement of hydrodynamic size of mono/bimetallic nanostructures was carried out by dispersing 2 mg of the catalyst in 5 ml of deionized water using Malvern ZEN-3600.

1.5.3 X-ray powder diffraction (XRD)

XRD is an analytical technique used to measure the diffraction pattern, crystallinity of the material, lattice plane and facet design of as-prepared catalyst using Cu Kα (1.54A^{o}) radiation and angle range of 20^{0}–90^{0} at a rate of five degree rise per minute. PANalytical-Xpert-Pro diffractometer was used to record the XRD spectra of mono/bimetallic-TiO_2 nanocomposites.

1.5.4 Morphological analysis

The structural features like shape and particle size of as-prepared nanocatalysts were determined by using different electron microscopy like scanning electron microscopy (SEM), Field Emission Scanning Electron Microscopy (FESEM), Transmission electron microscopy (TEM) and scanning transmission electron microscopy (STEM). The elemental composition was determined by line profile or elemental color dot EDS (Energy dispersive X-ray spectrometer) mapping.

JEOL, JEM-F200 and Hitachi-7500 instruments were used to carry out TEM, HRTEM and STEM analysis operating at accelerating voltage of 200 kV. The magnifications for TEM analysis ×20 to ×2.0 M and for STEM analysis ×200 to ×150 M were used. Bruker windowless EDS detector was used to determine the elemental composition. SU8-180 (Tokyo Japan) was used to carry out FESEM analysis.

1.5.5 Surface and porosity analysis

The Brunauer-Emmett-Teller (BET, BEL mini-I) instrument was used to determine the surface area and porosity of the as-prepared mono/bimetallic-TiO_2 nanocomposites. First, the sample undergoes heat treatment process (150-200 ^{o}C) in order to remove the adsorbed gas and water molecules. The analysis was carried out at -195 ^{o}C using liquid nitrogen. The Barrett-Joyner-Halenda (BJH) analysis curves were used to determine the pore size and pore volume.

1.5.6 X-ray photoelectron spectroscopy (XPS)

The chemical state of different elements present in the mono/bimetallic-TiO_2 nanocomposites were determined by XPS analysis. The XPS data was recorded on VersaProbe-III (PHI-5000) using Al-Kα source (1486.6 eV) and also on Shimadzu-165, UK XPS instrument.

1.5.7 Photoluminescence spectroscopy (PL)

The PL spectra of different photocatalysts were recorded by exciting the material at 320 nm. The analysis was carried out by dispersing mono/bimetallic-TiO_2 nanocomposites in distilled water and data was recorded on Perkin-Elmer, LS5 instrument.

1.5.8 Thermogravimetric analysis (TGA)

The thermal properties and stability of synthesized mono/bimetallic-TiO_2 nanocomposites were determined by TGA. The mass loss of the material occurred with respect to the temperature was recorded on Shimadzu-TGA50 in the temperature range of 25-600 ^oC.

1.5.9 Gas-chromatography (GC)

The identification of the hydrogenated product was done by GC–MS (Bruker) and further analyzed with gas chromatography (Nucon) equipped with a flame ionization detector (FID) and capillary column (BR-1 ms). The oven temperature was varied from 120 ^oC to 260 ^oC with 10 ^oC rise/min and keeping the temperature of the detector and injector constant at 350 ^oC and 250 ^oC respectively.

Section-D

1.6 Catalytic activity

The catalytic activity of various core-shell bimetallic nanostructures relative to monometallic counterparts was carried out for the hydrogenation of unsaturated carbonyl compounds and other organic compounds under continuous flow of hydrogen. The reaction samples were analyzed by UV–Vis spectrophotometer. The different products formed were further quantified by high performance liquid chromatography (HPLC), gas chromatography (GC) equipped with FID detector, and GC-MS.

1.7 Co-catalytic activity

The co-catalytic activity of various TiO_2-$M_1@M_2$ composite samples was evaluated by the photocatalytic hydrogenation of unsaturated carbonyl and other organic compounds under visible, solar or UV-light illumination (**Scheme-1.6**). The final product was identified with GC-MS and further quantified with GC having a flame ionization detector (FID).

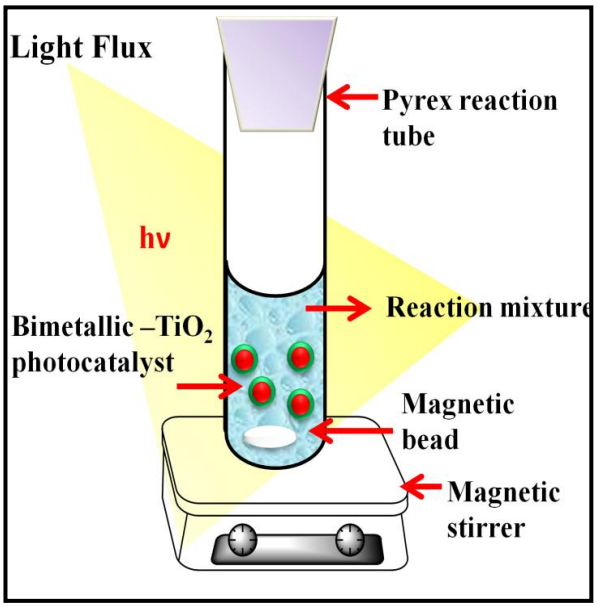

Scheme-1.6: Reaction setup for photocatalytic hydrogenation.

Model reactions which are carried out for catalytic and co-catalytic activity of core-shell nanostructures.

Reactant	Product	Uses
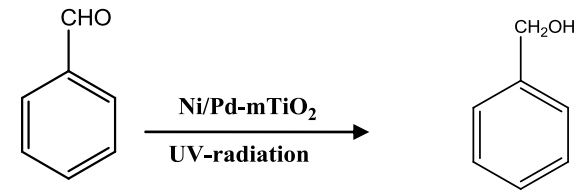		In the manufacture of soaps, skin lotions, topical creams
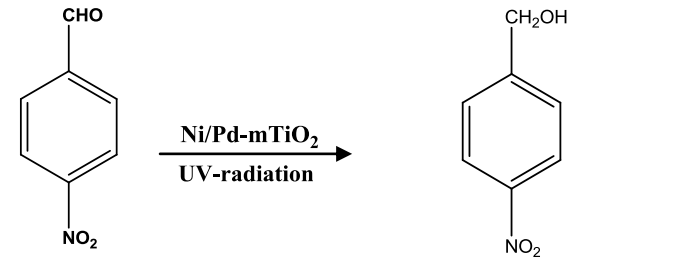		
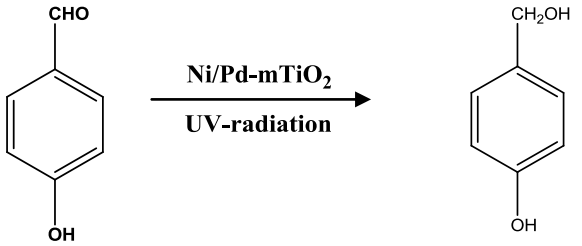		

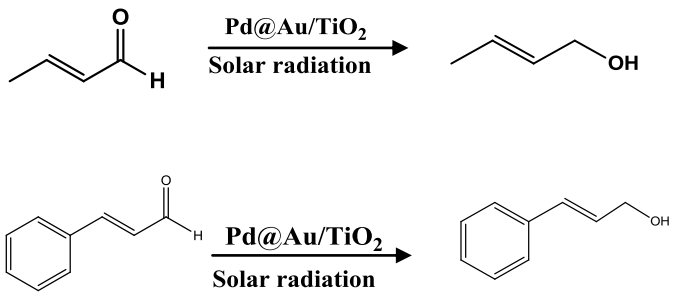	Used in cosmetic products as a fragnance ingredient and as flavoring agents
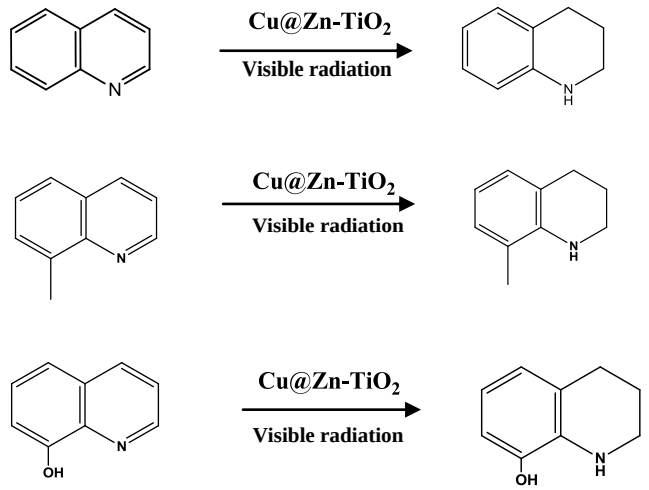	In the manufacture of dyes and preparation of hydroxyquinoline sulfate and niacin

References

[1] N. Kolobov, D. Svintsitskiy, E. Kozlova, D. Selishchev, D. Kozlov, Chem. Eng. J., 314 (2017) 600-611.

[2] M. Nasrollahzadeh, Z. Issaabadi, M.M. Tohidi, S. Mohammad Sajadi, Chem. Rec., 18 (2018) 165-229.

[3] Z. Lou, M. Fujitsuka, T. Majima, J. Phys. Chem. Lett., 8 (2017) 844-849.

[4] L. Liu, F. Gao, P. Concepción, A. Corma, J. Catal., 350 (2017) 218-225.

[5] K. Yuan, T. Song, D. Wang, X. Zhang, X. Gao, Y. Zou, H. Dong, Z. Tang, W. Hu, Angew. Chem. Int. Ed., (2018).

[6] P.V. Kamat, J. Phys. Chem. B, 106 (2002) 7729-7744.

[7] K.L. Kelly, E. Coronado, L.L. Zhao, G.C. Schatz, J. Phys. Chem. B 107 (2003) 668-677.

[8] P. Suchomel, L. Kvitek, R. Prucek, A. Panacek, A. Halder, S. Vajda, R. Zboril, Sci. Rep., 8 (2018) 1-11.

[9] J. Mondal, Q.T. Trinh, A. Jana, W.K.H. Ng, P. Borah, H. Hirao, Y. Zhao, ACS Appl. Mater. Interfaces, 8 (2016) 15307-15319.

[10] A. Bathla, B. Pal, ChemistrySelect, 3 (2018) 4738-4744.

[11] Y.-H. Won, K. Huh, L.A. Stanciu, Biosens. Bioelectron., 26 (2011) 4514-4519.

[12] J. Helmlinger, C. Sengstock, C. Groß-Heitfeld, C. Mayer, T. Schildhauer, M. Köller, M. Epple, RSC Adv., 6 (2016) 18490-18501.

[13] R. Xu, D. Wang, J. Zhang, Y. Li, Chem. Asian J., 1 (2006) 888-893.

[14] D. Gogoi, A. Namdeo, A.K. Golder, N.R. Peela, Int. J. Hydrogen Energ., 45 (2020) 2729-2744.

[15] R. Wang, J. Shen, K. Sun, H. Tang, Q. Liu, Appl. Surf. Sci., 493 (2019) 1142-1149.

[16] P. Deng, M. Gan, X. Zhang, Z. Li, Y. Hou, Int. J. Hydrogen Energ., 44 (2019) 30084-30092.

[17] F.-M. McKenna, J.A. Anderson, J. Catal., 281 (2011) 231-240.

[18] H.T. Nasrabadi, E. Abbasi, S. Davaran, M. Kouhi, A. Akbarzadeh, Artif. Cells, Nanomed. Biotechnol., 44 (2016) 376-380.

[19] A. Zaleska-Medynska, M. Marchelek, M. Diak, E. Grabowska, Adv. Colloid Interface Sci., 229 (2016) 80-107.

[20] C. Tyson, A. Bzowski, P. Kristof, M. Kuhn, R. Sammynaiken, T. Sham, Phys. Rev. B, 45 (1992) 8924.

[21] S. Nishimura, A.T.N. Dao, D. Mott, K. Ebitani, S. Maenosono, J. Phys. Chem. C, 116 (2012) 4511-4516.

[22] S. Sakong, C. Mosch, A. Groß, Phys. Chem. Chem. Phys., 9 (2007) 2216-2225.

[23] A. Monga, B. Pal, Colloids Surf. A, 481 (2015) 158-166.

[24] Y. Hong, X. Jing, J. Huang, D. Sun, T. Odoom-Wubah, F. Yang, M. Du, Q. Li, ACS Sustain. Chem. Eng., 2 (2014) 1752-1759.

[25] T.D. Thanh, N.D. Chuong, H.V. Hien, N.H. Kim, J.-H. Lee, ACS Appl. Mater. Interfaces, (2018).

[26] K.K. Haldar, S. Kundu, A. Patra, ACS Appl. Mater. Interfaces, 6 (2014) 21946-21953.

[27] A. Vysakh, C.L. Babu, C. Vinod, J. Phys. Chem. C, 119 (2015) 8138-8146.

[28] A. Monga, R.A. Rather, B. Pal, Sol. Energy Mater. Sol. Cells, 172 (2017) 285-292.

[29] H. Wang, C. Wang, H. Yan, H. Yi, J. Lu, J. Catal., 324 (2015) 59-68.

[30] S. Ma, M. Sadakiyo, M. Heima, R. Luo, R.T. Haasch, J.I. Gold, M. Yamauchi, P.J. Kenis, J. Am. Chem. Soc., 139 (2016) 47-50.

[31] F. Liao, X.-P. Wu, J. Zheng, M.M.-J. Li, A. Kroner, Z. Zeng, X. Hong, Y. Yuan, X.-Q. Gong, S.C.E. Tsang, Green Chem., 19 (2017) 270-280.

[32] K. Mallik, M. Mandal, N. Pradhan, T. Pal, Nano Lett., 1 (2001) 319-322.

[33] Y. Sun, Y. Xia, J. Am. Chem. Soc., 126 (2004) 3892-3901.

[34] M. Tsuji, N. Miyamae, S. Lim, K. Kimura, X. Zhang, S. Hikino, M. Nishio, Cryst. Growth Design, 6 (2006) 1801-1807.

[35] M. Tsuji, N. Nakamura, M. Ogino, K. Ikedo, M. Matsunaga, CrystEngComm, 14 (2012) 7639-7647.

[36] Y. Xiang, X. Wu, D. Liu, Z. Li, W. Chu, L. Feng, K. Zhang, W. Zhou, S. Xie, Langmuir, 24 (2008) 3465-3470.

[37] S. De, J. Zhang, R. Luque, N. Yan, Energy Environ. Sci., 9 (2016) 3314-3347.

[38] K.D. Gilroy, A. Ruditskiy, H.-C. Peng, D. Qin, Y. Xia, Chem. Rev., 116 (2016) 10414-10472.

[39] H.-L. Jiang, T. Akita, T. Ishida, M. Haruta, Q. Xu, J. Am. Chem. Soc., 133 (2011) 1304-1306.

[40] G. Fu, Z. Liu, Y. Chen, J. Lin, Y. Tang, T. Lu, Nano Res., 7 (2014) 1205-1214.
[41] M. Wu, X. Wu, L. Zhang, A. Abdelhafiz, I. Chang, C. Qu, Y. Jiang, J. Zeng, F. Alamgir, Electrochim. Acta, 306 (2019) 167-174.
[42] Y. Yang, J. Liu, Z.-W. Fu, D. Qin, J. Am. Chem. Soc., 136 (2014) 8153-8156.
[43] L. Fu, W. Cai, A. Wang, Y. Zheng, Mater. Lett, 142. (2015) 201-203.
[44] P. Sharma, Y. Sasson, Green Chem., 19 (2017) 844-852.
[45] A. Aguilar-Tapia, L. Delannoy, C. Louis, C.W. Han, V. Ortalan, R. Zanella, J. Catal., 344 (2016) 515-523.
[46] S. Rohani, A. Ziarati, G.M. Ziarani, A. Badiei, T. Bürgi, Catal. Sci. Technol., (2019).
[47] M. Pradenas, J. Yáñez, S. Ranganathan, D. Contreras, P. Santander, H.D. Mansilla, Water Environ. Res., 91 (2019) 157-164.
[48] M. Edelmannová, K.-Y. Lin, J.C. Wu, I. Troppová, L. Čapek, K. Kočí, Appl. Surf. Sci., 454 (2018) 313-318.
[49] B. Boro, B. Gogoi, B. Rajbongshi, A. Ramchiary, Renewable and Sustainable Energy Reviews, 81 (2018) 2264-2270.
[50] D. Tsukamoto, A. Shiro, Y. Shiraishi, Y. Sugano, S. Ichikawa, S. Tanaka, T. Hirai, ACS Catal., 2 (2012) 599-603.
[51] A. Monga, A. Bathla, B. Pal, Sol. Energy, 155 (2017) 1403-1410.
[52] A. Crake, K.C. Christoforidis, R. Godin, B. Moss, A. Kafizas, S. Zafeiratos, J.R. Durrant, C. Petit, Appl. Catal., B, 242 (2019) 369-378.
[53] R.A. Rather, D. Pooja, P. Kumar, S. Singh, B. Pal, J. Clean. Prod., 175 (2018) 394-401.
[54] Z. Mou, M. Han, G. Li, Y. Du, P. Yang, H. Zhang, Z. Deng, Mater. Res. Bull., 48 (2013) 4780-4784.
[55] K. Everaere, A. Mortreux, J.F. Carpentier, Adv. Syn. Catal., 345 (2003) 67-77.
[56] R.M. Mironenko, O.B. Belskaya, T.I. Gulyaeva, M.V. Trenikhin, A.I. Nizovskii, A.V. Kalinkin, V.I. Bukhtiyarov, A.V. Lavrenov, V.A. Likholobov, Catal. Today, 279 (2017) 2-9.
[57] L. Luo, Z. Duan, H. Li, J. Kim, G. Henkelman, R.M. Crooks, J. Am. Chem. Soc., 139 (2017) 5538-5546.
[58] H. Hareesh, K. Minchitha, K. Venkatesh, N. Nagaraju, N. Kathyayini, RSC Adv., 6 (2016) 82359-82369.
[59] J. Zhang, K. Gao, S. Wang, W. Li, Y. Han, RSC Adv., 7 (2017) 6447-6456.

[60] S. Wang, Z. Xin, X. Huang, W. Yu, S. Niu, L. Shao, Phys. Chem. Chem. Phys., 19 (2017) 6164-6168.
[61] Q. Xiao, S. Sarina, E.R. Waclawik, J. Jia, J. Chang, J.D. Riches, H. Wu, Z. Zheng, H. Zhu, ACS Catal., 6 (2016) 1744-1753.
[62] Q. Wu, C. Zhang, B. Zhang, X. Li, Z. Ying, T. Liu, W. Lin, Y. Yu, H. Cheng, F. Zhao, J. Colloid Interface Sci., 463 (2016) 75-82.
[63] N. Li, X. Zou, M. Liu, L. Wei, Q. Shen, R. Bibi, C. Xu, Q. Ma, J. Zhou, J. Phys. Chem. C, 121 (2017) 25795-25804.
[64] P. Verma, M. Navlani-García, Y. Kuwahara, K. Mori, H. Yamashita, J. Chem. Sci., 129 (2017) 1661-1669.
[65] C.-H. Hao, X.-N. Guo, Y.-T. Pan, S. Chen, Z.-F. Jiao, H. Yang, X.-Y. Guo, J. Am. Chem. Soc., 138 (2016) 9361-9364.

CHAPTER- 2

UV-light responsive selective hydrogenation of carbonyl compounds using bimetallic Pd@Ni-mesoporous TiO_2 nanocatalyst

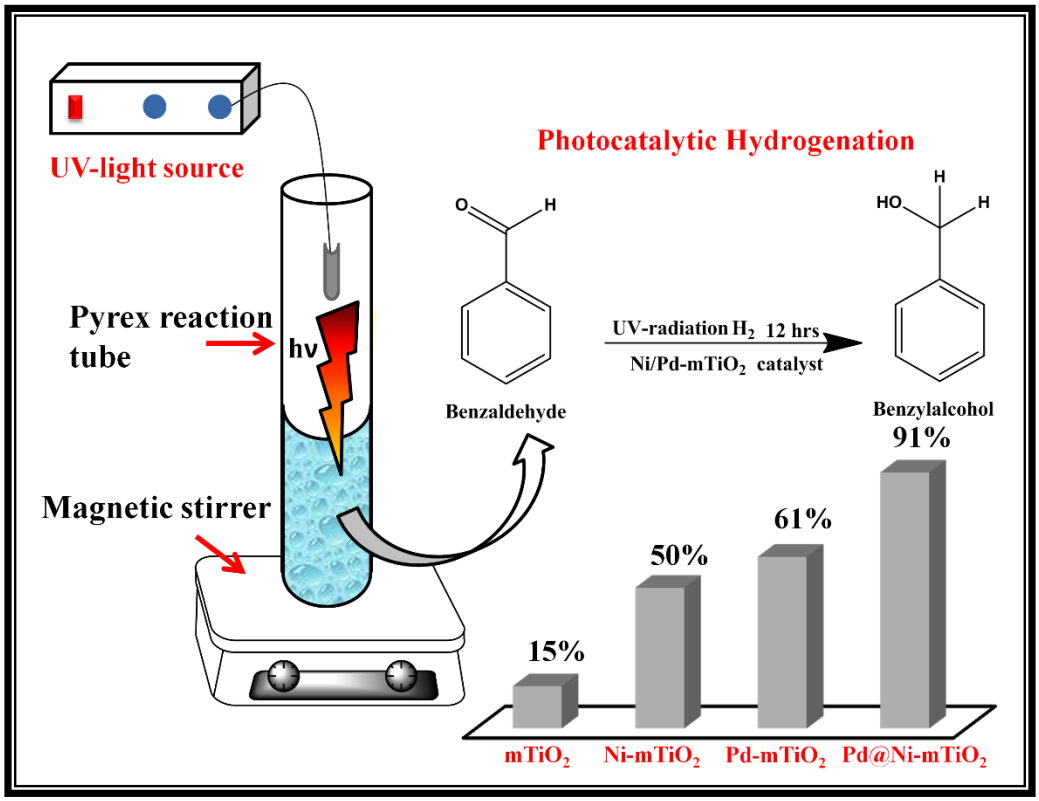

Schematic outline

This study reveals the co-catalysis of bimetallic Pd@Ni nanostructure impregnated on mesoporous TiO_2 compared to their monometallic analogues for the photo-catalytic and selective hydrogenation of unsaturated aldehydes under UV-light irradiation. The higher activity of bimetallic nanocomposites arises due to hindrance in the recombination rate of charge carriers resulting in effective charge transfer at bimetallic-mTiO_2 interface relative to monometallic-mTiO_2 nanocomposites.

2.1 Introduction

Metal nanoparticles are extensively used in hydrogenation, oxidation-reduction reactions, and carbon-carbon cross coupling [1–9] because of their small size and extremely large surface area. Besides the large number of catalytic applications, the single metal nanocatalysts are still not able to accomplish the activity and selectivity requirements for the reactions. These specific properties of metal nanoparticles are improved by depositing another metal on the surface of first metal. In recent years, bimetallic nanocomposites have gained considerable attention in the area of catalysis [10–13]. Bimetallic nanocatalysts exhibited distinctive electronic and chemical properties compared to their parent metals. The enhancement in their catalytic performance is credited to the synergistic or electronic interaction between the metals, resulting in higher selectivity and increased yield for the reaction [14–17]. Monga et al. [18] explored that different shape bimetallic Au@Ag nanostructure displayed better photo-activity for the nitro aromatic reduction than monometallic ones. Similarly, Chen et al. [19] reported the bimetallic Au-Pd supported on SBA-15 displayed superior catalytic activity for the benzyl alcohol oxidation than monometallic (Au and Pd) nanocomposites. The hydrogenation of carbonyl group (C=O) is the commercially important step for a large number of applications and mostly used in the formation of various drugs, paints, pesticides and polymers [20– 23]. Presently, many efforts have been made in the preparation of an effective catalyst for the selective hydrogenation of carbonyl compounds to their corresponding alcohol. Although both mono and bimetallic catalyst have been used for this purpose, bimetallic catalyst exhibits a particular interest because of their superior activity, stability, and selectivity [24–26]. Among the bimetallic nanostructure palladium-based catalysts have gained particular interest in the field of hydrogenation. Luo et al. [27] reported that PdAu and PtAu alloy nanostructure for the allyl alcohol hydrogenation and observed that PdAu nanostructure exhibited enhanced activity relative to PtAu alloy nanostructure. Similarly, Zhang et al. [28] reported that bimetallic Pd-Ru supported on gamma alumina exhibited superior activity for hydrogenation of 2-ethylanthraquinone than monometallic nanocatalysts. Furthermore, heterogeneous semiconductor photocatalyst has been widely employed in various organic transformations like hydrogenation of alkenes, alkynes, ketones and aldehydes [29–32]. Out of various semiconductors, TiO_2 is considered promising material for various photocatalytic activities despite the fact that titanium dioxide (P25) has certain limitations: low surface area, fast electron-hole pair recombination. Recently,

mesoporous TiO_2 has emerged as an effective material to overcome these obstructions. Large surface area, high porosity and brilliant electronic properties of mesoporous TiO_2 resulted in efficient charge transfer and improved the quantum yield for various photocatalytic reactions [33–35]. Wu et al. [7] reported the Pt/MesoTiO_2-SiO_2 nanocomposite was highly effective catalyst for the selective hydrogenation of cinnamaldehyde. Similarly, Sree-thawong and Yoshikawa [36] studied the effect of impregnation of copper, palladium, and gold on mesoporous titanium dioxide for photocatalytic hydrogen evolution under UV-light radiation. There are few reports showing the co-catalytic effect of bimetallic nanostructure deposited on mesoporous TiO_2 for the selective photocatalytic hydrogenation of carbonyl compounds. In the present study, we have synthesized mono (Ni and Pd), bimetallic core@shell nanostructure (Pd@Ni) and their impregnation on mesoporous titanium dioxide to examine the photo- catalytic hydrogenation of carbonyl compounds in comparison to monometallic-TiO_2 nanocomposites. Since, basic catalytic hydrogen transfer reaction of C=O group generally occurs in the harsh condition like high temperature, long reaction time. Therefore, keeping in mind the major key issues, we considered Pd@Ni nanostructure loading over mesoporous TiO_2 (with porosity) as a promising support to enhance the photoactivity and an ideal catalyst for both environmental and economical perspective.

2.2 Experimental

2.2.1 Chemicals and reagents

$PdCl_2$ (palladium chloride), potassium bromide (KBr), $NiCl_2.6H_2O$ (Nickel chloride hexahydrate), titanium butoxide ($C_{16}H_{36}O_4Ti$), isopropyl alcohol (C_3H_8O), ethylene glycol ($C_2H_6O_2$) polyvinylpyrrolidone (PVP, $(C_6H_9NO)n$), glacial acetic acid were purchased from Loba Chemie India and sodium borohydride ($NaBH_4$), benzaldehyde, 4-nitrobenzaldehyde (4-NBZ), 4-hydroxybenzaldehyde (4-HBZ) from Spectrochem Ltd. and were used as-received.

2.2.2 Synthesis of mesoporous titanium oxide ($mTiO_2$)

Mesoporous titanium oxide ($mTiO_2$) was prepared using template method. In synthesized procedure, 1.5 ml of $Ti(OBu)_4$ was added in beaker (100 ml) containing ethylene glycol (40 ml) followed by stirring for 8 h at 25 ^oC. The mixture was transferred into the solution containing acetone (200 ml), H_2O (5 ml), 1 ml glacial acetic acid and stirred for 3 h at 35 ^oC leading to the formation of titanium glycolate. The solution was further refluxed at 90–100 ^oC for 8 h to

synthesized mesoporous TiO_2. The final suspension was separated via centrifugation, washed with distilled water, ethanol and dried at 100 ^oC.

2.2.3 Preparation of monometallic (Pd and Ni) nanoparticles

In a typical synthesis, $PdCl_2$ (20 ml, 10^{-2} M) or $NiCl_2.6H_2O$ (85 mg) was added to the preheated solution of KBr (600 mg) and PVP (105 mg) in 10 ml of water. The solution was maintained at 80 ^oC for 30 min followed by the addition of freshly prepared 600 ml of 0.1 M $NaBH_4$ solution under magnetic stirring. The color transformed from yellow to black (in case of Pd) or green to black (in case of Ni) showing the formation of metal nanoparticles. The final product was separated and washed several times with water, ethanol and re-dispersed in water for further analysis.

2.2.4 Synthesis of bimetallic Pd@Ni nanostructure

In a standard procedure, 600 mg of KBr, 105 mg of PVP (MW = 30,000) and 10 ml of H_2O was added in round bottom flask (50 ml) and pre-heated in the oil bath for 10 min under magnetic stirring. Introduced the $PdCl_2$ (20 ml, 10^{-2}M) and $NiCl_2.6H_20$ (0.35 mmol) into the pre-heated solution and maintained the solution at 80 ^oC for 30 min. Added 600 ml of $NaBH_4$ (0.1 M) into mixture under stirring, an immediate color change to black indicated the formation of bimetallic nanoparticles and the solution was kept at 80 ^oC for additional 2 h. The main role of KBr is to facilitate the galvanic interaction between Pd and Ni which led to the formation of Pd@Ni nanostructure. The resulting product was centrifuged (8000 RPM, 5 min), washed and re-dispersed into the water.

2.2.5 Synthesis of mono/bimetallic-mTiO_2 nanocomposites

The synthesis of bimetallic Pd@Ni-mTiO_2, as well as monometallic (Ni-mTiO_2 and Pd-mTiO_2) nanocomposite, was done by wet impregnation method. The as-prepared mTiO_2 (200 mg) was dispersed in distilled water (20 ml) using ultrasonic treatment for 20 min. The required amount of bimetallic and monometallic metal nanoparticles (1 wt% with respect to TiO_2) was added to the mixture and stirred for 24 h. The overall synthesis procedure adopted for the formation of bimetallic-TiO_2 nanocomposites is represented in **Scheme-2.1**

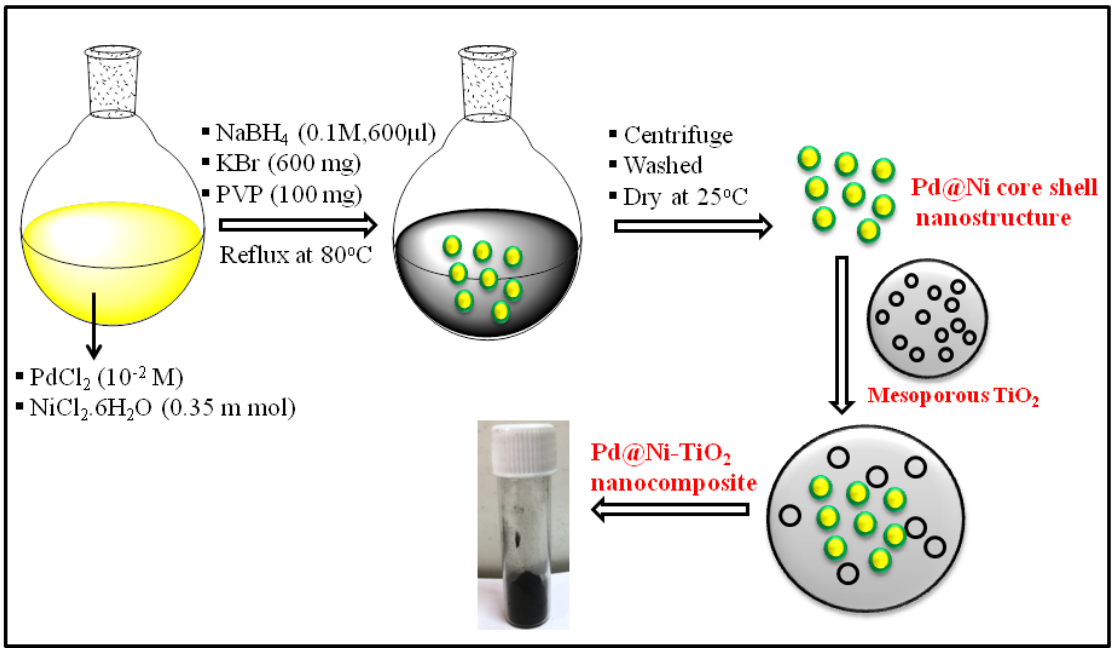

Scheme-2.1: Schematic representation of synthesized bimetallic Pd@Ni/mTiO_2 nanocomposite.

2.2.6 Characterization

The optical analysis of mono/bimetallic-mTiO_2 nanocomposite was examined with the UV-Visible spectrophotometer (Specord-205, Analytic-Jena), Photoluminescence spectra were measured using Perkin-Elmer LS5. Morphological and composition studies were determined by HR-TEM (FEI Technai, G2-F20) and EDS analysis. The hydrodynamic size of different photocatalyst was determined by Malvern ZEN3600 particle size analyzer. The XRD analysis was done by PANalytical-Xpert Pro with a diffraction angle of 20–90^o at 5^o rise/min. The oxidation state of photocatalyst was determined by XPS (X-ray photon spectroscopy, Shimadzu-165, UK). Furthermore, surface area and porosity were studied by BET surface analysis (BEL mini-II, Japan).

The photocatalytic activity was performed in a reactor containing 0.1 mM benzaldehyde in isopropyl alcohol (20 ml) (act as a hole scavenger) and 10 mg of photocatalyst under magnetic stirring and illuminated with UV lamp (Hg-arc, 125 W). Based on earlier findings, it was observed that different catalytic and photocatalytic reactions displayed superior efficiency and selectivity in presence of saturated hydrogen atmosphere and under light radiation. In order to maintain H_2 saturated atmosphere inside the reaction vessel, a hydrogen balloon was fixed at the top of vessel. The water was allowed to flow continuously through the reactor to maintain constant temperature of the lamp. The final product was first identified with GC–MS (Bruker,

SHS-40) and then quantified with GC (gas chromatography, Nucon Ltd., India) having a flame ionization detector (FID) and BR-1 ms capillary column (0.50 mm, 30 m × 0.32 mm). The injection was done manually with airtight syringe (Agilent, 10 ml), injector and detector was maintained at 250 ^{o}C and 330 ^{o}C respectively, and oven temperature was programmed as holding at 120 ^{o}C for 2 min and increasing to 260 ^{o}C with a 10 ^{o}C rise per minute. The percentage yield of the reaction was calculated by comparing peak area with the standard solutions. The fractional conversion of benzaldehyde was calculated as

$$X = \frac{(\text{benzaldehye})\text{in} - (\text{benzaldehyde})\text{out}}{(\text{benzaldehyde})\text{in}}$$

Where 'in' and 'out' are the subscripts refer to the amount of benzaldehyde taken initially and come out after the reaction. Similarly, selectivity with respect to benzyl alcohol is calculated as

$$S = \frac{[\text{product 1}]}{\{[\text{product 1}] + [\text{product 2}]\}} \text{X100}$$

2.3 Results and discussion

The optical analysis (**Fig. 2.1**) of as-prepared photocatalysts revealed that the mesoporous mTiO_2 showed the absorption edge at 343 nm. The deposition of Pd and Ni-NPs on mTiO_2 resulted in the formation of new absorption edges corresponding to wavelength 308 nm and 246 nm respectively. Moreover, with increasing concentration of Pd (constant Ni weight ratio) in PNT-1, PNT-2 and PNT-3 a considerable shift in the absorption intensity was observed relative to Pd-mTiO_2. The band gap of synthesized photocatalysts was determined by Tauc plot (**Fig. 2.2**). The band gap of mTiO_2 was calculated to be 3.2 eV, and no significant changes were observed after deposition of mono and bimetallic Pd@Ni nano-structures [37–39].

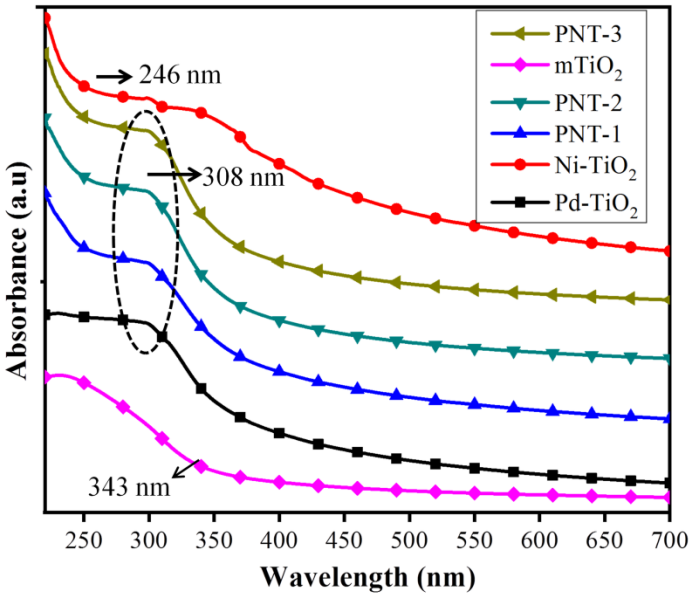

Fig. 2.1: Absorption spectra of different photocatalysts PNT-1, PNT-2, and PNT-3.

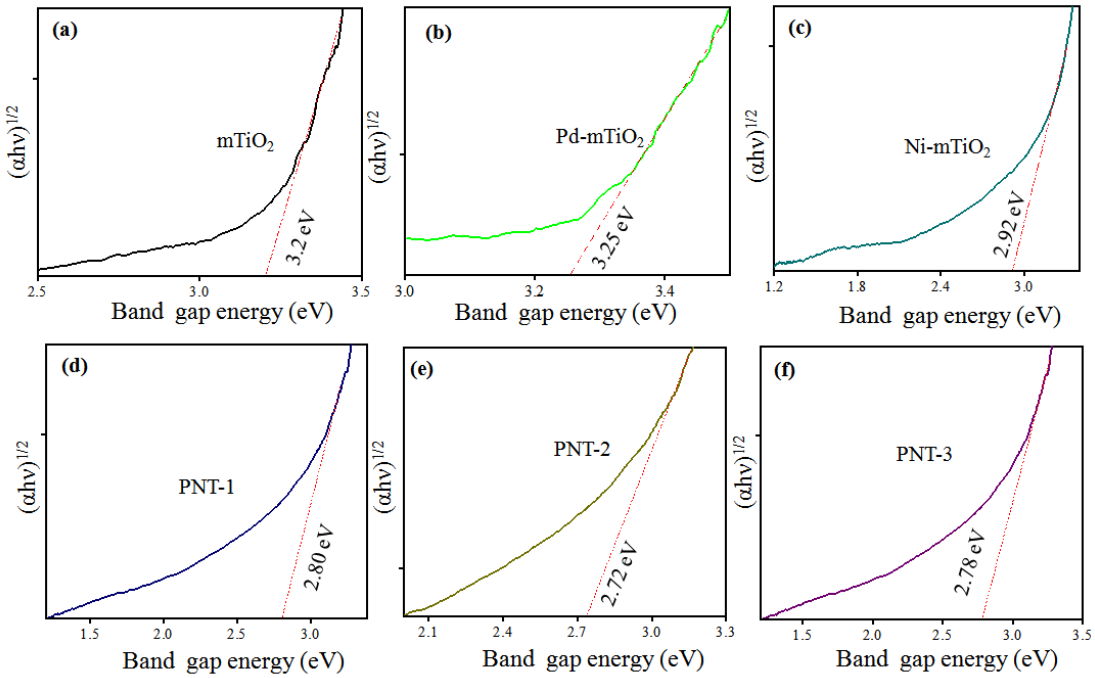

Fig. 2.2: The plot of $(\alpha h\nu)^{1/2}$ function versus the band gap energy of different monometallic and bimetallic modified $mTiO_2$.

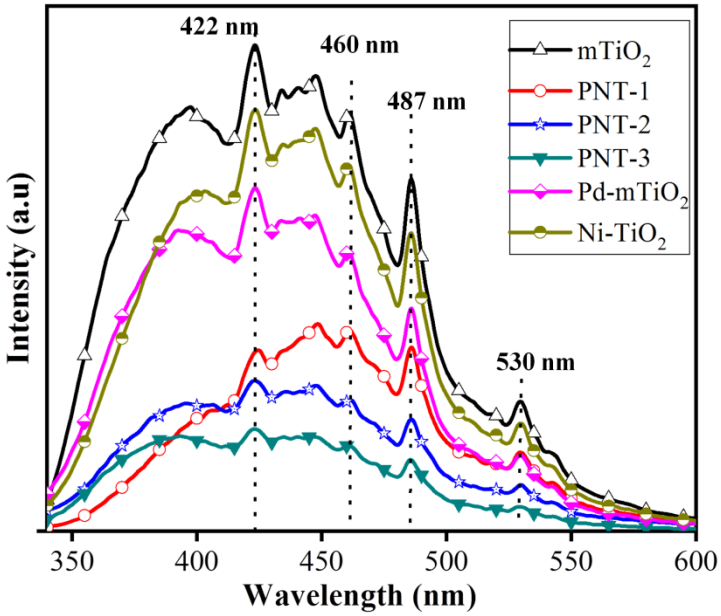

Fig. 2.3: Photoluminescence spectra of mono/bimetallic-$mTiO_2$ nanocomposites.

The photoluminescence spectra of $mTiO_2$ (**Fig. 2.3**) consist of several emission peaks corresponding to excitation at 320 nm. The major peaks at 397, 422, 460, 487 and 530 nm are assigned to surface state emission mainly arise due to oxygen vacancy, surface defects state in $mTiO_2$ nanoparticles and charge transfer from O^{2-} to Ti^{4+} [40, 41]. The metal deposited on the surface of $mTiO_2$ prevented the electron-hole ($e^-.h^+$) recombination and led to quenching of photoluminescence intensity. It was observed that bimetallic $Pd_1@Ni_1$-$mTiO_2$ (PNT-1) nanocomposite exhibited higher quenching of PL intensity relative to their monometallic-$mTiO_2$ nanocomposite. Moreover, with an increase in Pd concentration in PNT-2 ($Pd_2@Ni_1$-$mTiO_2$) and PNT-3 ($Pd_3@Ni_1$-$mTiO_2$), the PL intensity further reduced. This quenching occurred due to efficient transfer of photo-generated electrons and holes (charge carriers) from $mTiO_2$ to the bimetallic nanostructure. The hydrodynamic size (**Fig. 2.4 (a,b)**) was obtained by dispersing 2 mg of photocatalyst in distilled water (5 ml). It was observed that deposition of metal on the surface of mesoporous TiO_2 modified the particle size distribution of resulting nanocomposite. The average size of bare $mTiO_2$ was found to be 102 nm whereas after the deposition of Pd and Ni on the surface of $mTiO_2$ the size changes to 135 and 157 nm respectively. Furthermore, the average hydrodynamic size of bimetallic $mTiO_2$ nanocomposite (PNT-1) was observed to be 116 nm and with increasing concentration (wt%) of Pd and keeping the concentration of Ni constant in PNT-2 and PNT-3, the average hydrodynamic size of nanocomposites increased to 125 and 140 nm respectively.

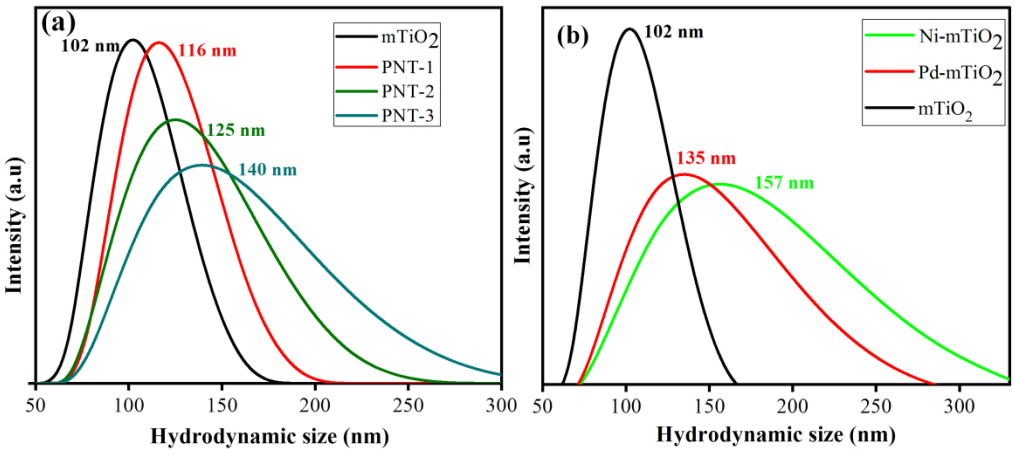

Fig. 2.4: (a) The hydrodynamic size of bimetallic-TiO_2 (b) monometallic-TiO_2 nanocomposites relative to $mTiO_2$.

The XRD diffraction pattern of $mTiO_2$ (**Fig. 2.5**) matches with anatase phase (JCPDS card 01-075-1537) showing its characteristic peak at 25.6° corresponding to plane (101) and some low-intensity peaks (symbolized with star, **Fig. 2.5**) at 54.5°, 62.7° and 75.1° are corresponding to lattice plane (105), (204) and (107) respectively. The diffraction pattern of Pd displayed several peaks (JCPDS card 01-087-0638, symbolized with a hollow circle) but strong diffraction peak at 40.20° corresponding to the plane (111) and others at 46.8°, 68.2°, and 82.3° which are indexed to (200), (220) and (311) respectively. The effect of an increase in Pd concentration was also observed showing the small changes in the sharpness and growth of planes in PNT-2 and PNT-3. Similarly, The X-ray analysis of Ni showed two diffraction peaks (JCPDS card 01-089-7129, symbolized with a dark circle) at 39.6° (100) and at 86.7° (201).

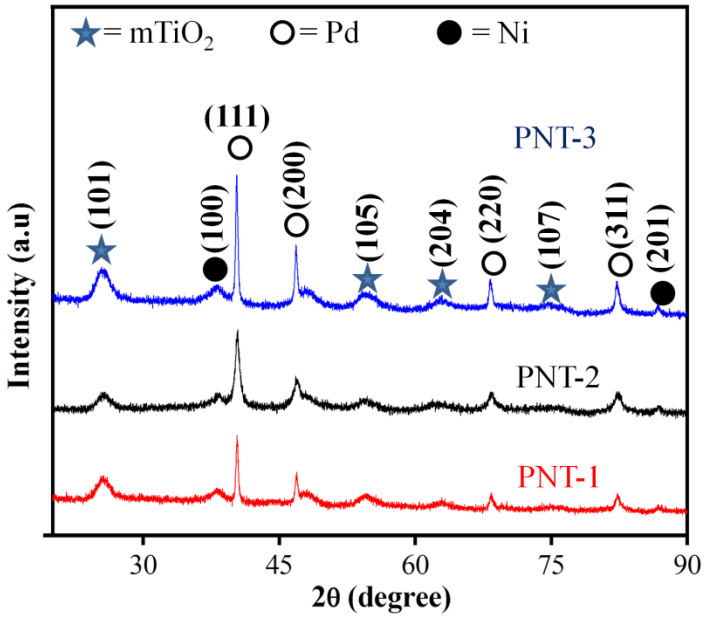

Fig. 2.5: XRD pattern of bimetallic Pd@Ni/$mTiO_2$ nanocomposites with varying Pd concentration.

HRTEM images (**Fig. 2.6**) represents the formation of core@shell (Pd@Ni) nanostructure analyzed by the presence of distinct lattice planes of Pd and Ni with interplanar distance of ~0.19 nm and ~0.20 nm corresponding to (200) and (100) plane respectively (**Fig. 2.6 (e)**), which was further supported by the SAED pattern (**Fig. 2.6 (f)**). In one pot co-reduction procedure, the reduction potential of metals played a crucial role in determining the final structural design of bimetallic nanocatalyst. In our case Pd having higher reduction potential (0.915 V) reduced first and act as a core whereas Ni having lower reduction potential act as a shell [42].

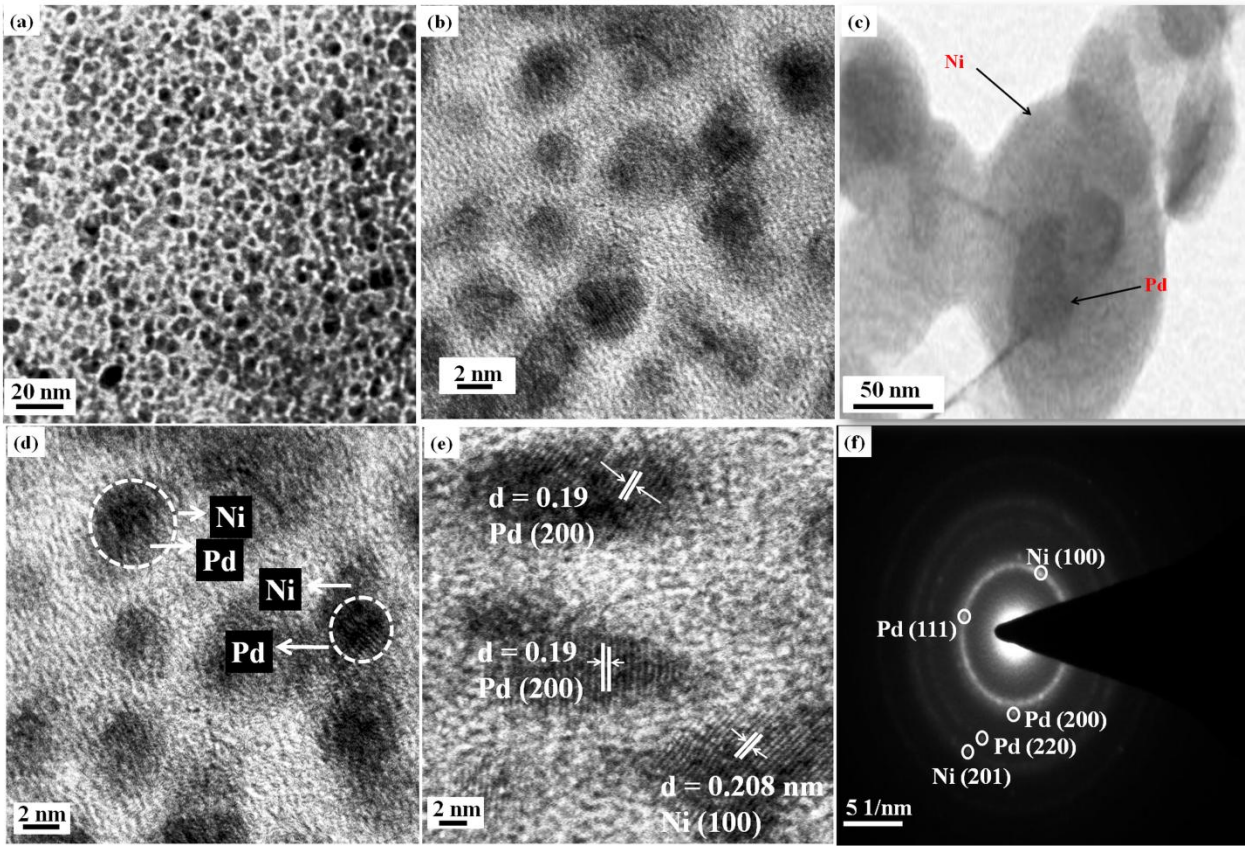

Fig. 2.6: (a-d) TEM images of Pd@Ni core-shell nanostructure (e) Lattice fringe and (f) SAED pattern for Pd@Ni nanostructure.

Furthermore, **Fig. 2.7 (a-d)** showing the TEM image of Pd@Ni doped mesoporous titanium oxide ($mTiO_2$) and HRTEM consisting of three distinctive lattice planes of TiO_2, Pd and Ni with an interplanar distance of ~0.33 (101), 0.22 (111) and 0.18 nm (201) respectively. The atomic ratio of these elements in $mTiO_2$ was examined by EDS Spectra (**Fig. 2.8**). The dot color mapping of PNT-3 (**Fig. 2 9**) represents the uniform distribution of Pd, Ti, O, and Ni elements.

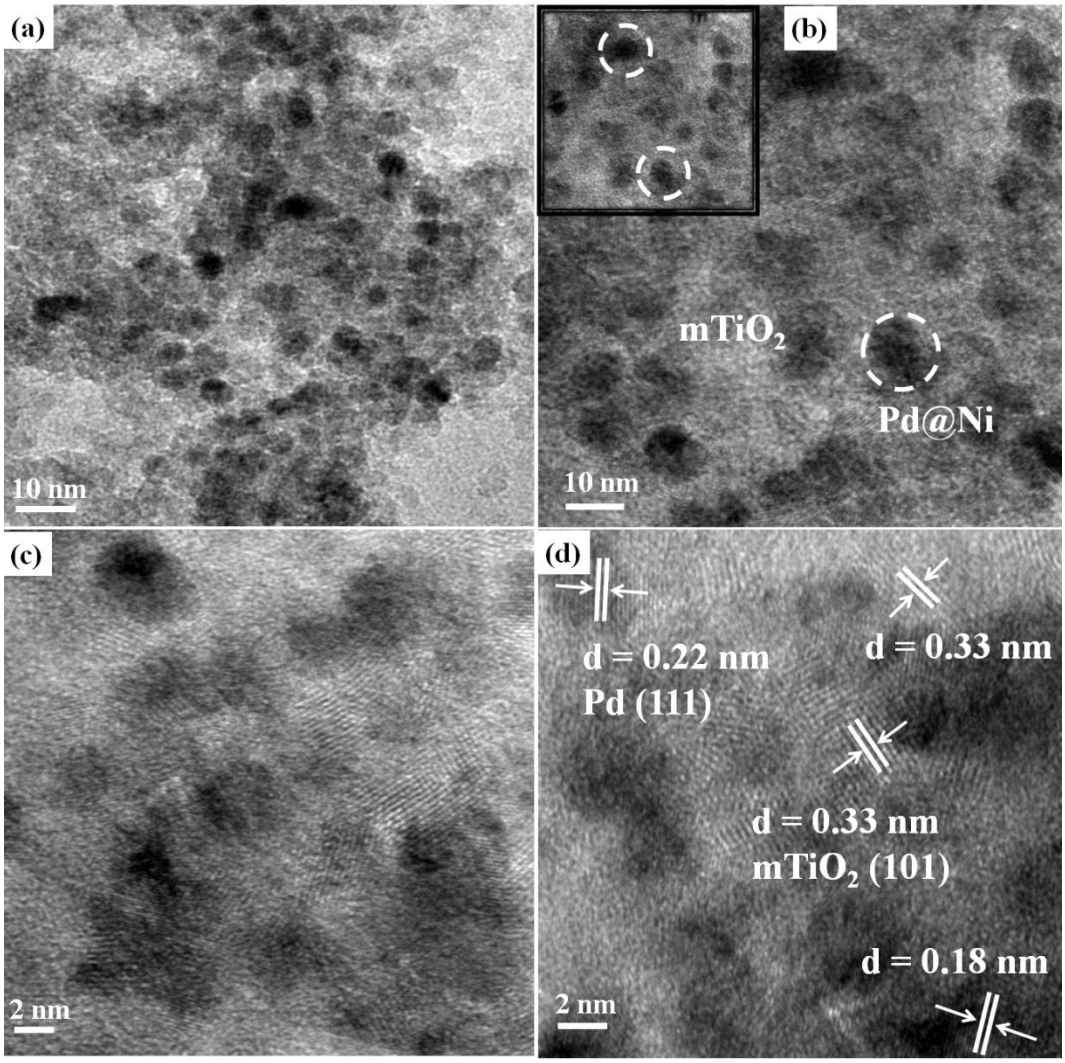

Fig. 2.7: (a-d) HRTEM images of $Pd_3@Ni_1$-$mTiO_2$ (PNT-3) nanocomposites.

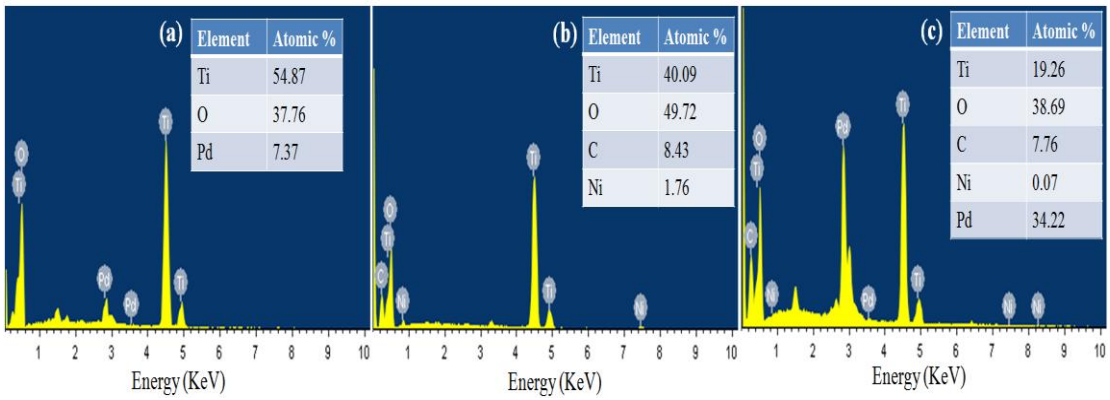

Fig. 2.8: EDS analysis of (a) Pd-$mTiO_2$ (b) Ni-$mTiO_2$ (c) Pd@Ni-$mTiO_2$ (PNT-3).

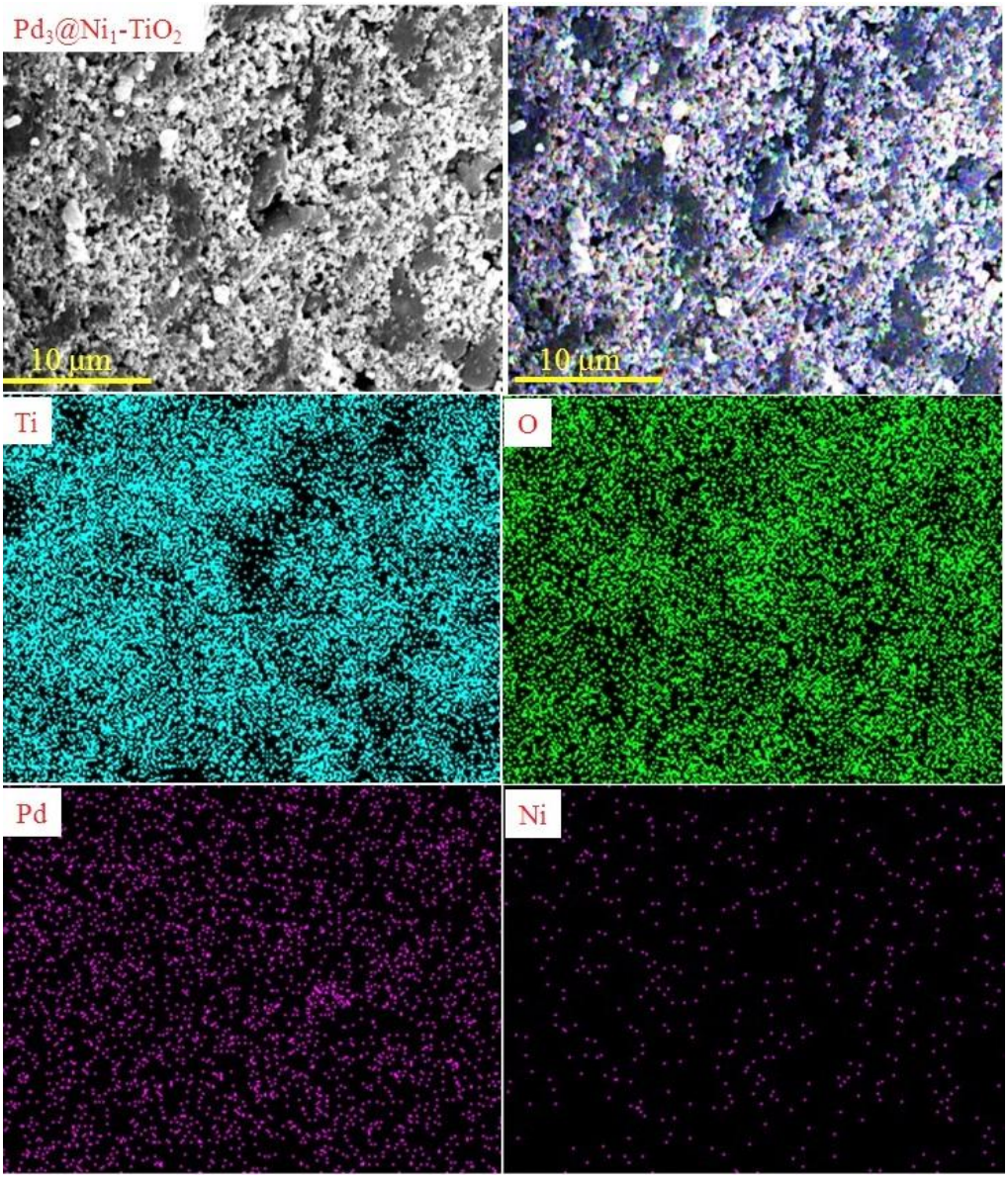

Fig. 2.9: EDS color mapping of different elements present in PNT-3 photocatalyst.

The XPS survey spectrum of PNT-3 (**Fig. 2.10**) showed the existence of Pd, Ni, Ti and O elements resembling with EDS result. The high resolution XPS spectrum of Ti (2p) **(Fig. 2.11 (a)**) consisting of two fitted peaks one at binding energy of 458.4 eV corresponding to $2P_{3/2}$ and other at 464.07 eV ($2P_{1/2}$). The difference between these two peaks is found to be 5.6 eV which is similar with the binding energy reported for the titanium in four oxidation state (Ti^{+4}). In case of O (1s), the spectrum (**Fig. 2.11 (b)**) was fitted to three deconvoluted peaks at 529.8 eV, 531.3 eV and 532.8 eV, these peaks are allocated to crystal lattice oxygen (O_{Ti-O}), O-H (surface hydroxyl group) and adsorbed oxygen (O_2) respectively. Furthermore, the existence of two peaks in the Pd (3d) (**Fig. 2.11 (c)**) centered at 334.7 eV ($3d_{5/2}$), 339.9 eV ($3d_{3/2}$) and with the difference of 5.2 eV suggesting the presence of palladium in its metallic state (Pd^0). Similarly, in case of Ni (2p), two peaks are recorded as shown in (**Fig. 2.11 (d)**. The peak at the binding energy of 852.8 eV corresponds to $3p_{3/2}$ signifying the presence of nickel in zero oxidation state (Ni^0) and another peak at 861.4 eV ($3p_{3/2}$) correlates with nickel in the oxide form [43-45].

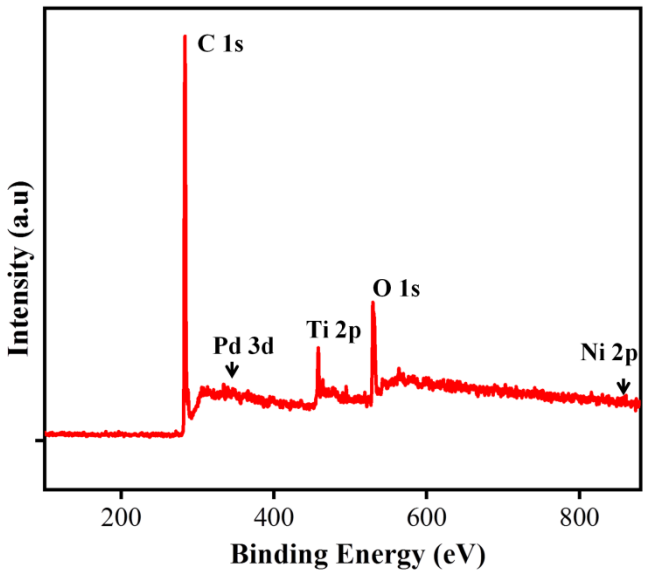

Fig. 2.10: XPS survey spectrum of PNT-3 showing the presence of Pd, Ni, Ti and O elements.

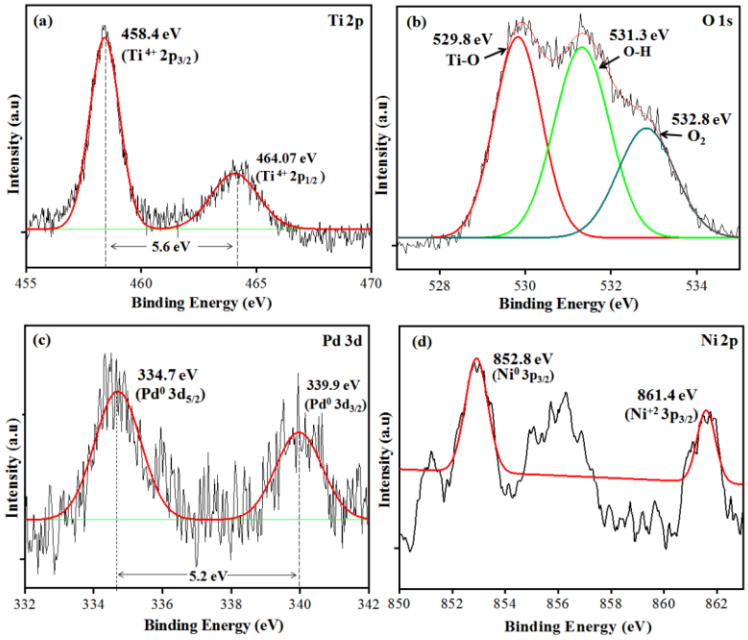

Fig. 2.11: The high resolution XPS spectra of (a) Ti 2p (b) O 1s (c) Pd 3d (d) Ni 2p.

The BET surface analysis of $mTiO_2$ and PNT-3 photocatalyst is shown in **Fig. 2.12.** The mesoporousTiO_2 possessed highest surface area, 421 m^2g^{-1} and pore volume (**Table-2.1**). The nitrogen adsorption-desorption isotherm strictly followed the Type-IV Langmuir characteristics and H1 hysteresis loop which are the uniqueness of the mesoporous materials [33, 46]. The BJH analysis represents (**Fig. 2.12 (b)**) narrow size pore distribution of $mTiO_2$ having a pore diameter in the range 2-10 nm. Similarly, bimetallic doped mesoporous TiO_2 (PNT-3) also followed Type-IV isotherm with surface area, 212 m^2g^{-1} suggesting the mesoporous behavior of the photocatalyst.

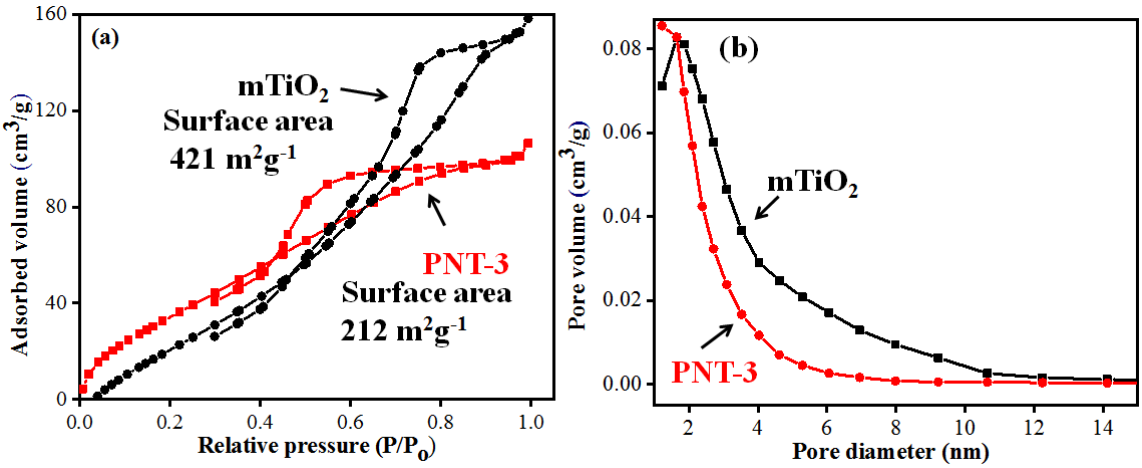

Fig. 2.12: (a) Nitrogen adsorption-desorption curve (b) BJH curve of $mTiO_2$ and PNT-3.

Table-2.1: The surface area, pore volume and pore diameter of different photocatalyst.

S.No.	Photocatalyst	Surface area (m^2g^{-1})	Total Pore Volume (cm^3g^{-1})	Mean Pore diameter (nm)
1	$mTiO_2$	421	0.301	5.479
2	Ni-$mTiO_2$	220	0.688	6.538
3	Pd-$mTiO_2$	312	0.681	8.737
4	PNT-3	212	0.192	3.694

The conversion of benzaldehyde to its corresponding alcohol was determined by comparing the retention time (R_T) and peak area with standard benzaldehyde solution (0.1mM). The samples were drawn periodically, to analyze the reaction products with GC-MS and GC-FID as shown in **Fig. 2.13**. The selective hydrogenation of benzaldehyde was challenging step because a range of intermediates (**Fig. 2.14**) had been formed during the reaction [23, 47]. It was proposed that benzyl alcohol was formed directly from hydrogenation of alcohol (step 1) and toluene was resulted from the subsequent conversion of benzyl alcohol (step 2) and hydrogenolysis of benzaldehyde in step 3 (**Fig. 2.14**). The percentage yield for the toluene formation in our reaction was

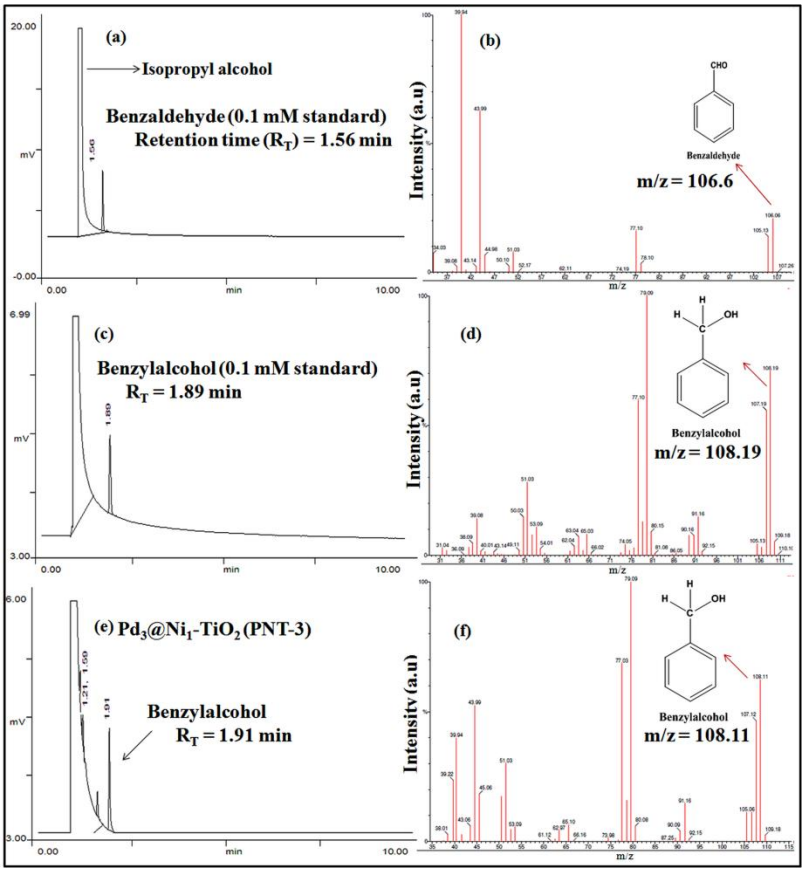

Fig. 2.13: GC-FID spectra with corresponding mass spectrum of (a,b) Standard benzaldehyde (0.1 mM), (c,d) Standard benzyl alcohol (0.1 mM) and (e,f) benzyl alcohol produced with PNT-3.

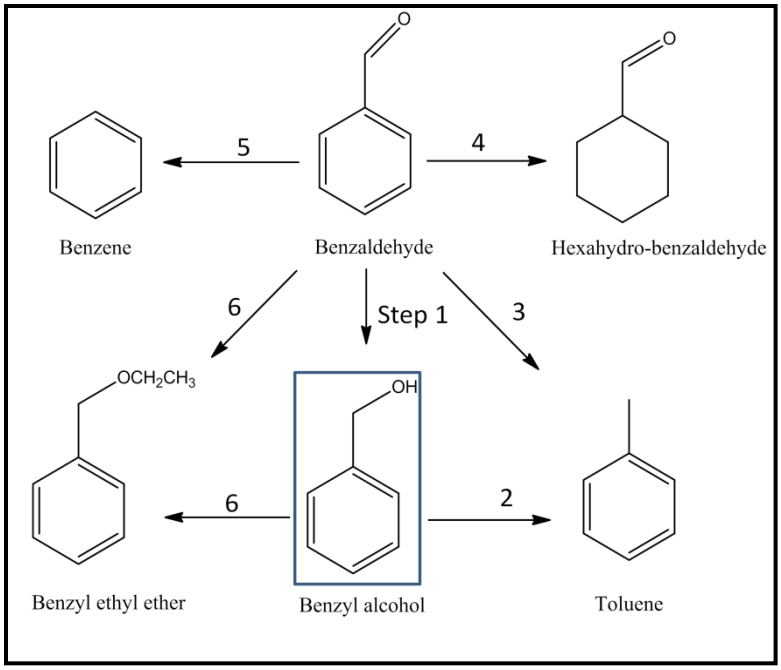

Fig. 2.14: Possible reaction intermediates formed during the hydrogenation of benzaldehyde.

very small ~ 2 % and no other intermediates were observed. Different controlled experiments have been performed like hydrogenation under UV-light, in dark, without catalyst. **Fig. 2.15 (a)** represents the comparative histograms showing the percentage yield obtained for the selective hydrogenation of benzaldehyde to benzyl alcohol with mono/bimetallic-mTiO_2 composites in dark and UV-light radiation under hydrogen atmosphere. It has been observed that no hydrogenation of benzaldehyde occurred in the absence of catalyst and without mTiO_2 support bimetallic Pd@Ni showed a percentage yield of ~23 % which is higher than their corresponding monometallic analogues. The bimetallic impregnated mTiO_2 (PNT-3) photocatalyst displayed higher conversion for the benzaldehyde to benzyl alcohol (28 %) in dark might be due to the increased exposed surface area of the catalyst. But under saturated H_2 atmosphere and UV-light radiation PNT-3 photocatalyst showed higher conversion of benazaldehyde (91%) and selectivity (**Table-2.2**) comparative to PNT-2, PNT-1, and their monometallic analogues. **Fig. 2.15 (b)** represent the time course study showing the amount of benzaldehyde (μmol) remain left using bare, mono and bimetallic (PNT-3) mTiO_2 photocatalyst.

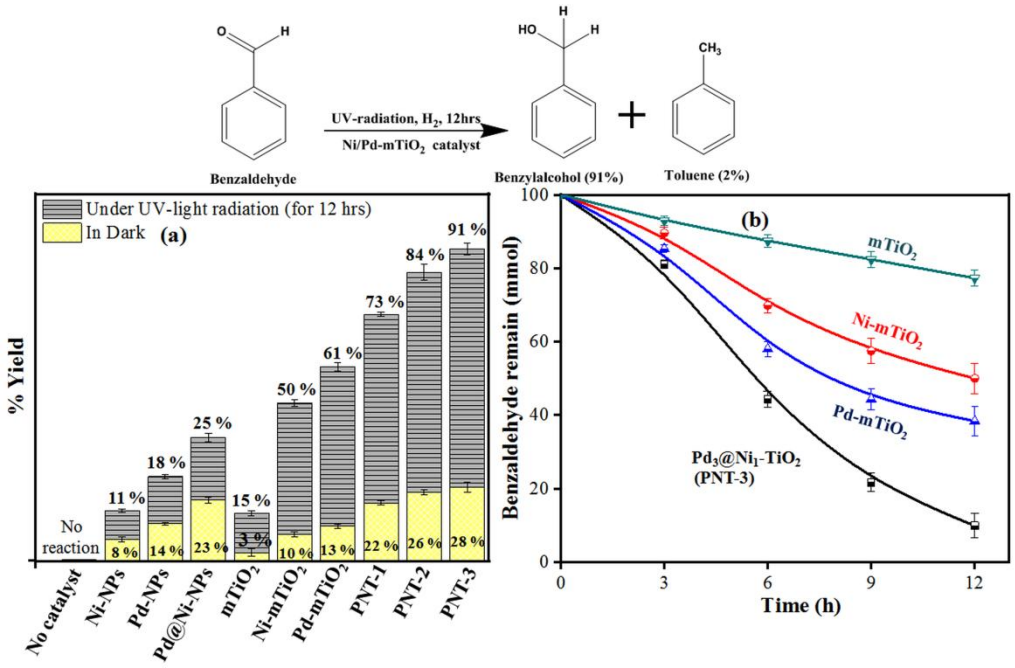

Fig. 2.15: (a) Percentage yield obtained for the hydrogenation of benzaldehyde in dark and UV-light radiation (b) showing the amount of benzaldehyde (μmol) remain with respect to time using bare, mono/bimetallic (PNT-3) mTiO_2 photocatalyst.

Table-2.2: The percentage yield and selectivity obtained for the hydrogenation of benzaldehyde with different nanocatalysts.

S No.	Photocatalyst	Reaction Time (h)	Yield (%)	Selectivity (%)
1	TiO_2	12	15	27
2	Ni-TiO_2	12	50	49
3	Pd-TiO_2	12	61	66
4	PNT-1 (Pd_1@Ni_1-TiO_2)	12	73	84
5	PNT-2 (Pd_2@Ni_1-TiO_2)	12	84	89
6	PNT-3 (Pd_3@Ni_1-TiO_2)	12	91	96

To confirm whether the higher yield for the benzyl alcohol formation with PNT-3 and PNT-2 photocatalyst was either due to the increasing concentration of Pd or synergistic effect of Pd@Ni doped on $mTiO_2$. The benzaldehyde hydrogenation was examined with $mTiO_2$ impregnated with 2 and 3 weight percent of Pd nanoparticles. The histogram showing the percentage yield for the reaction found to be almost similar (**Fig. 2.16**). This result suggested that electronic interactions occurred at bimetallic-$mTiO_2$ interface promoted the hydrogenation of benzaldehyde. The reaction kinetics of benzaldehyde reaction

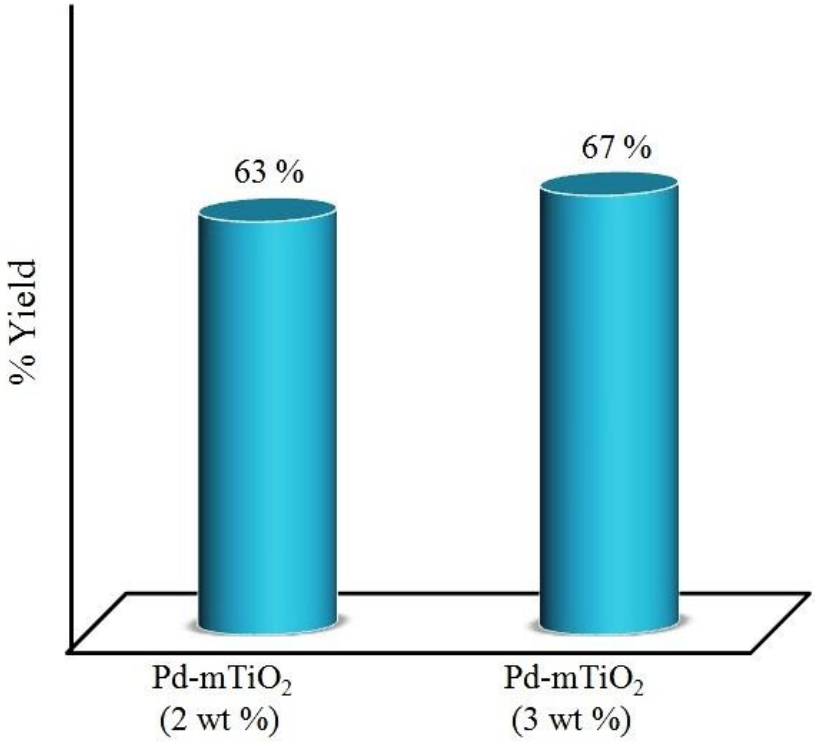

Fig. 2.16: Histogram showing the percentage yield for the hydrogenation of benzaldehyde.

have been determined using the equation

$r = -dC/dt = k(KC)/(1+KC)$

(r = rate, k = kinetic constant, K = adsorption equilibrium constant and C = concentration)

The selective hydrogenation reaction followed the pseudo first order kinetics. The reaction rate (**Fig. 2.17**) found to be maximum for the bimetallic-$mTiO_2$ (PNT-3) nanocomposite i.e. ($k = 5.37 \times 10^{-1}\ h^{-1}$) as compared to monometallic Pd-$mTiO_2$ ($2.20 \times 10^{-1}\ h^{-1}$), Ni-$mTiO_2$ ($1.49 \times 10^{-1}\ h^{-1}$) followed by bare $mTiO_2$ ($0.47 \times 10^{-1}\ h^{-1}$) The photocatalytic efficiency of synthesized Pd/Ni-$mTiO_2$ nanocomposites for the selective hydrogenation was further explored by using two different benzaldehyde substrate i.e. 4-nitrobenzaldehyde (4-NBZ) and 4-hydroxybenzaldehyde (4-HBZ). It was observed that bimetallic-$mTiO_2$ photocatalyst exhibited higher catalytic efficiency relative to their monometallic counterparts and bare TiO_2 for the hydrogenation of both 4-NBZ and 4-HBZ and displayed higher percentage yield (93%) for the reaction followed by PNT-2 > PNT-1 > Pd-$mTiO_2$ > Ni-$mTiO_2$ > $mTiO_2$ as shown in **Fig. 2.18**. Similarly, time course study and histogram showing percentage yield for the hydrogenation of 4-

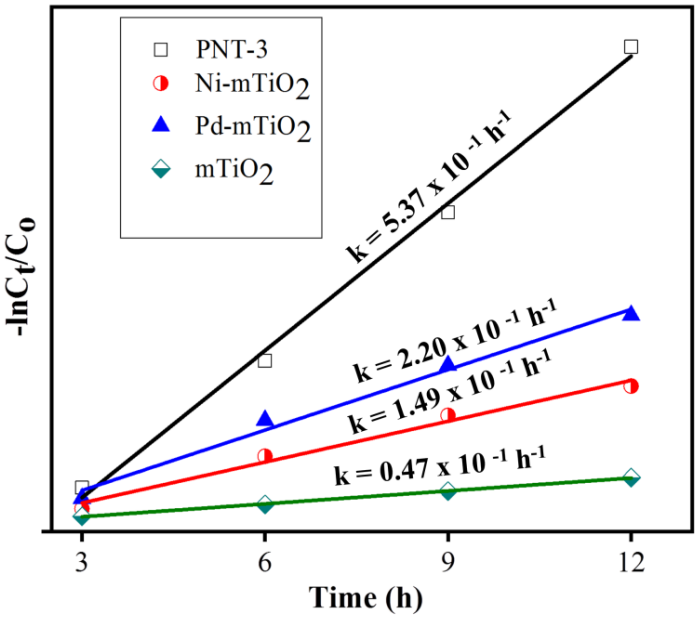

Fig. 2.17: Rate constant obtained for hydrogenation of benzaldehyde in UV-light.

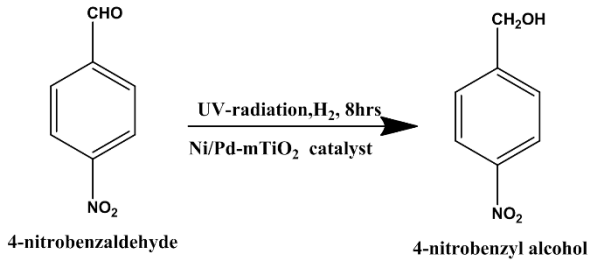

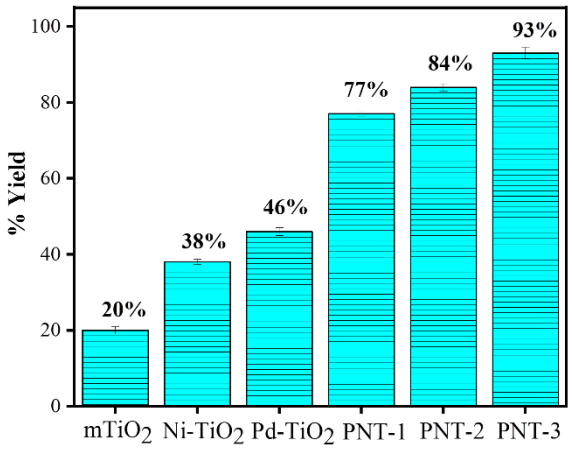

Fig. 2.18: Percentage yield for the hydrogenation of 4-NBZ.

hydroxybenazaldhyde as shown in the **Fig. 2.19**. The observed trend for the hydrogenation 4-HBZ followed the order PNT-3 > PNT-2 > PNT-3 having percentage yield for 4-HBA 83 %, 72 %, and 58 % respectively, higher than the monometallic ones. The results obtained from the hydrogenation of 4-NBZ and 4-HBZ signified that the presence of electron withdrawing group (NO_2) increase the rate of hydrogen transfer reaction and electron releasing group (OH) attached to the aldehyde reduces the reaction rate in the presence of secondary alcohol (isopropyl alcohol) [31].

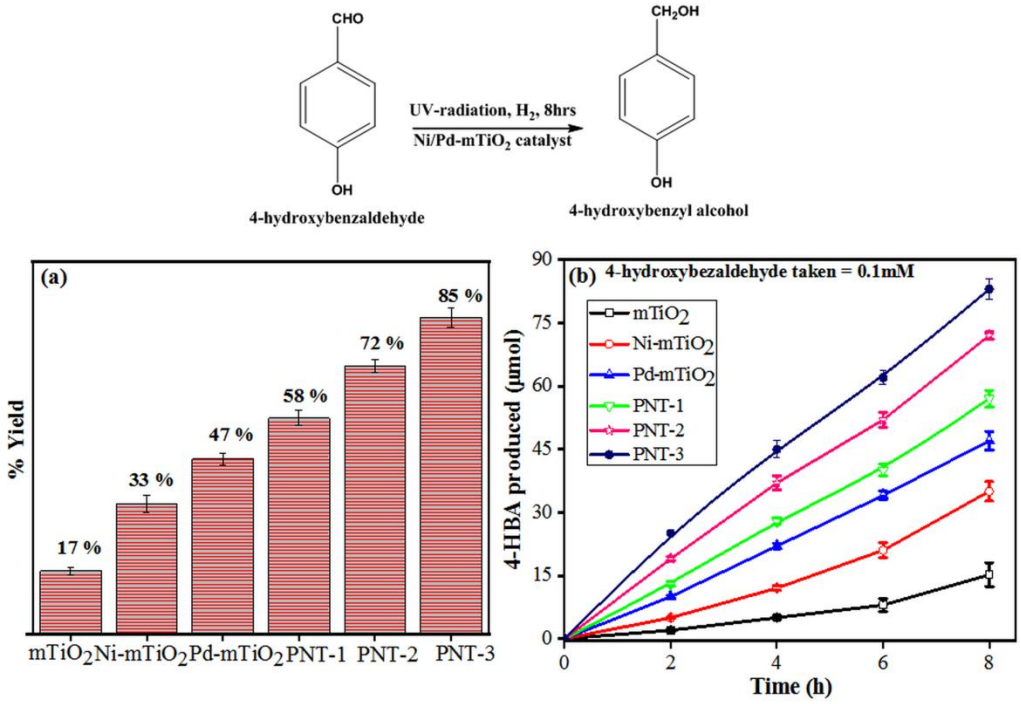

Fig. 2.19: (a) Percentage yield obtained for the hydrogenation of 4-HBZ (b) time course study.

Mechanism for the photocatalytic hydrogenation reaction

Based on the earlier findings [48, 49], the most probable mechanism followed by the photocatalytic hydrogenation reaction is shown in **Scheme-2.2**. When photocatalyst illuminated with UV-radiation, the electrons from the VB (valence band) of $mTiO_2$ are excited to their respective CB (conduction band). The metal-doped on $mTiO_2$ acts as a hetero-junction for the excited electrons. These electrons are transferred from CB of $mTiO_2$ to mono/bimetallic surface results in the formation of radical ($RCH^{\cdot}O^{-}$). The second electron transfer leads to the formation of $RCH^{-}OH$ which easily transform into benzyl alcohol. As reported by S.O. Flores *et al.* [48] and B. Pal *et al.* [49] the holes (h^{+}) generated in the valence band (VB) of $mTiO_2$ oxidize the isopropyl alcohol to acetone and provide H^{+} for the hydrogenation of benzaldehyde. The

saturated hydrogen atmosphere (through hydrogen balloon) further enhances the photocatalytic efficiency of bimetallic nanocatalysts. Therefore, bimetallic PNT-3 photocatalyst is highly active in the presence of H_2 atmosphere. Moreover, the superior catalytic activity of bimetallic nanocomposites relative to monometallic ones arise due to reduction in barrier height and enhancement in the lifetime of charge carries which promotes efficient charge transfer from the CB of $mTiO_2$ and enriches the electron density over the Pd@Ni reaction active center [18, 39, 50].

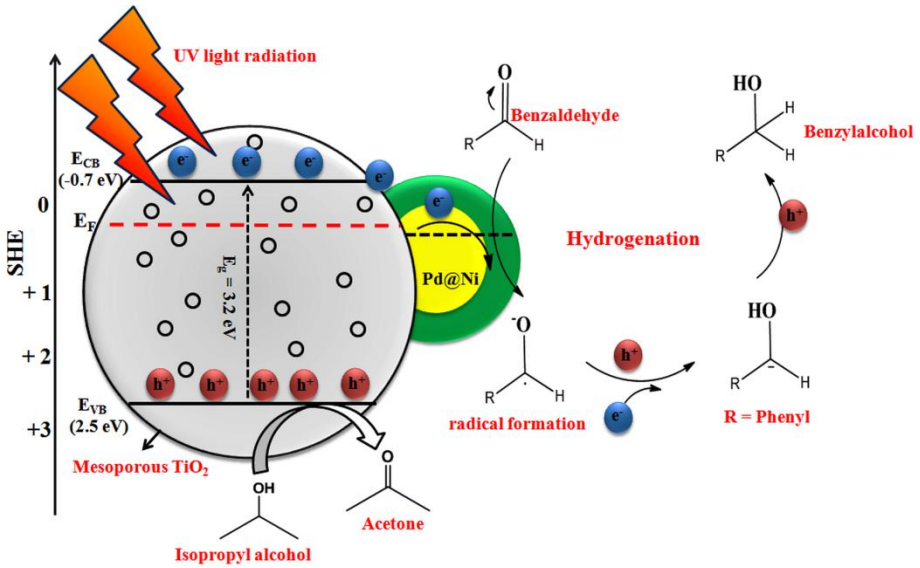

Scheme 2.2: Possible mechanism scheme for the photocatalytic hydrogenation.

Moreover, the heterogeneous catalysis is more preferred over the homogeneous catalysis because of its reusability and long-term stability. The photocatalytic stability of PNT-3 was determined by its reusability for the five consecutive cycles. The recycling test was performed for the hydrogenation of benzaldehyde under UV-irradiation and hydrogen atmosphere. After the reaction the photocatalyst was separated with the centrifuge and washed, dried and reused for further experiment under same photochemical conditions. No considerable loss in the activity of the recycled PNT-3 photocatalyst was observed after five repeated cycles

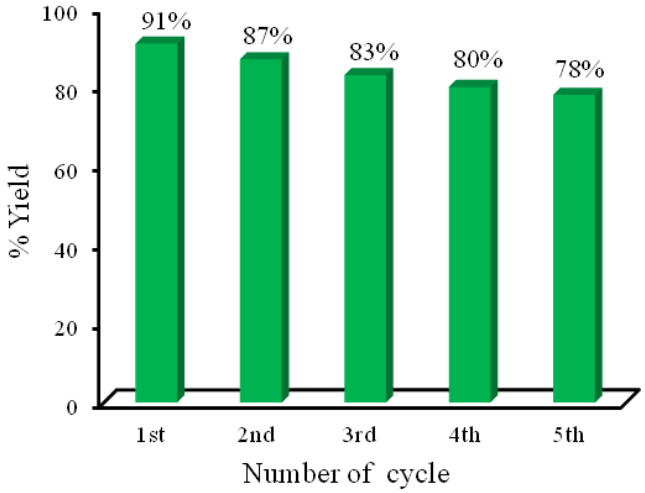

Fig. 2.20: Reusability of the photocatalyst PNT-3 for five successive cycles.

suggesting the long-term stability for the hydrogenation of C=O group. However, the minor loss in activity (**Fig. 2.20**) arises due to the fact that some amount of catalyst has been lost during its washing process or blockage in the catalytic active sites of the catalyst.

References

[1] A.-G. Boudjahem, A. Redjel, T. Mokrane, J. Ind. Eng. Chem.18 (2012) 303-308.

[2] B. Li, G.-S. Hu, L.-Y. Jin, X. Hong, J.-Q. Lu, M.-F. Luo, J. Ind. Eng. Chem.19 (2013) 250-255.

[3] H.-y. Jiang, S.-s. Zhang, B. Sun, Catal. Lett. 148 (2018) 1336-1344.

[4] R.L. Oliveira, C.S. Oliveira, R. Landers, C.R. Correia, ChemistrySelect 3 (2018) 535-543.

[5] Y. Ping, J. Zhang, T. Xing, G. Chen, R. Tao, K.-H. Choo, J. Ind. Eng. Chem. 58 (2018) 74-79.

[6] S. Kang, K.S. Yoo, Y. Chung, Y. Kwon, J. Ind. Eng. Chem., 62 (2018) 329-332.

[7] Q. Wu, C. Zhang, B. Zhang, X. Li, Z. Ying, T. Liu, W. Lin, Y. Yu, H. Cheng, F. Zhao, J. Colloid Interface Sci. 463 (2016) 75-82.

[8] J. Xia, G. He, L. Zhang, X. Sun, X. Wang, Appl. Catal., B 180 (2016) 408-415.

[9] A. Bathla, B. Pal, ChemistrySelect 3 (2018) 4738-4744.

[10] L. Liu, F. Gao, P. Concepción, A. Corma, J. Catal. 350 (2017) 218-225.

[11] S. Rana, S.B. Jonnalagadda, RSC Adv. 7 (2017) 2869-2879.

[12] P. Natarajan, H.A. Khan, S. Yoon, K.-D. Jung, J. Ind. Eng. Chem. 63 (2018) 380-390.

[13] S. Cattaneo, S.J. Freakley, D.J. Morgan, M. Sankar, N. Dimitratos, G.J. Hutchings, Catal. Sci. Technol. 8 (2018) 1677-1685.

[14] A. Monga, A. Bathla, B. Pal, Sol. Energy, 155 (2017) 1403-1410.

[15] A. Monga, R.A. Rather, B. Pal, Sol. Energy Mater. Sol. Cells, 172 (2017) 285-292.

[16] L. Rout, A. Kumar, R.S. Dhaka, G.N. Reddy, S. Giri, P. Dash, Appl. Catal., A 538 (2017) 107-122.

[17] C.-H. Liu, R.-H. Liu, Q.-J. Sun, J.-B. Chang, X. Gao, Y. Liu, S.-T. Lee, Z.-H. Kang, S.-D. Wang, Nanoscale 7 (2015) 6356-6362.

[18] A. Monga, B. Pal, Colloids Surf., A 481 (2015) 158-166.

[19] Y. Chen, H. Lim, Q. Tang, Y. Gao, T. Sun, Q. Yan, Y. Yang, Appl. Catal., A 380 (2010) 55-65.

[20] T. Jayesh, K. Itika, G.R. Babu, K.R. Rao, R. Keri, A.H. Jadhav, B. Nagaraja, Catal. Commun. 106 (2018) 73-77.

[21] M. Glatz, B. Stöger, D. Himmelbauer, L.F. Veiros, K. Kirchner, ACS Catal. 8 (2018) 4009-4016.

[22] M. Han, H. Zhang, Y. Du, P. Yang, Z. Deng, React. Kinet. Mech. Catal. 102 (2010) 393-404.

[23] R.M. Mironenko, O.B. Belskaya, T.I. Gulyaeva, M.V. Trenikhin, A.I. Nizovskii, A.V. Kalinkin, V.I. Bukhtiyarov, A.V. Lavrenov, V.A. Likholobov, Catal. Today 279 (2017) 2-9.

[24] X. Jiang, N. Koizumi, X. Guo, C. Song, Appl. Catal., B 170 (2015) 173-185.

[25] S. Fu, C. Zhu, Q. Shi, H. Xia, D. Du, Y. Lin, Nanoscale 8 (2016) 5076-5081.

[26] X. Fu, Y. Liu, W. Yao, Z. Wu, Catal. Commun. 83 (2016) 22-26.

[27] L. Luo, Z. Duan, H. Li, J. Kim, G. Henkelman, R.M. Crooks, J. Am. Chem. Soc. 139 (2017) 5538-5546.

[28] J. Zhang, K. Gao, S. Wang, W. Li, Y. Han, RSC Adv. 7 (2017) 6447-6456.

[29] C.-H. Hao, X.-N. Guo, Y.-T. Pan, S. Chen, Z.-F. Jiao, H. Yang, X.-Y. Guo, J. Am. Chem. Soc. 138 (2016) 9361-9364.

[30] L. Fu, W. Cai, A. Wang, Y. Zheng, Mater. Lett. 142 (2015) 201-203.

[31] P. Sharma, Y. Sasson, Green Chem.19 (2017) 844-852.

[32] R.A. Rather, S. Singh, B. Pal, Appl. Catal., B 213 (2017) 9-17.

[33] R.A. Rather, S. Singh, B. Pal, J. Catal. 346 (2017) 1-9.

[34] J. Archana, S. Harish, M. Sabarinathan, M. Navaneethan, S. Ponnusamy, C. Muthamizhchelvan, M. Shimomura, H. Ikeda, D. Aswal, Y. Hayakawa, RSC Adv. 6 (2016) 68092-68099.

[35] Z.-Q. Li, Y.-P. Que, L.-E. Mo, W.-C. Chen, Y. Ding, Y.-M. Ma, L. Jiang, L.-H. Hu, S.-Y. Dai, ACS Appl. Mater. Interfaces 7 (2015) 10928-10934.

[36] T. Sreethawong, S. Yoshikawa, Catal. Commun. 6 (2005) 661-668.

[37] Y. Liu, Z. Wang, W. Fan, Z. Geng, L. Feng, Ceram. Int. 40 (2014) 3887-3893.

[38] N. Zhang, S. Liu, X. Fu, Y.-J. Xu, J. Phys. Chem. C 115 (2011) 9136-9145.

[39] J. Kaur, R. Singh, B. Pal, J. Mol. Catal., A 397 (2015) 99-105.

[40] J. Prakash, P. Kumar, R. Harris, C. Swart, J. Neethling, A.J. van Vuuren, H. Swart, Nanotechnology 27 (2016) 355707.

[41] D.K. Pallotti, L. Passoni, P. Maddalena, F. Di Fonzo, S. Lettieri, J. Phys. Chem. C, 121 (2017) 9011-9021.

[42] S. De, J. Zhang, R. Luque, N. Yan, Energy Environ. Sci. 9 (2016) 3314-3347.

[43] C. Su, L. Liu, M. Zhang, Y. Zhang, C. Shao, CrystEngComm. 14 (2012) 3989-3999.

[44] A.L. Luna, D. Dragoe, K. Wang, P. Beaunier, E. Kowalska, B. Ohtani, D. Bahena Uribe, M.A. Valenzuela, H. Remita, C. Colbeau-Justin, J. Phys. Chem. C 121 (2017) 14302-14311.

[45] N. Chen, D. Deng, Y. Li, X. Liu, X. Xing, X. Xiao, Y. Wang, Sci. Rep. 7 (2017) 7692.

[46] R.A. Rather, D. Pooja, P. Kumar, S. Singh, B. Pal, J. Cle. Pro. 175 (2018) 394-401.

[47] N. Perret, F. Cárdenas-Lizana, M.A. Keane, Catal. Commun. 16 (2011) 159-164.

[48] S. Flores, O. Rios-Bernij, M. Valenzuela, I. Córdova, R. Gómez, R. Gutiérrez, Topics in Catal. 44 (2007) 507-511.

[49] S. Singh, R. Prajapat, R.A. Rather, B. Pal, Arab. J. Chem. (2018).

[50] W.G. Menezes, B. Neumann, V. Zielasek, K. Thiel, M. Bäumer, ChemPhysChem. 14 (2013) 1577-1581.

CHAPTER- 3

Enhanced co-catalysis of bimetallic Cu(core)@Zn(shell) imparted to (001) faceted TiO_2 for selective quinoline hydrogenation

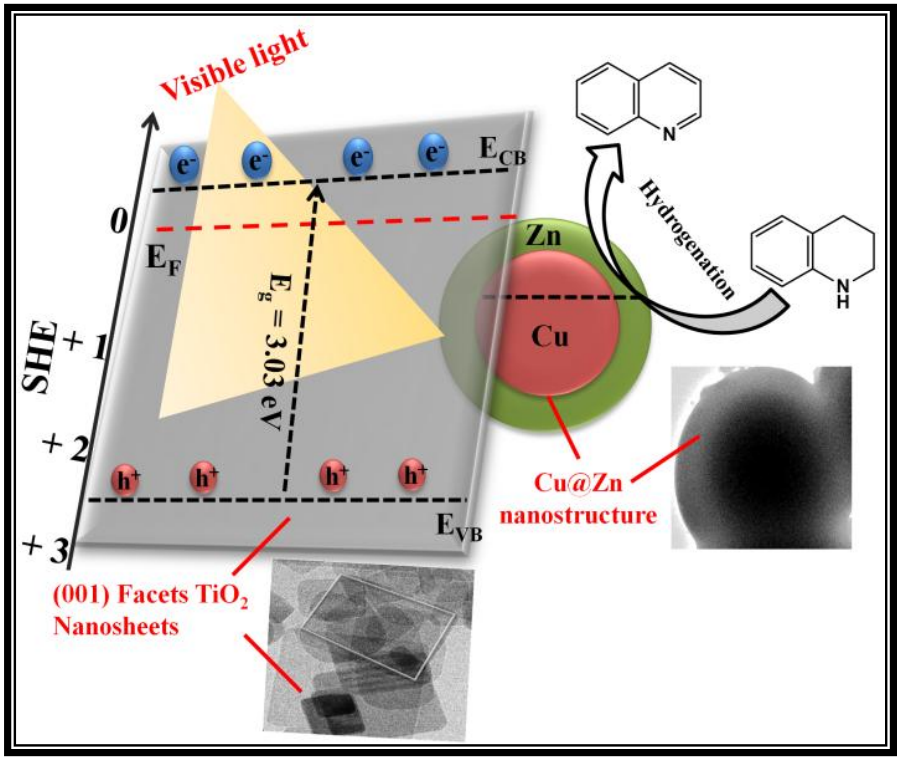

Schematic outline

The present study demonstrated the synthesis of bimetallic Cu(core)@Zn(shell) nanostructures based on their galvanic interactions. The Cu@Zn nanostructures were used as co-catalyst after impregnated on (001) faceted titania nanosheets for selective hydrogenation of quinoline under visible light radiation. The Cu@Zn/TiO_2 photocatalyst exhibited superior activity than bare Cu@Zn and other monometallic counterparts. The synergistic interaction between the two metals at bimetallic-TiO_2 interface promotes electron and hydride ion (H^-) transfer for quinoline hydrogenation compared to monometallic-TiO_2 nanocomposites.

3.1 Introduction

The bimetallic core@shell nanostructures (NS) composed of two different galvanic metals (Pd, Au, Ni, Zn, Cu, and Ag) have aroused tremendous attention in the area of catalysis, photocatalysis, and electronics [1-7]. The core@shell nano-arrangement exhibited fascinating electronic, optical and surface properties [8-12] due to synergistic interaction between two metals relative to their individual monometallic components. A variety of methods have been employed by different researchers, but one pot co-reduction method based on galvanic interaction between the metals is a promising method to synthesize core@shell nanoparticles [13-16]. In this method, reduction potential (E^o value) of two metals played a decisive role in the final structural design. In the presence of weak reducing agent (glucose, ascorbic acid etc.) the two metals were reduced in consecutive order based on their reduction potential values. H. Jiang *et al*. [17] reported the synthesis of bimetallic Au@Ag NS via galvanic interaction between two soluble metal salts ($AgCl_2$ and $HAuCl_4$) arise due to difference in their E^o values ($E^0_{Ag+/Ag}$ = +0.80 eV Vs SHE; $E^0_{Au3+/Au}$ = +0.93 eV Vs SHE). C. Xu et *al.* [18] reported the synthesis of nanoporous bimetallic core@shell structure of Cu and Pt based on their galvanic interaction. Similarly, A. Sarkar *et al*. [19] reported the synthesis of bimetallic core-shell (Pt@Cu) NS by galvanic displacement between copper and platinum for the oxygen reduction reaction in fuel cells.

The selective hydrogenation of N-heteroarenes is a crucial step for various pharmaceutical and petrochemical industries in the manufacturing of different fine products [20-23]. The conversion of quinoline (Qu) to 1,2,3,4-tetrahydroquinoline is a challenging task as it involves the breaking of aromaticity of the molecule. Different transition metal (Ir, Rh, Ru, Co, Cu, Zn, Ni, Fe) or supported metal based catalysts [23-28] have been employed for the selective hydrogenation of quinoline. S. Li *et al*. [29] reported the catalytic hydrogenation of quinoline to 1,2,3,4-tetrahydroquinoline at room temperature using Pt nanoparticles supported on TiO_2. Y. Gong *et al*. [30] reported Pd@ompg-C_3N_4 as an effective catalyst for the selective hydrogenation of quinoline under mild conditions. Although these metal nanocatalysts are highly active and showed superior catalytic efficiency, still there is a gap in order to accomplish the desired selectivity for the quinoline hydrogenation. These selectivity requirements could be improved by using core@shell NS consisting of two different metals. Y. Chen *et al*. [31] reported that bimetallic Cu@Ru nanocrystal exhibited superior catalytic efficiency towards regioselective

hydrogenation of quinoline compared to bare Cu and Ru nanocatalysts. S. Zhang *et al*. [32] reported the selective hydrogenation of halogenated quinolines using bimetallic Au-Pd nanocatalyst supported on CeO_2 nanorods. It was observed that $Au_{1-x}Pd_x$ having low Pd composition showed enhanced selectivity for the halogenated quinolines. Similarly, I. Sorribes *et al.* [33] reported the synthesis of nano-layered Co-Mo/S as highly chemo/regioselective catalyst for quinoline hydrogenation.

These bimetallic nanostructures (NS) (Au@Ag, Pd@Ni Cu@Zn, Au@Cu and combination of different metals) [7, 34-37] are effectively used as good co-catalysts after impregnation on the surface of suitable semiconductor material. Out of various semiconductors (001) faceted anatase TiO_2 captures huge attention in the area of photocatalysis and other organic transformation reactions like oxygen reduction reaction, hydrogenation of carbonyl compounds, and different biological activities [38-47]. The (001) faceted TiO_2 surface exhibited higher catalytic exposed active sites and showed enhanced photoactivity compared to thermodynamically stable (101) faceted TiO_2 nanoparticles. The deposition of different metals on the surface of TiO_2 (001) further enhanced the photocatalytic efficiency of TiO_2. W. Wang *et al.* [48] reported the synthesis of ultrathin (001) facets TiO_2 nanosheets on graphene for the photocatalytic degradation of methylene blue under visible light radiation. R. Rather *et al.* [49] reported the co-deposition of Au and Pt on (001) facets TiO_2 nanosheets for photoreduction of water under sunlight radiation. The photocatalytic hydrogenation of unsaturated compounds using bimetallic-TiO_2 nanocomposites under light radiation are not much investigated.

In this regard, the present work outlines the synthesis of Cu, Zn and Cu@Zn nanostructure (NS) on the basis of galvanic interaction that takes place between the two metal salts. These nanocatalysts were examined for the selective hydrogenation of quinoline and observed that bimetallic Cu@Zn displayed superior activity than bare Zn and Cu nanoparticles. However, when these NS were used as co-catalyst after impregnation on as-prepared (001) faceted TiO_2 nanosheets, the Cu@Zn/TiO_2 showed enhanced activity and selectivity towards the quinoline conversion under visible light. The hydrogenation reaction was analyzed using different controlled experiments (under visible light, with H_2, without H_2, and under dark conditions). In general, the quinoline hydrogenation occurs in very harsh conditions (required high temperature, solvents and bases). Therefore, Cu@Zn/TiO_2 nanocomposite could be an effective photocatalyst for the selective quinoline hydrogenation.

3.2 Experimental

3.2.1 Chemical and Regents

$ZnCl_2$ (zinc chloride), $CuCl_2.2H_2O$ (cupric chloride dehydrate), $C_6H_{12}O_6$ (D-glucose), NaOH (sodium hydroxide) and C_7H_8 (toluene) were acquired from Loba Chemie (India). Quinoline (Qu), 1,2,3,4-tetrahydroquinoline (THQu), 8-hydroxyquinoline (8-HQu), 1,2,3,4-tetrahydroquino-8-ol (8-HTHQ), 8-methylquinoline (8-MQu), 8-methyl-1,2,3,4-tetrahydroquinoline (8-MTHQ) were obtained from Sigma-Aldrich (India) and all other chemicals were used without any additional modification.

3.2.2 Synthesis of Zn, Cu and Cu@Zn core-shell nanostructures

In a typical procedure, $CuCl_2.2H_2O$ (0.03 M) and $ZnCl_2$ (0.03 M) were added to 20 ml of pre-synthesized aqueous gelatin solution (15 mg/10 ml) in 50 ml in round bottom flask. The mixture was maintained under continuous magnetic stirring for 30 min to make a homogenous solution of different salts. The pH of the solution was maintained within the range of 8-9 by drop-wise addition of 0.5 M NaOH solution. The reduction of copper metal on the surface of zinc metal was initiated with the addition of 1M glucose (5 ml) solution acting as a weak reducing agent. The resulting solution was kept under ultrasonic treatment until the color of the solution changed from blue to a brown color indicating the formation of bimetallic Cu@Zn core-shell nanostructure. The different type of core@shell nanocatalysts were prepared by varying the Cu:Zn weight ratio as 1:1, 2:1, 3:1 and abbreviated as $Cu_1@Zn_1$, $Cu_2@Zn_1$, and $Cu_3@Zn_1$ respectively. The final suspension was centrifuged, washed several times with water and ethanol and then dried at room temperature.

As stated above, a similar procedure was followed to synthesize Cu and Zn nanoparticles. $CuCl_2.2H_2O$ (0.03 M) or $ZnCl_2$ (0.03 M) was added to 20 ml of pre-synthesized gelatin solution (15 mg/10 ml) respectively. The solution was maintained under magnetic stirring for 30 min followed by dropwise addition of 0.5 M NaOH solution to maintain the pH of the solution ~8 or 9. After that 5 ml of glucose (1 M) solution was added to the mixture in order to initiate the reduction of the metal salt. The resulting solution was kept under ultrasonic treatment until the color of the solution changed from blue to brown color (in case of Cu) and formation of a white precipitate (in case of Zn) indicating the formation Cu and Zn nanoparticles respectively. The final suspension was centrifuged, washed with ethanol and then dried at room temperature.

3.2.3 Synthesis of (001) facet TiO_2 nanosheets

The (001) faceted TiO_2 nanosheets were synthesized by hydrothermal approach [49, 50] using $Ti(OBu)_4$ as a precursor. In a typical procedure, titanium butoxide (20 ml) was added to 75 ml Teflon lined stainless steel autoclave followed by direct addition of 4 ml of hydrofluoric (HF) acid. The solution was kept in a muffle furnace for heat treatment at 200 ^oC for 24 h. After hydrothermal treatment, the precipitates were centrifuged and washed several times with water, ethanol and dried at room temperature.

3.2.4 Fabrication of Cu/Zn-TiO_2 nanocomposites

The fabrication of Cu@Zn-TiO_2 and Cu-TiO_2, Zn-TiO_2 was done by wet impregnation method (**Scheme-3.1**) [7]. In a standard procedure, 200 mg of pre-synthesized titanium oxide was dispersed in 20 ml of water followed by the addition of the desired amount (1 wt% with respect to TiO_2) of mono/bimetallic nanoparticles. The solution was kept under magnetic stirring for 24 h. The resulting solution was centrifuged, washed and dried at room temperature to get desired metal-TiO_2 nanocomposites. The bimetallic-TiO_2 nanocomposites having different Cu:Zn ratio (1:1, 2:1 and 3:1) abbreviated as ZCT-1, ZCT-2, and ZCT-3 where ZCT is Cu@Zn-TiO_2 nanocomposite.

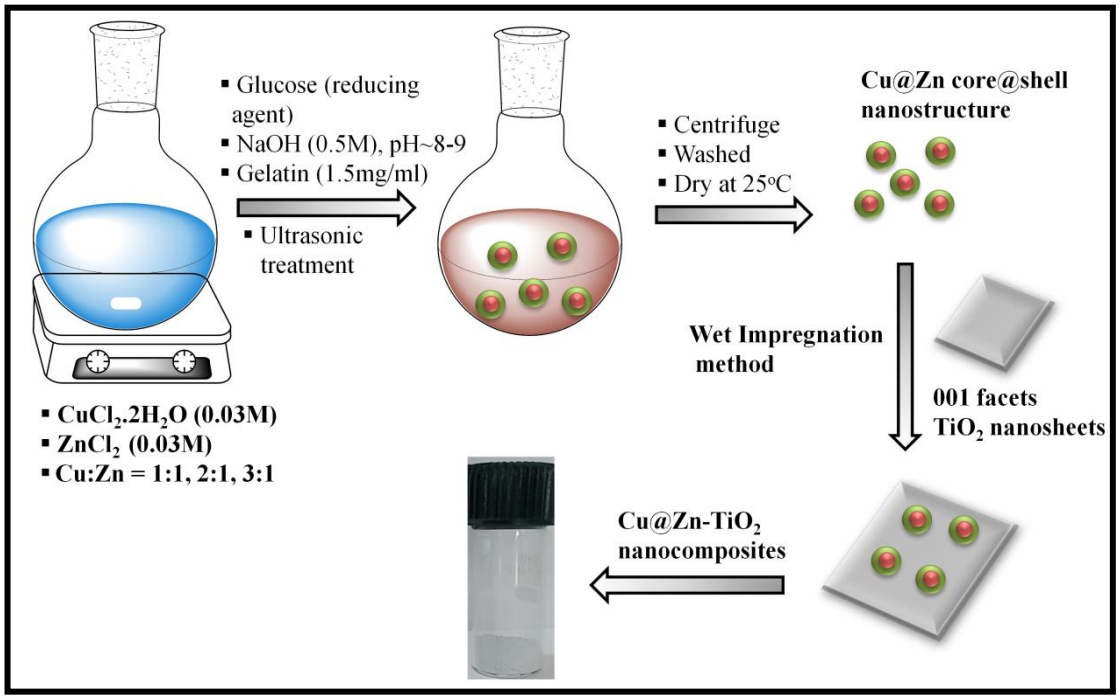

Scheme-3.1: Schematic description of synthesized bimetallic Cu@Zn-TiO_2 nanocomposite.

3.2.5 Characterization and Photocatalytic activity

The characterization of as-prepared photocatalysts by different techniques has already been described in chapter-1 and chapter-2.

The selective hydrogenation of quinoline was carried out in a photocatalytic reactor containing 0.1 mM quinoline in 20 ml of toluene. The reactor was illuminated with visible lamp (125W halogen lamp at 400-800 nm) followed by the addition 10 mg of as-prepared catalyst under continuous magnetic stirring. It was observed that various photocatalytic hydrogenation reactions showed enhanced catalytic efficiency and selectivity under saturated hydrogen atmosphere. Thus, in order to sustain saturated hydrogen (H_2) atmosphere inside the reactor, we have used H_2 balloon at the top of the reactor. The reactor temperature was maintained constant as the water continuously flows throughout the reactor. The final hydrogenated product was identified with GC-MS (Bruker) and further analyzed with gas chromatography (Nucon) equipped with a flame ionization detector (FID) and capillary column (BR-1ms). The oven temperature was varied from 120 ^{o}C to 260 ^{o}C with 10 ^{o}C rise/min and keeping the temperature of the detector and injector constant at 350 ^{o}C and 250 ^{o}C respectively.

3.3 Results and discussion

The average hydrodynamic size of synthesized Zn, Cu, and Cu@Zn nanocatalysts (**Fig. 3.1 (a)**) was measured by dissolving or dispersing 5 mg of catalyst in 10 ml of distilled water using ultrasonication treatment for 1 h. The hydrodynamic size of Cu and Zn nanoparticles was found to be 114 nm and 169 nm respectively. In case of Cu@Zn having Cu:Zn weight ratio 1:1, the average size was found to be 198 nm. It was observed that with increasing Cu weight ratio, the hydrodynamic size increased from 230 nm to 267 nm for Cu@Zn (2:1) and Cu@Zn (3:1) respectively. The optical absorption analysis (**Fig. 3.2 (b)**) revealed that Zn nanoparticles showed

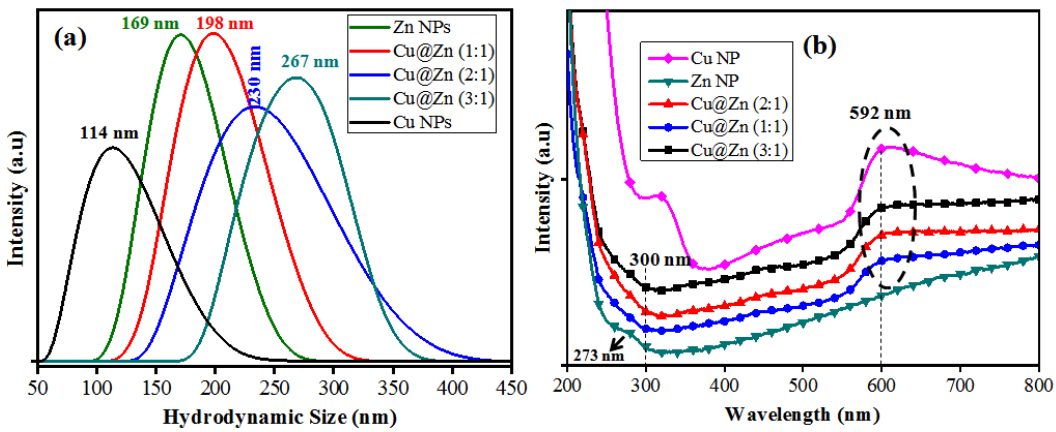

Fig. 3.1: (a) The average hydrodynamic size (b) optical absorption spectra of mono and bimetallic Cu@Zn nanostructures.

an absorption edge at 273 nm. A significant red shift in absorption edge (300 nm) was observed in case of bimetallic Cu@Zn NS having Cu:Zn weight ratio 1:1 and a new absorption maxima was also observed at 592 nm due to surface plasmon resonance (SPR) effect or coherent oscillations of surface electrons of Cu. The absorption maxima observed at 592 nm was slightly blue shifted from 595 nm to 592 nm with respect to pure Cu nanoparticles. It was observed that with the increasing weight ratio of Cu with respect to Zn, the intensity of SPR absorption maxima also increases. **Fig. 3.2** represents the DRS spectra of bare TiO_2 nanosheets and Zn/Cu-TiO_2 nanocomposites. **Fig. 3.3** (a–c) represents the TEM images of synthesized Cu@Zn nanoparticles.

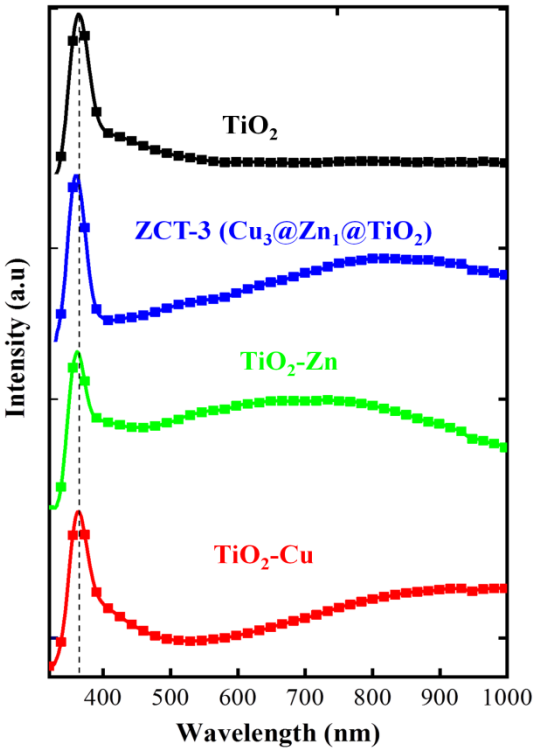

Fig. 3.2: DRS analysis of different Zn, Cu and Cu@Zn-TiO_2 nanocomposites.

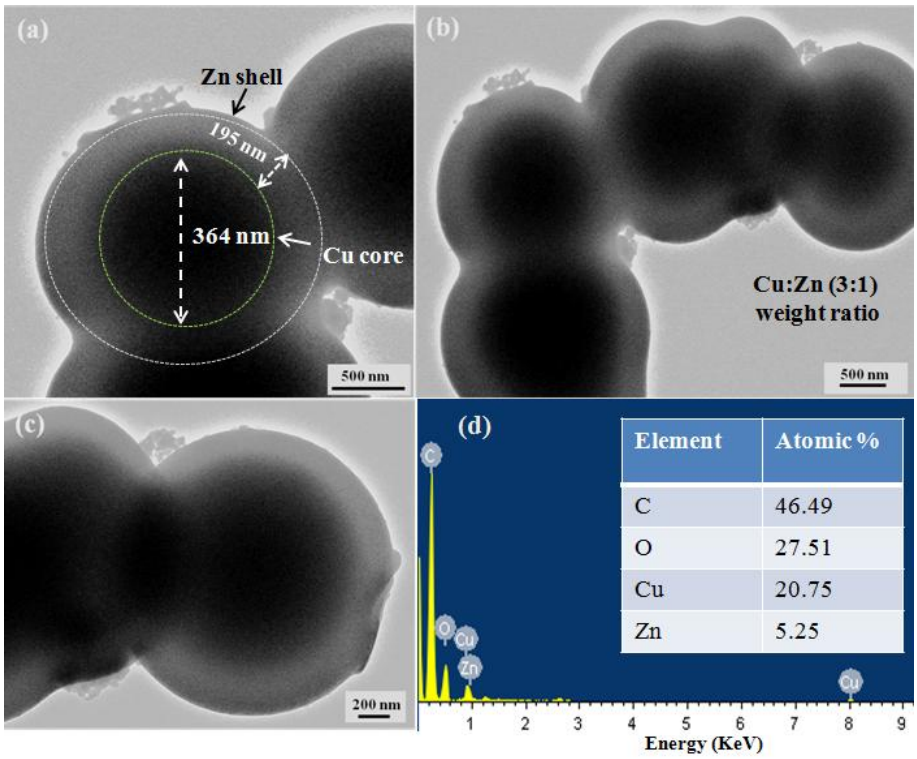

Fig. 3.3: (a-c) TEM images showing the formation of Cu@Zn (3:1) nanostructure (d) corresponding EDS analysis.

The galvanic interactions between zinc and copper nanoparticles lead to the formation of Cu@Zn NS. Since copper having higher reduction potential reduced first (act as a core) and zinc undergoes oxidation (as ZnO) and makes a shell over the reduced copper nanoparticles. However, as we move towards the core region, it shows higher intensity of Cu indicated by pink pattern in **Fig. 3.4 (e)** and possibly exists as Cu/Cu_2O. Thus, this result confirms the formation of Cu (core) and Zn (shell) in the observed core@shell nanostructure.

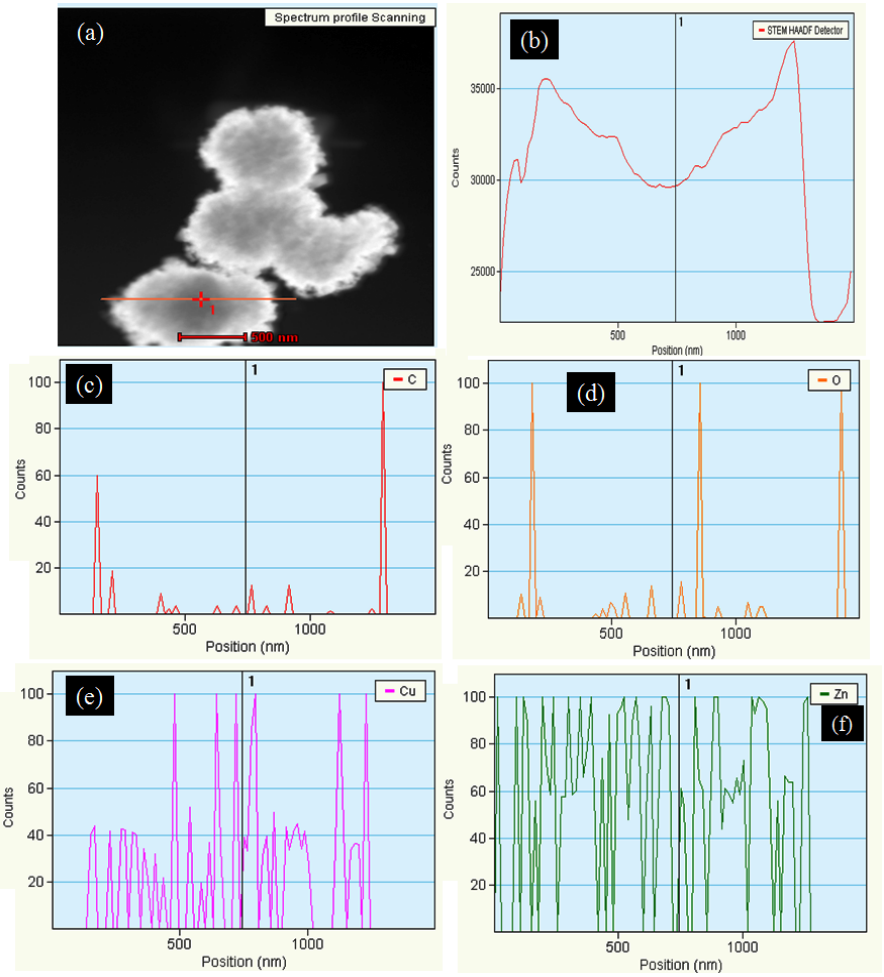

Fig. 3.4: STEM and line profile EDS mapping of Cu@Zn nanostructure.

Fig. 3.5 (a–b) represents the HRTEM analysis, showing the well-defined formation of (001) faceted TiO_2 nanosheets. The average dimensions of as-prepared TiO_2 nanosheets found to be 75× 60 nm. **Fig. 3.5 (c)** shows the lattice fringe pattern and the measured d values of 0.34 nm and 0.24 nm resembles with the (101) and (001) anatase phase of titanium dioxide respectively. Similarly, **Fig. 3.5 (d)** represents the SAED pattern of synthesized TiO_2 nanosheets demonstrating the formation of (101), (103), (004) and (112) distinct lattice planes. **Fig. 3.6** shows the HRTEM analysis of bimetallic ZCT-3 (Cu_3@Zn_1-TiO_2) impregnated on the surface of (001) faceted TiO_2 nanosheets.

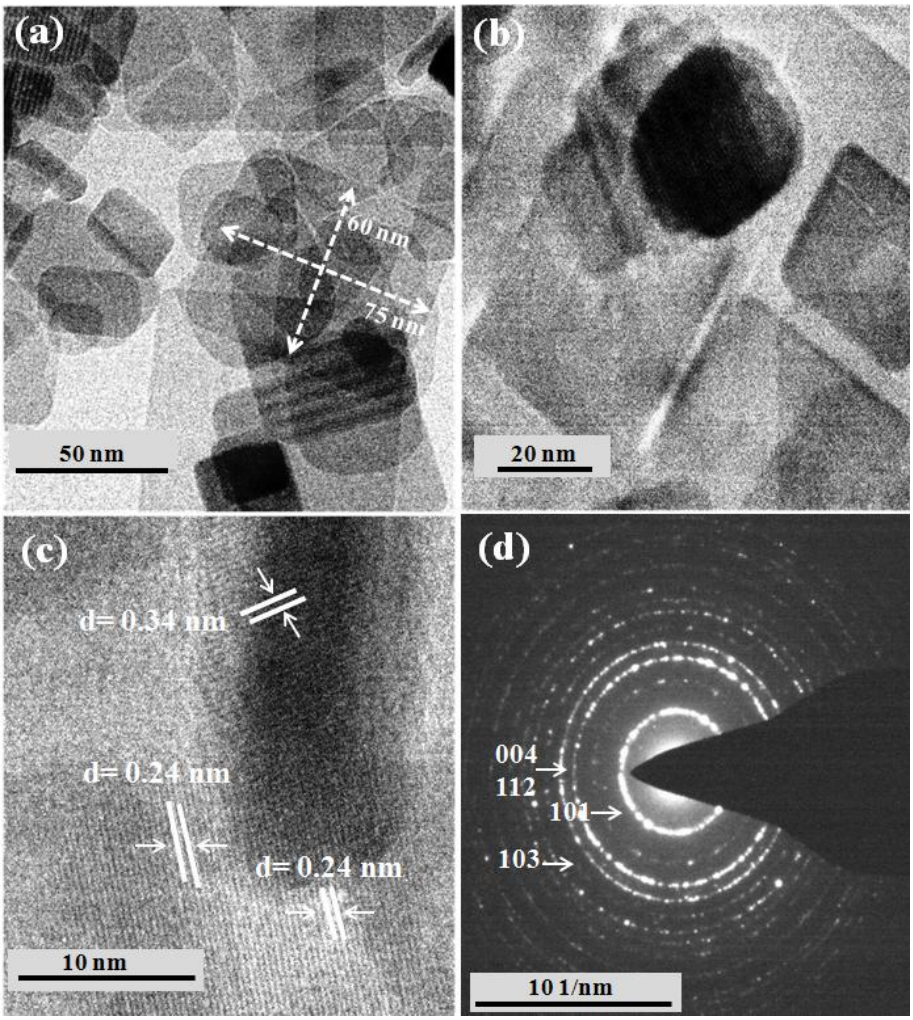

Fig. 3.5: (a-b) HRTEM images of TiO_2 nanosheets (c) lattice fringes and (d) SAED pattern.

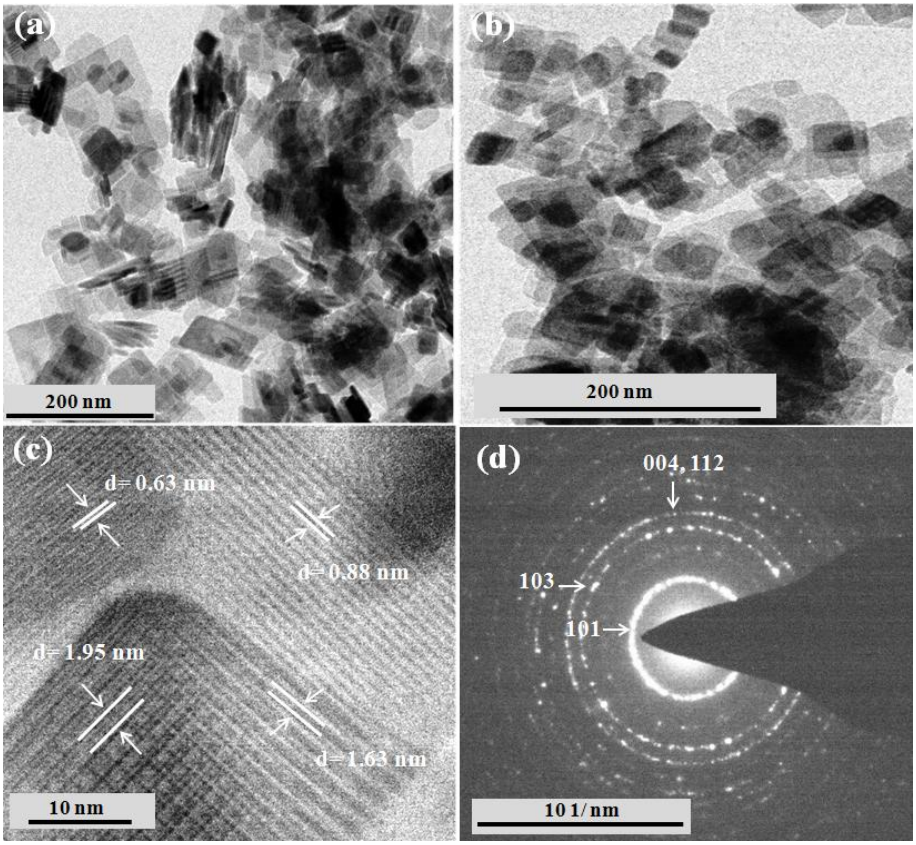

Fig. 3.6: (a-b) HRTEM images of ZCT-3 (Cu_3@Zn_1-TiO_2) nanocomposite (c) corresponding lattice fringes and (d) SAED pattern.

The elemental color dot mapping (**Fig. 3.7**) shows the presence of Ti, O, Cu, and Zn in ZCT-3 photocatalyst.

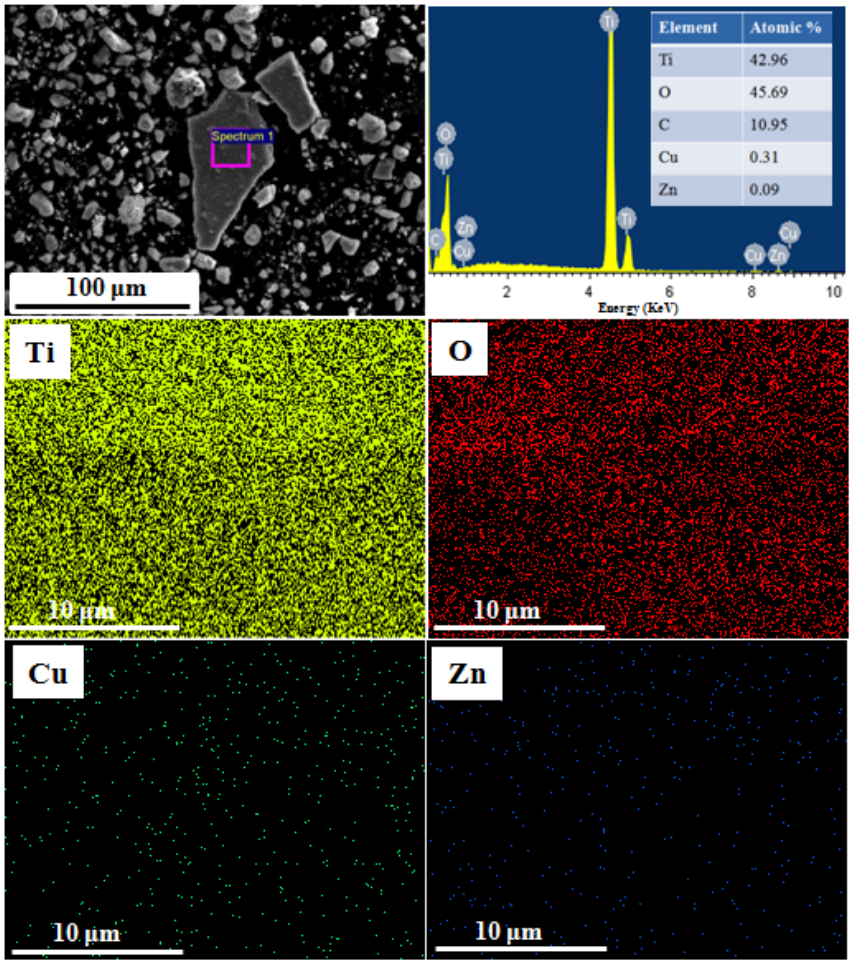

Fig. 3.7: Elemental dot mapping of different elements present in ZCT-3 catalyst.

Fig. 3.8 (a) represents the X-ray diffraction pattern of commercial available P25 and as-prepared TiO_2 nanosheets. The diffraction peaks of TiO_2 were matched with the anatase phase of titanium dioxide (JCPDS 01-089-4921). The most intensive diffraction peaks observed at 25.41°, 38.07°, 48.19°, 55.15°, and 60.27° were indexed to different (101), (004), (200), (105), and (204) lattice planes. The existence of (004) lattice plane at 38.07° clearly indicated the formation of exposed (001) faceted titania nanosheets (disappear in case of commercial P25). The absence of (001) diffraction peak might be due to some structural factor, arising due to tetragonal geometry of TiO_2. Similarly, **Fig. 3.8 (b)** represents the diffraction pattern after impregnation of bimetallic Cu@Zn on the surface of titanium dioxide nanosheets. The diffraction peaks of Cu@Zn (marked with dark circle) matches with intermetallic cubical structure (JCPDS No. 00-039-0400) which are indexed to different planes (311), (410), (511), and (630). It was observed that with increasing Cu weight ratio the growth and intensity of planes also increased in ZCT-2 and ZCT-3 respectively.

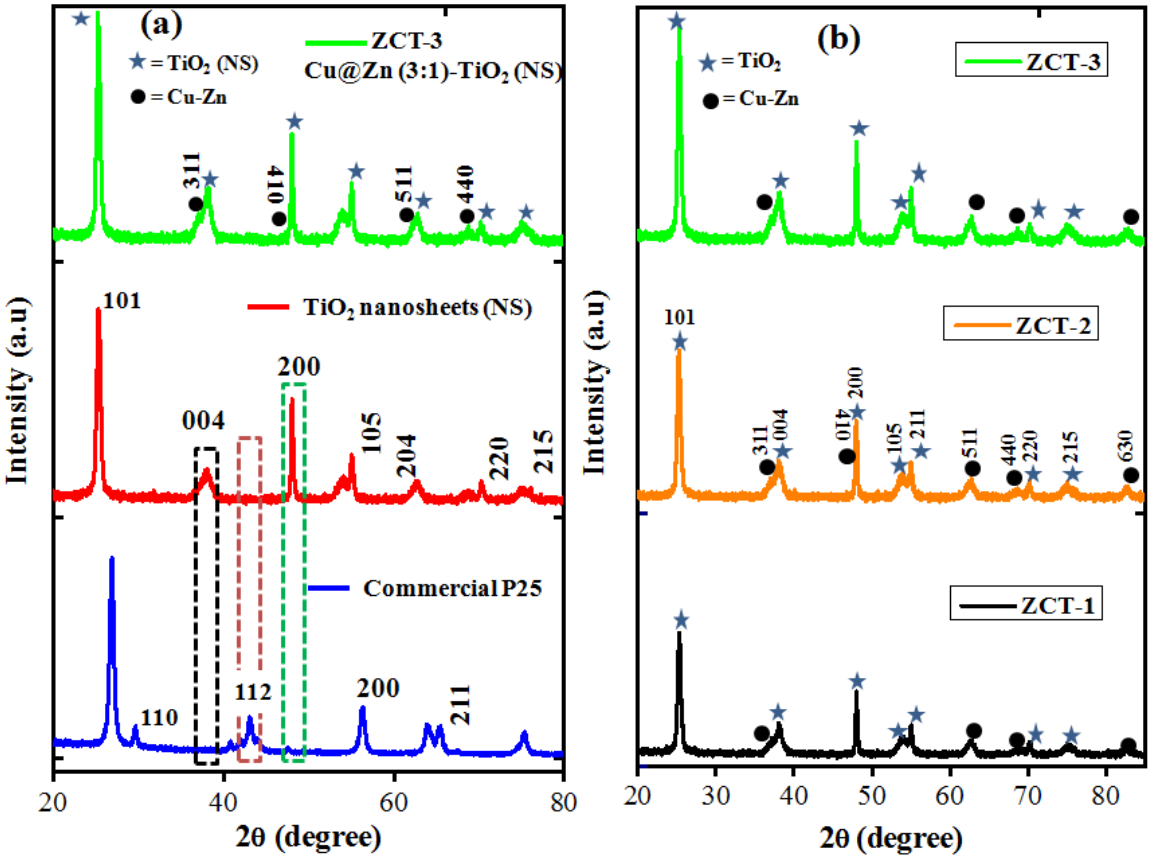

Fig. 3.8: XRD analysis of (a) commercial P25, TiO_2 nanosheets and Cu@Zn-TiO_2 nanocomposites (b) Cu@Zn-TiO_2 nanocomposites with varying Cu:Zn (1:1, 2:1, 3:1) weight ratio.

Fig. 3.9: represents the photoluminescence (PL) spectra of Zn/Cu-TiO_2 nanocomposites. The PL spectrum of TiO_2 nanosheets consists of several emission peaks at 384, 423, 485 and 530 nm corresponding to excitation at 320 nm. The intensive peaks at 423, 485 and 530 nm arise due to different surface defect states like O_2 vacancy, defect on the surface of TiO_2, and occurrence of $O_2^- \rightarrow Ti^{4+}$ electronic charge transfer [7, 51].

The impregnation of metal on the surface of TiO_2 prevents the recombination rate of charge carriers which results in the reduction of PL intensity. It was found that ZCT-1 nanocatalyst (Cu_1@Zn_1-TiO_2) exhibited a higher reduction

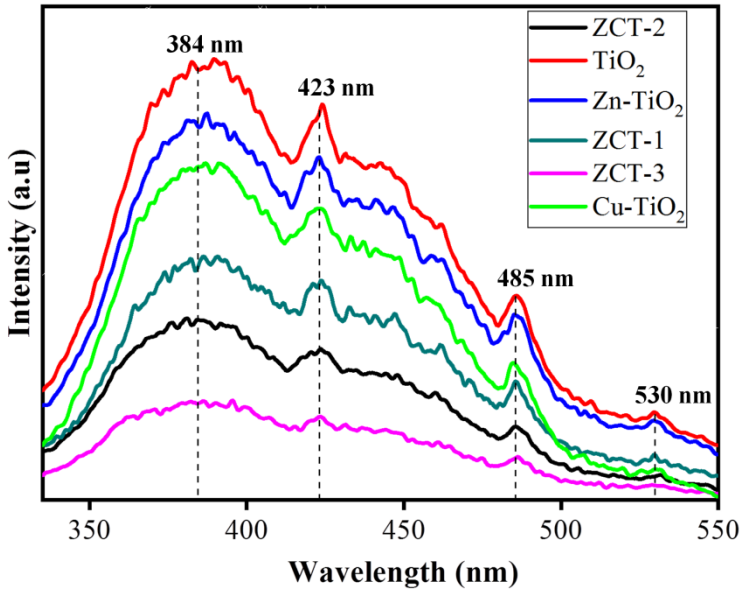

Fig. 3.9: PL (Photoluminescence) spectra of bare TiO_2 and Cu/Zn/Cu@Zn-TiO_2 nanocatalysts.

in PL intensity compared to Cu-TiO_2 and Zn-TiO_2 nanocomposites. It was also observed that with increasing Cu weight ratio, the PL intensity further decreased in case of ZCT-2 (Cu_2@Zn_1-TiO_2) and ZCT-3 (Cu_3@Zn_1-TiO_2) respectively. The higher quenching of PL intensity in case of bimetallic arises due to the reduction in barrier height which leads to effective charge transfer (e^--h^+) from the surface of TiO_2 nanosheets to bimetallic Cu@Zn nanostructure. **Fig. 3.10** (a) represents the BET surface analysis of titanium dioxide nanosheets and bimetallic ZCT-3 photocatalyst performed at cryogenic temperature. The deposition of Cu, Zn, and Cu@Zn nanocatalysts leads to some reduction in the surface area (**Table-3.1**). The surface area of ZCT-3 photocatalyst having higher Cu weight reduced to 59 m^2g^{-1} compared to ZCT-2 (62 m^2g^{-1}) and ZCT-1 (64 m^2g^{-1}) which may be arise due to little pore strain in the surface.

The surface area of bare TiO_2 nanosheets was found to be 73 m^2g^{-1} having a pore volume of 0.411 cm^3g^{-1}. The titania nanosheets were found to be multilayered and mesoporous in nature as indicated by N_2 adsorption or desorption isotherms which strictly follow Type IV Langmuir and H1 hysteresis loop. The BJH analysis also revealed that the majority of pore size distribution lies in the range of 2-10 nm showing the mesoporous behavior of the photocatalyst.

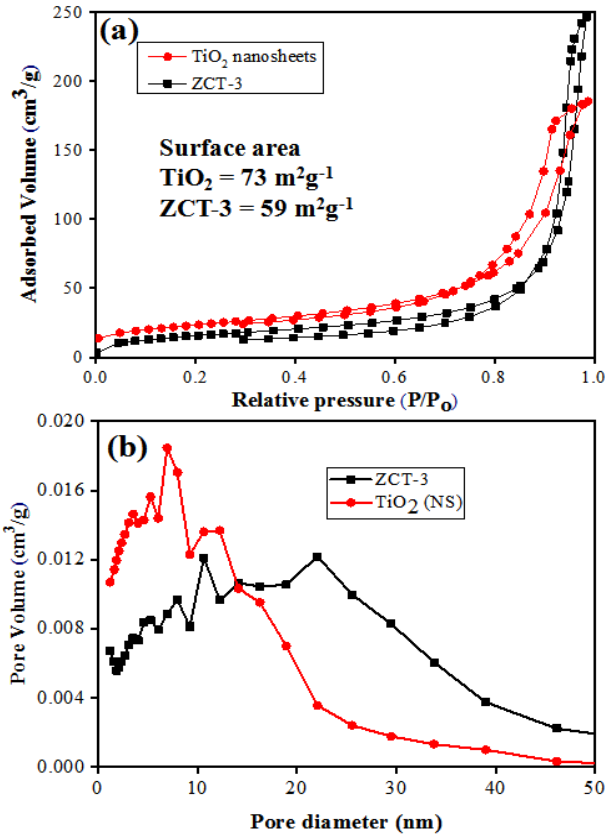

Fig. 3.10: BET surface analysis (a) N_2 adsorption-desorption isotherm (b) BJH analysis of TiO_2 and ZCT-3 nanocatalyst.

Table-3.1: The surface area, pore volume and pore diameter of different photocatalyst.

S.No.	Photocatalyst	Surface area (m^2g^{-1})	Total Pore Volume (cm^3g^{-1})	Mean Pore diameter (nm)
1	TiO_2	73	0.411	15.45
2	Zn-TiO_2	69	0.515	28.22
3	Cu-TiO_2	72	0.281	21.07
4	ZCT-1	64	0.359	22.19
5	ZCT-2	62	0.368	23.5
6	ZCT-3	59	0.381	25.9

Fig. 3.11 represents the XPS survey spectra showing the elemental peaks of Ti, O, Zn, and Cu present in ZCT-3 photocatalyst. The high resolution XPS spectrum of Ti 2p (**Fig. 3.12 (a)**) deconvoluted in two different peaks having center at 458.29 eV and 464.04 eV which are ascribed to $2p_{3/2}$ and $2p_{1/2}$ respectively. The difference in binding energy between two peaks was found to be 5.7 eV indicating the presence Ti^{4+} oxidation state [52]. **Fig. 3.12 (b)** shows the deconvoluted spectrum of O1s, fitted into three different peaks. Two peaks one at 529.1 eV and other at 529.3 eV were assigned to lattice or adsorbed oxygen species and oxygen atoms bound to Ti (Ti-O). The other peak at 530.5 corresponds to bonding between oxygen and Zn atoms (Zn-O) [53]. The Cu 2p XPS spectrum (**Fig. 3.12 (c)**) was fitted into two intensive peaks at 931.7 eV (corresponds to $2p_{3/2}$) and 951.5 eV (corresponds to $2p_{1/2}$) and one satellite peak at 952.7 eV. These peaks indicated that the Cu exist in two variable oxidation states 0 and +1 which are assigned to metallic copper or Cu_2O species [54, 55]. Similarly, the XPS spectrum of Zn 2p (**Fig. 3.12 (d)**) consists of two deconvoluted peaks having a center at 1020.7 eV and 1039.6 eV corresponding to $2p_{3/2}$ and $2p_{1/2}$ respectively. These peaks corroborate that zinc exists in +2 oxidation state in the form of ZnO which further confirm the galvanic interactions between Cu@Zn in which Cu reduced to 0 or +1 oxidation states and Zn in +2 oxidation state. In order to determine the thermal properties of as-prepared catalyst thermo gravimetrical analysis (**Fig. 3.13**) was carried out. The bare titanium oxide nanosheets showed a ~7.4 % mass loss within the temperature range of 25-225^{o} C which arises due to removal of water molecules adsorbed on the surface of TiO_2 nanosheets.

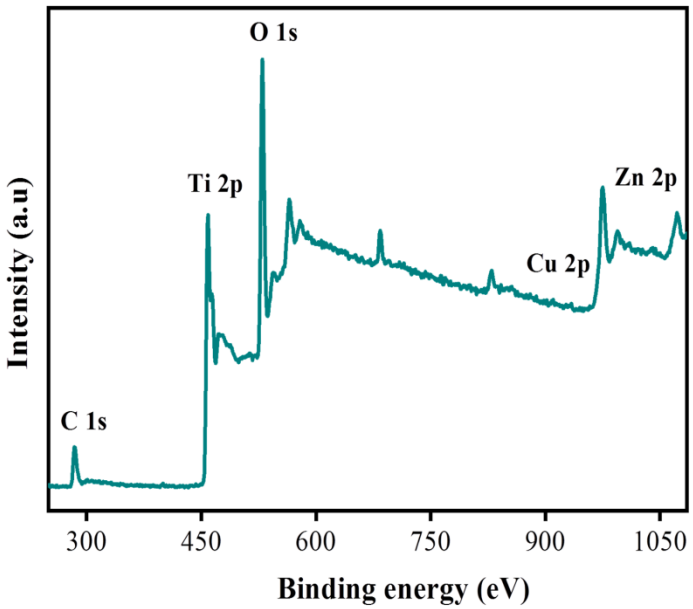

Fig. 3.11: XPS survey spectra of different elements present in ZCT-3 photocatalyst.

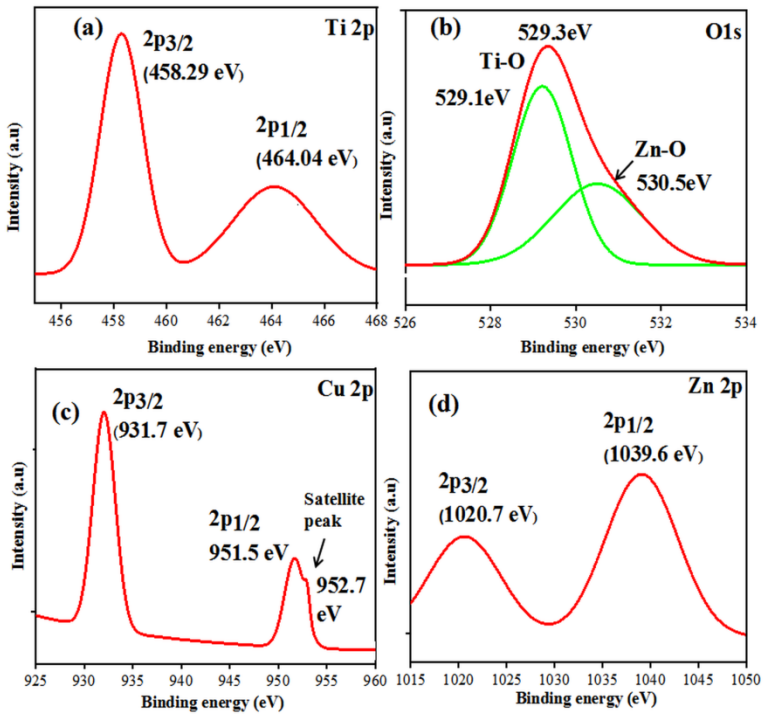

Fig. 3.12: XPS analysis of ZCT-3 (a) Ti 2p (b) O 1s (c) Cu 2p (d) Zn 2p.

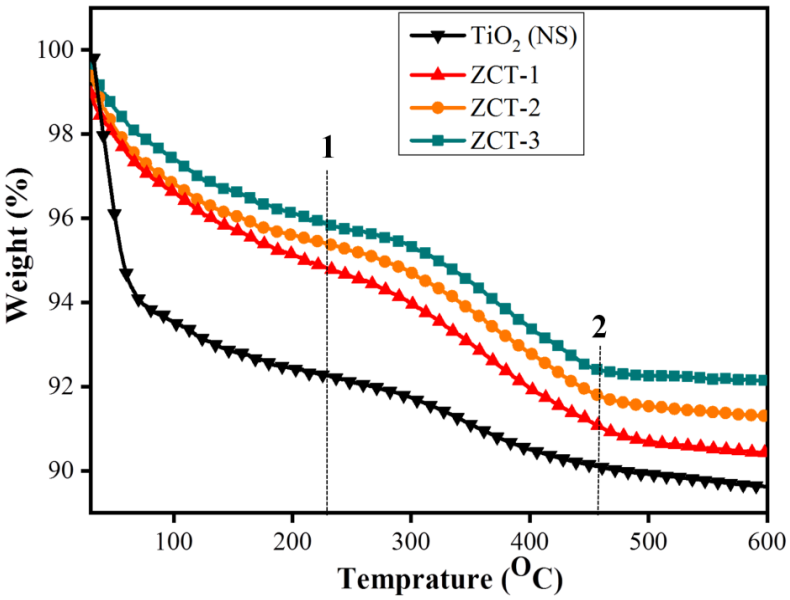

Fig. 3.13: TGA of TiO_2 and bimetallic-TiO_2 nanostructure.

The second mass loss of about ~2.37 % occurs in the temperature range of 230-450 ^{o}C ascribed to the breakdown of organic compounds inside the pores. The total percentage of mass loss occurred for TiO_2 nanosheets is ~9.77 % [56, 57]. It was observed that the deposition of Cu@Zn increases the thermal stability of the photocatalyst titanium dioxide (ZCT-1). Moreover, with an increasing weight ratio of Cu thermal stability further increased in the case of ZCT-2 and ZCT-3. The total percentage mass loss for ZCT-1, ZCT-2, and ZCT-3 found to be ~9.28 %, ~8.52 %, and ~7.62 % respectively.

Photocatalytic activity

The selective conversion of quinoline to 1,2,3,4-tetrahydroquinoline was analyzed by measuring the peak area and retention time with the standard (0.1mM) solutions. The samples were drawn periodically, to analyze the reaction products with GC-MS and GC-FID as shown in Fig. 3.14. The GC-FID peak of 1,2,3,4-tetrahydroquinoline with ZCT-3 observed at retention time (R_T) of 5.44 min and GC-MS peak observed at m/z = 133.1 (**Fig. 3.14**). **Fig. 3.15:** shows the % yield achieved during the hydrogenation of quinoline with bare TiO_2 and Zn/Cu-TiO_2 nanocomposites under visible light radiation, dark conditions, and saturated hydrogen atmosphere.

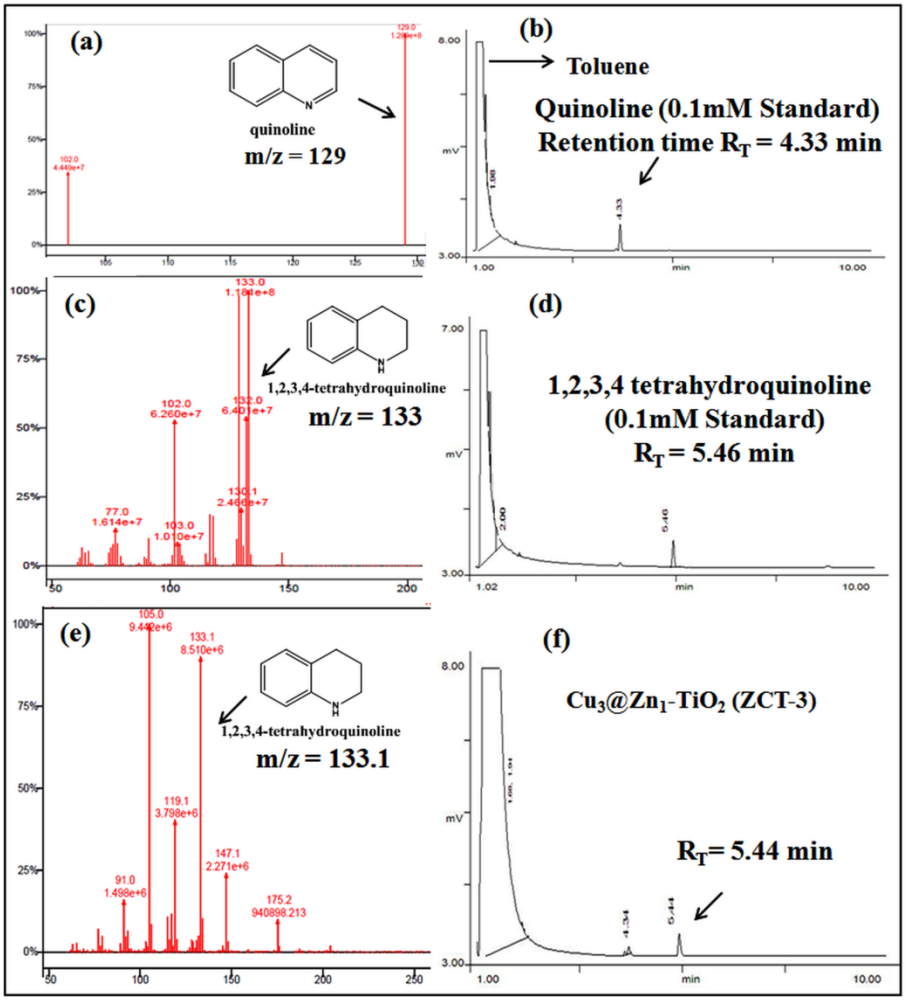

Fig. 3.14: GC-FID spectra with corresponding mass spectrum of (a,b) Standard quinoline (0.1 mM), (c,d) Standard 1,2,3,4-tertahydroquinoline (0.1 mM) and (e,f) 1,2,3,4-tertahydroquinoline formed during hydrogenation with ZCT-3 nanocatalyst.

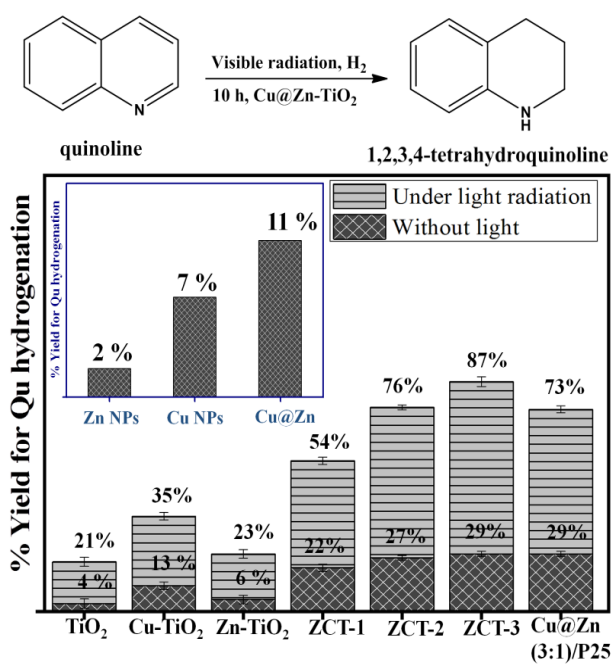

Fig. 3.15: The % yield obtained for quinoline hydrogenation under dark and visible radiation.

Table-3.2: Percentage yield and selectivity obtained for quinoline hydrogenation using different catalyst.

Sr. No.	Catalyst	Reaction time (h)	% Yield	% Selectivity
1	TiO_2	10	21	23
2	Cu-TiO_2	10	35	65
3	Zn-TiO_2	10	23	27
4	ZCT-1 (Cu_1@Zn_1-TiO_2)	10	54	>98
5	ZCT-2 (Cu_2@Zn_1-TiO_2)	10	76	>98
6	ZCT-3 (Cu_3@Zn_1-TiO_2)	10	87	>98

The Cu@Zn nanocatalyst (without TiO_2 support) exhibited higher percentage yield relative to their corresponding Cu and Zn nanoparticles (Inset, **Fig. 3.15**). The higher activity of bimetallic nanostructures credited to the synergistic interaction that occurs between these two galvanic metals. The Cu@Zn-TiO_2 nanocomposites exhibited higher conversion of quinoline in the dark that might be due to an increase in surface area with titanium dioxide support. But in the presence of light radiation and under hydrogenated atmosphere the ZCT-3 showed higher conversion and selectivity (**Table-3.2**) towards the quinoline hydrogenation (87%) compared to ZCT-2 (76%), ZCT-1 (54%) and monometallic counterparts. The photocatalytic hydrogenation of quinoline was also studied using Cu@Zn(3:1)/P25 under dark and visible light radiation. The % yield obtained for the quinoline hydrogenation was found to be 73% smaller as compared to ZCT-3 photocatalyst. The higher activity of ZCT-3 arise due to the fact that the (001) faceted TiO_2 surface exhibited higher catalytically exposed active sites and showed enhanced photoactivity compared to thermodynamically stable (101) faceted TiO_2 nanoparticles.

The deposition of different metals on the surface of TiO_2 (001) further enhanced the photocatalytic efficiency of TiO_2. However, under dark condition, both catalysts showed almost similar catalytic activity. In order to

determine whether the catalytic efficiency of ZCT-3 enhanced due to increase in Cu weight ratio or arise due to the synergistic effect of Cu@Zn impregnated on the surface of titanium dioxide nanosheets. The hydrogenation reaction was further analyzed using TiO_2 nanosheets doped with 2 % and 3 % of Cu nanoparticles and also with ZCT-4 phtocatalyst (having (4:1) Cu:Zn weight ratio). It was observed that the percentage yield for quinoline hydrogenation was found be similar for both the catalysts as shown in **Fig. 3.16 (a)**. However, the % yield obtained (**Fig. 3.16 (a)**) using ZCT-4 was found to be higher than ZCT-1, ZCT-2, but smaller than ZCT-3 photocatalyst. Thus, ZCT-3 catalyst was found to more effective and selective towards the quinoline hydrogenation. The kinetic measurement for the reaction was examined by using the Langmuir-Hinshelwood kinetic equation.

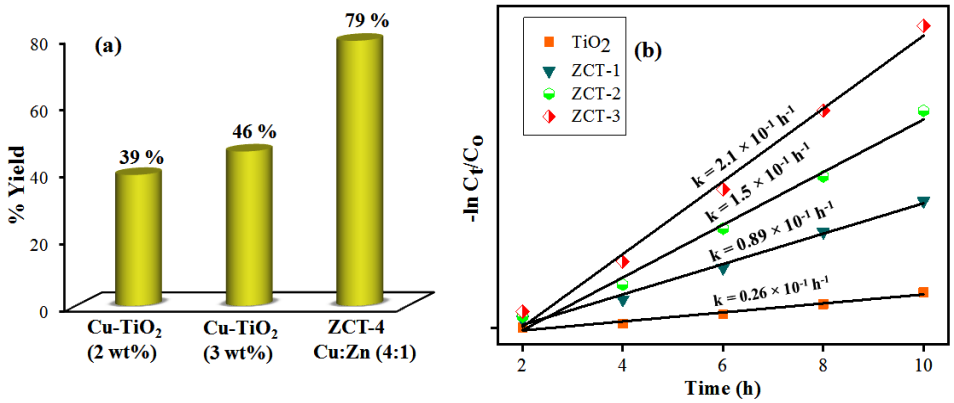

Fig. 3.16: (a) Histogram showing the percentage yield for the hydrogenation of quinoline (b) rate constant obtained under visible radiation.

It was found that selective hydrogenation of quinoline pursues the pseudo-first-order of kinetics. The photocatalyst ZCT-3 (**Fig. 3.16 (b)**) exhibited higher rate constant of k = 2.1 × 10^{-1} h^{-1} compared to Cu-TiO_2 (k = 0.46 × 10^{-1} h^{-1}) and Zn-TiO_2 (k = 0.28 × 10^{-1} h^{-1}) nanocomposites.

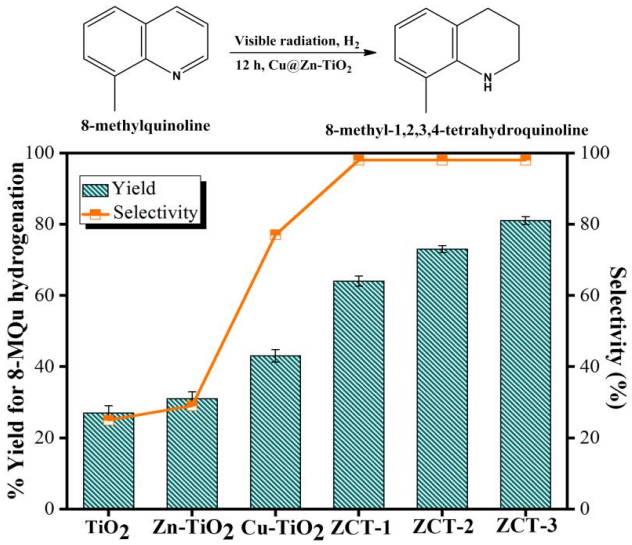

Fig. 3.17: The % yield and selectivity obtained for 8-methyl quinoline using different nanocatalysts.

The catalytic efficiency of bimetallic Cu@Zn-TiO_2 photocatalyst was further investigated using 8-methyl quinoline (8-MQu), and 8-hydroxyquinoline (8-HQu). It was observed that bimetallic ZCT-3 nanocatalyst showed the higher conversion of both 8-MQu and 8-HQu relative to bare TiO_2 and Zn/Cu-TiO_2 nanocomposites. **Fig. 3.17** represents the percentage yield and selectivity acquired by

different catalysts during the hydrogenation of 8-MQu. It was observed that ZCT-3 exhibited higher percentage yield of 81 % followed by ZCT-2 > ZCT-1 > Cu-TiO_2 > Zn-TiO_2 and bare TiO_2. Similarly, **Fig. 3.18** shows the percentage yield for the hydrogenation of 8-HQu using different photocatalysts. Similar trend ZCT-3 > ZCT-2 > ZCT-1 was observed during the hydrogenation of 8-HQu.

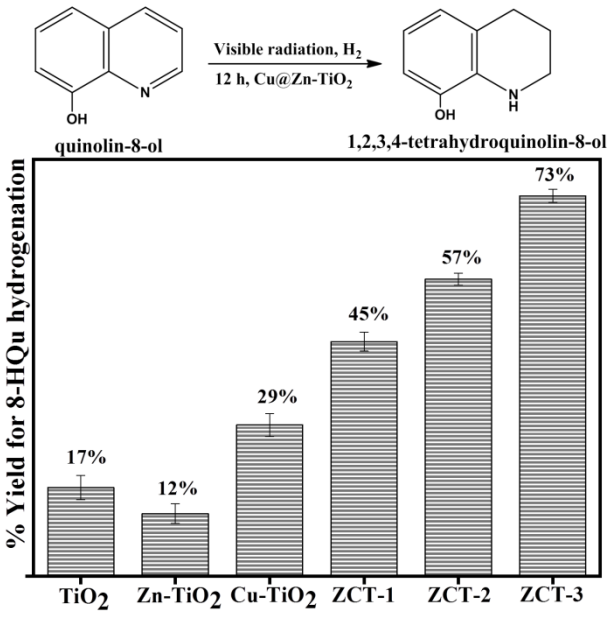

Fig. 3.18: Percentage yield obtained for hydrogenation of 8-hydroxyquinoline.

The mechanism for selective quinoline hydrogenation

When the as-prepared photocatalyst was illuminated with visible radiation the electrons were excited from valance band to corresponding conduction band of TiO_2. The hetero-junction formed after the deposition of bimetallic Cu@Zn on the surface TiO_2 promoted the electron transfer and increased the electron density over the reaction active center of Cu@Zn. Since the hydrogenation of quinoline leads to the formation of 1,2,3,4-tetrahydroquinoline, it suggested that the hydrogenation reaction occurs via effective adsorption of N-heteroarenes and hydrogen on the surface of bimetallic-TiO_2 nanocomposites. The suggested mechanism for quinoline hydrogenation is shown in **Scheme-3.2.**

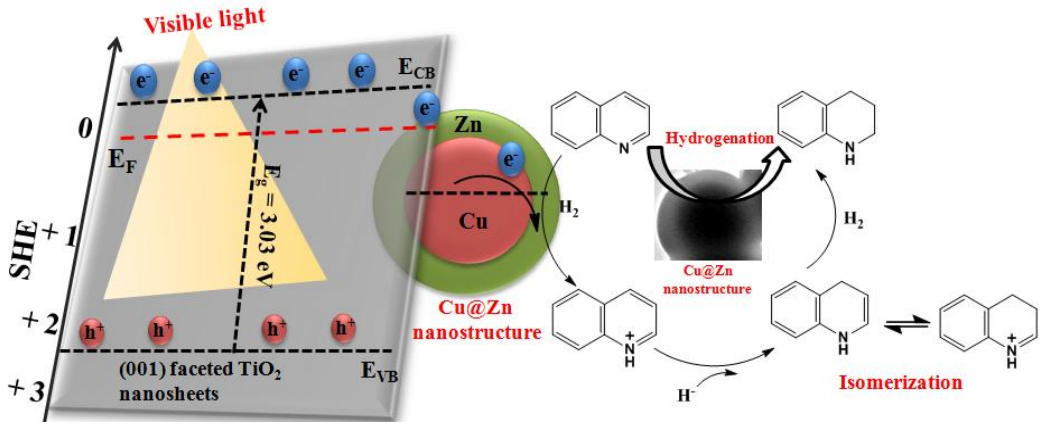

Scheme-3.2: The possible mechanism for the quinoline hydrogenation.

During reaction process, quinolin-1-ium cation was formed first via 1,4 hydride addition (**Scheme-3.2**) which further undergoes 1,2 hydride addition which leads to the formation of 3,4-dihydroquinolin-1-ium cation or 1,4-dihydroquinoline and finally was converted into desired hydrogenated product (1,2,3,4-tetrahydroquinoline). The synergistic interaction between the two metals at bimetallic-TiO_2 interface resulted in the reduction of barrier height which effectively promotes electron and hydride ion (H^-) transfer for quinoline hydrogenation compared to Cu/Zn-TiO_2 nanocomposites.

The reusability over the number of cycles is an important property for the metal supported heterogeneous catalysts. The reusability of catalyst for quinoline hydrogenation is a major concern as catalyst becomes inactive due to interaction of nitrogen atoms and hydrogenated product with metal nanoparticles. The bimetallic ZCT-3 photocatalyst (**Fig. 3.19**) was examined for the reusability test under visible light and saturated hydrogenated atmosphere for five successive cycles. The ZCT-3 photocatalyst showed stable catalytic performance and no significant loss in catalytic activity was observed after five consecutive cycles. The slight loss in catalytic activity arises due to the fact that a few amount of catalyst was drawn during its cleaning process.

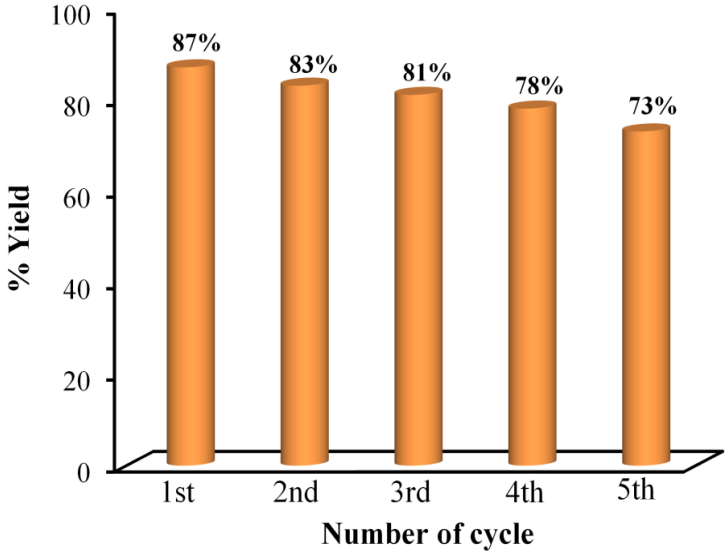

Fig. 3.19: Reusability test of ZCT-3 photocatalyst for quinoline hydrogenation.

References

[1] K. Shim, W.-C. Lee, M.-S. Park, M. Shahabuddin, Y. Yamauchi, M.S.A. Hossain, Y.-B. Shim, J.H. Kim, Sens. Actuators, B, 278 (2019) 88-96.

[2] T.D. Thanh, N.D. Chuong, H.V. Hien, N.H. Kim, J.H. Lee, ACS Appl. Mater. Interfaces, 10 (2018) 4672-4681.

[3] H. Xu, P. Song, J. Wang, Y. Shiraishi, Y. Du, Q. Liu, ACS Sustainable Chem. Eng., 6 (2018) 7159-7167.

[4] B. Li, J. Liu, Q. Liu, R. Chen, H. Zhang, J. Yu, D. Song, J. Li, M. Zhang, J. Wang, Appl. Surf. Sci., (2019).

[5] N. Roy, N. Suzuki, Y. Nakabayashi, Y. Hirano, H. Ikari, K.i. Katsumata, K. Nakata, A. Fujishima, C. Terashima, ChemElectroChem., 5 (2018) 2542-2550.

[6] W. Dong, Y. Ren, Z. Bai, J. Jiao, Y. Chen, B. Han, Q. Chen, J. Colloid Interface Sci., 512 (2018) 812-818.

[7] A. Bathla, B. Pal, J. Ind. Eng. Chem., 67 (2018) 486-496.

[8] Y. Ma, W. Li, E.C. Cho, Z. Li, T. Yu, J. Zeng, Z. Xie, Y. Xia, ACS Nano, 4 (2010) 6725-6734.

[9] W.-L. Weng, C.-Y. Hsu, J.-S. Lee, H.-H. Fan, C.-N. Liao, Nanoscale, 10 (2018) 9862-9866.

[10] P. Ma, D. Gao, Y. Ni, L. Gao, Plasmonics, 11 (2016) 183-187.

[11] H.T. Nasrabadi, E. Abbasi, S. Davaran, M. Kouhi, A. Akbarzadeh, Artif. Cells Nanomed. Biotechnol., 44 (2016) 376-380.

[12] X. Jin, A. Mao, M. Ding, P. Ding, T. Zhang, X. Gu, W. Xiao, J. Yuan, Appl. Spectrosc., 70 (2016) 1692-1699.

[13] M.B. Gawande, A. Goswami, T. Asefa, H. Guo, A.V. Biradar, D.-L. Peng, R. Zboril, R.S. Varma, Chem. Soc. Rev., 44 (2015) 7540-7590.

[14] M. Khatami, H. Alijani, M. Nejad, R. Varma, Appl. Sci., 8 (2018) 411.

[15] K.D. Gilroy, A. Ruditskiy, H.-C. Peng, D. Qin, Y. Xia, Chem. Rev., 116 (2016) 10414-10472.

[16] S. De, J. Zhang, R. Luque, N. Yan, Energy Environ. Sci., 9 (2016) 3314-3347.

[17] H.-L. Jiang, T. Akita, T. Ishida, M. Haruta, Q. Xu, J. Am. Chem. Soc., 133 (2011) 1304-1306.

[18] C. Xu, Y. Liu, J. Wang, H. Geng, H. Qiu, ACS Appl. Mater. Interfaces, 3 (2011) 4626-4632.

[19] A. Sarkar, A. Manthiram, J. Phy. Chem., C, 114 (2010) 4725-4732.

[20] G.E. Dobereiner, A. Nova, N.D. Schley, N. Hazari, S.J. Miller, O. Eisenstein, R.H. Crabtree, J. Am. Chem. Soc., 133 (2011) 7547-7562.

[21] V. Sridharan, P.A. Suryavanshi, J.C. Menéndez, Chem. Rev., 111 (2011) 7157-7259.

[22] C. Wang, C. Li, X. Wu, A. Pettman, J. Xiao, Angewandte Chemie., 121 (2009) 6646-6650.

[23] S. Chakraborty, W.W. Brennessel, W.D. Jones, J J. Am. Chem. Soc., 136 (2014) 8564-8567.
[24] F. Chen, A.-E. Surkus, L. He, M.-M. Pohl, J.r. Radnik, C. Topf, K. Junge, M. Beller, J. Am. Chem. Soc., 137 (2015) 11718-11724.
[25] L. Zhang, X. Wang, Y. Xue, X. Zeng, H. Chen, R. Li, S. Wang, Catal. Sci. Technol., 4 (2014) 1939-1948.
[26] J. Wu, J.H. Barnard, Y. Zhang, D. Talwar, C.M. Robertson, J. Xiao, Chem. Commun., 49 (2013) 7052-7054.
[27] B. Abarca, R. Adam, R. Ballesteros, Org. Biomol. Chem., 10 (2012) 1826-1833.
[28] A. Bathla, B. Pal, ChemistrySelect, 3 (2018) 4738-4744.
[29] S. Li, Y. Yang, Y. Wang, H. Liu, J. Tai, J. Zhang, B. Han, Catal. Sci. Technol., 8 (2018) 4314-4317.
[30] Y. Gong, P. Zhang, X. Xu, Y. Li, H. Li, Y. Wang, J. Catal., 297 (2013) 272-280.
[31] Y. Chen, Z. Yu, Z. Chen, R. Shen, Y. Wang, X. Cao, Q. Peng, Y. Li, Nano Research, 9 (2016) 2632-2640.
[32] S. Zhang, Z. Xia, T. Ni, H. Zhang, C. Wu, Y. Qu, J. Mater. Chem., A, 5 (2017) 3260-3266.
[33] I. Sorribes, L. Liu, A. Doménech-Carbó, A. Corma, ACS Catal., 8 (2018) 4545-4557.
[34] A. Monga, A. Bathla, B. Pal, Sol. Energy, 155 (2017) 1403-1410.
[35] A. Monga, R.A. Rather, B. Pal, Sol. Energy Mater. Sol. Cells, 172 (2017) 285-292.
[36] S.-H. Chang, P.-Y. Yang, C.-M. Lai, S.-C. Lu, G.-A. Li, W.-C. Chang, H.-Y. Tuan, CrystEngComm., 18 (2016) 616-621.
[37] S. Kamimura, S. Yamashita, S. Abe, T. Tsubota, T. Ohno, Appl. Catal., B, 211 (2017) 11-17.
[38] Z. Lyu, B. Liu, R. Wang, L. Tian, J. Mater. Res., 32 (2017) 2781-2789.
[39] S. Ma, S. Zhan, Y. Jia, Q. Zhou, ACS Appl. Mater. Interfaces, 7 (2015) 21875-21883.
[40] V. Vaiano, M. Lara, G. Iervolino, M. Matarangolo, J. Navio, M. Hidalgo, J. Photochem. Photobiol., A, 365 (2018) 52-59.
[41] C. Xie, J. Song, H. Wu, Y. Hu, H. Liu, Z. Zhang, P. Zhang, B. Chen, B. Han, J. Am. Chem. Soc., (2019).
[42] Z. Tong, D. Yang, T. Xiao, Y. Tian, Z. Jiang, Chem. Eng. J., 260 (2015) 117-125.

[43] H. She, H. Zhou, L. Li, Z. Zhao, M. Jiang, J. Huang, L. Wang, Q. Wang, ACS Sustain. Chem. Eng., 7 (2018) 650-659.

[44] H. She, H. Zhou, L. Li, L. Wang, J. Huang, Q. Wang, ACS Sustain. Chem. Eng., 6 (2018) 11939-11948.

[45] Q. Ma, X. Peng, M. Zhu, X. Wang, Y. Wang, H. Wang, Electrochem. Commun., 95 (2018) 28-32.

[46] X. Peng, C. He, Q. Liu, X. Wang, H. Wang, Y. Zhang, Q. Ma, K. Zhang, Y. Han, H. Wang, Electrochim. Acta, 222 (2016) 1112-1119.

[47] C. He, X. Peng, Q. Liu, X. Fan, H. Wang, Int. J. Hydrog Energy, 39 (2014) 13415-13420.

[48] W.-S. Wang, D.-H. Wang, W.-G. Qu, L.-Q. Lu, A.-W. Xu, J. Phys. Chem. C, 116 (2012) 19893-19901.

[49] R.A. Rather, D. Pooja, P. Kumar, S. Singh, B. Pal, J. Cleaner Prod., 175 (2018) 394-401.

[50] X. Han, Q. Kuang, M. Jin, Z. Xie, L. Zheng, J. Am. Chem. Soc., 131 (2009) 3152-3153.

[51] D.K. Pallotti, L. Passoni, P. Maddalena, F. Di Fonzo, S. Lettieri, J. Phys. Chem. C, 121 (2017) 9011-9021.

[52] N. Chen, D. Deng, Y. Li, X. Liu, X. Xing, X. Xiao, Y. Wang, Sci. Rep., 7 (2017) 7692.

[53] R.R. Thankalekshmi, A. Rastogi, in Hybrid bulk heterojunction solar cells with vertically aligned ZnO/ZnO_{1-xsx} nanorods in core-shell like nanostructure, pp. 1-6, IEEE, (2015).

[54] H. Hou, M. Shang, F. Gao, L. Wang, Q. Liu, J. Zheng, Z. Yang, W. Yang, ACS Appl. Mater. Interfaces, 8 (2016) 20128-20137.

[55] M.-Y. Lee, S.-J. Ding, C.-C. Wu, J. Peng, C.-T. Jiang, C.-C. Chou, Sens. Actuators, B 206 (2015) 584-591.

[56] K.V. Bineesh, D.-K. Kim, D.-W. Park, Nanoscale, 2 (2010) 1222-1228.

[57] M.M. Ba-Abbad, A.A.H. Kadhum, A.B. Mohamad, M.S. Takriff, K. Sopian, Int. J. Electrochem. Sci, 7 (2012) 4871-4888.

CHAPTER- 4

Photocatalytic vs. catalytic hydrogenation of industrially important unsaturated aldehydes using Pd(core)@Au(shell)/TiO_2 nanostructure

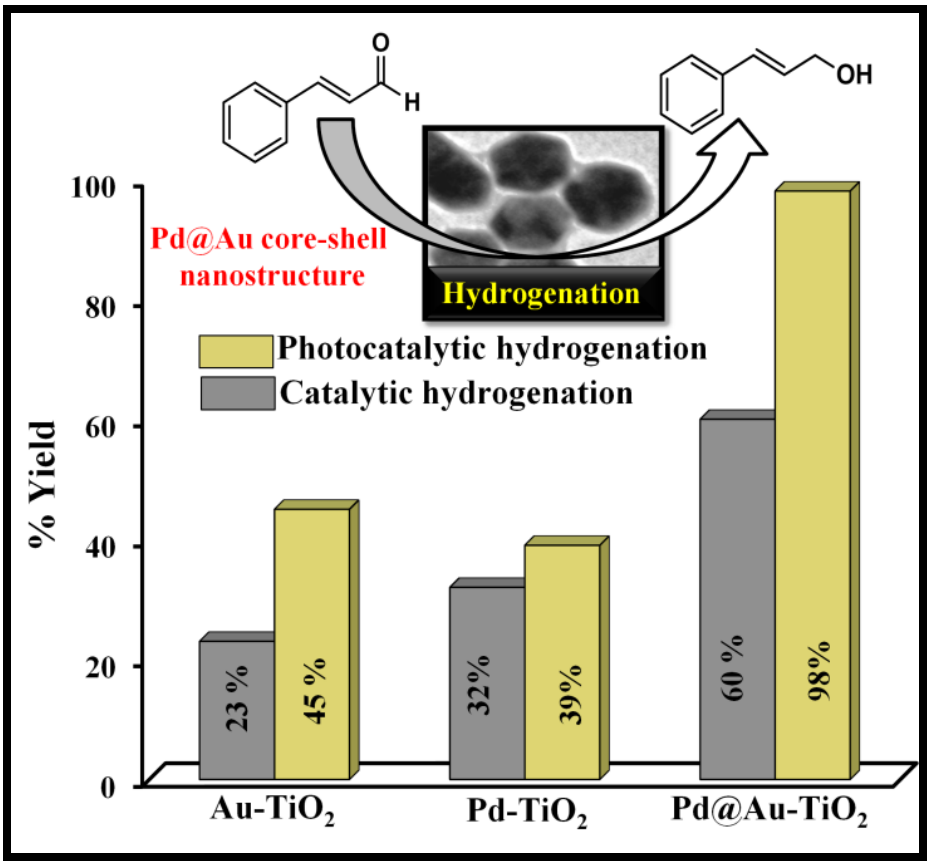

Schematic outline

This research work displayed the preparation, characterization and catalytic/photocatalytic activity of bimetallic Pd@Au core-shell nanostructure supported TiO_2 nanospheres. It was found that under sunlight radiation, bimetallic Pd@Au/TiO_2 photocatalyst exhibited higher percentage yield (98 %) and selectivity (100 %) for hydrogenation of cinnamaldehyde and croton aldehyde relative to their monometallic analogues.

4.1 Introduction

Bimetallic nanostructure of galvanic metals (Cu, Zn, Au, Pd, Ni, etc.) with different morphological appearance frequently show superior catalytic/photocatalytic activities compared to their monometallic analogues [1-6]. The tremendous performance of these bimetallic nanoparticles credited to their diverse arrangement/combination and synergistic interaction between two different metal atoms. Among different forms of bimetallic nanoparticles, core@shell nano-arrangement constructed via co-reduction method (based on galvanic interaction) found numerous applications in different research fields like catalysis, photocatalysis, sensing, and drug delivery [7-13]. The electrochemical potential difference between the two metals plays a crucial role in galvanic replacement reaction and also in finalizing the structural design [14, 15]. Wu *et al.* [16] reported the synthesis of bimetallic Cu@Pt nanostructure by galvanic replacement reaction and observed that Cu@Pt display superior performance for oxygen reduction reaction relative to monometallic counterparts. Bathla *et al.* [17] reported the formation of $Cu@Zn/TiO_2$ core-shell nanostructure via galvanic interaction method for the selective quinoline hydrogenation under visible light irradiation. Similarly, Yang *et al.* demonstrated the formation of Ag@Au core-shell nanocubes via galvanic replacement reaction between $AgNO_3$ and $HAuCl_4$ and studied for its enhanced SERS activity [18].

The selective hydrogenation of α-β unsaturated aldehydes to their corresponding alcohols is of great interest from the scientific and industrial point of view. The hydrogenated product of cinnamaldehyde (CAL) i.e. cinnamyl alcohol (COL) is an essential component for the synthesis of fine chemicals, perfumes, and cosmetics [19-22]. The selective hydrogenation of CAL to COL is a challenging task as it involves both C=C and C=O bonds. From the previous studies [23-25], it was observed that the hydrogenation occurs more preferably over the olefinic group than the carbonyl group. Different strategies have been employed by the researchers to fabricate the catalytic system that can effectively and selectively hydrogenate the carbonyl group. Cattaneo *et al.* [26] reported the catalytic hydrogenation of cinnamaldehyde using the bimetallic Au-Pd catalyst. Pal *et al.* [27] reported the catalytic hydrogenation of cinnamaldehyde and crotonaldehyde using different size PVP capped nickel nanoparticles. Yuan *et al.* [28] reported the hydrogenation of cinnamaldehyde using magnetic CoPt bimetallic nanoparticles. Similarly,

Szumełda *et al.* [29] reported the hydrogenation of cinnamaldehyde using bimetallic Pd/Ir nanoparticles under a hydrogen atmosphere and high temperature.

The conventional hydrogenation of unsaturated aldehydes is usually carried out under very harsh environment. It involves the use of H_2 under high-pressure, high temperature and also involves the use of different metal hydrides [24, 30-32] i.e. $NaBH_4$, $LiAlH_4$. In order to avoid the use of these explosives, high-cost, and tedious reaction conditions, the metal-catalyzed hydrogen transfer under light radiation is a promising alternative technique for the selective hydrogenation reactions [33-36]. Nowadays, there is significant research attention towards the photocatalytic hydrogen transfer using metal/bimetal doped semiconductor. The metal impregnated on the surface of the semiconductor acts as co-catalyst and improves its photocatalytic efficiency for different activities. Titanium dioxide (TiO_2) is an effective, non-toxic, highly stable, promising semiconductor material and found various applications in different research fields [37-40]. The major drawback regarding titanium dioxide is a wide energy band gap which limits its photocatalytic activity under visible light radiation. Efforts have been made to fabricate the complex M-TiO_2 catalytic system containing different plasmonic metals (Cu, Au, etc.) that effectively activate and improve the photocatalytic activity of TiO_2 under visible light irradiation. Monga *et al.* [41] reported the formation of core-shell and inverse core-shell of Cu and Au deposited on TiO_2 for photocatalytic reduction of nitro-aromatics under visible light radiation. Crake *et al.* [42] reported the gas phase photoreduction of CO_2 using TiO_2/C_3N_4 nanocomposite under UV-Visible light radiation. Similarly, Rather *et al.* [43] reported the sunlight driven photocatalytic hydrogen evolution from water using Au-Pt loaded TiO_2 nanosheets.

In this respect, the present study represents the formation of bimetallic core@shell nanostructure of gold and palladium synthesized via the co-reduction method. The galvanic replacement reaction between Pd and Au results in the formation of Pd@Au core@shell nanostructure. The prepared Pd@Au nanocatalysts were aimed to study the selective hydrogenation of cinnamaldehyde and crotonaldehyde under both catalytic and photocatalytic conditions. The bimetallic Pd@Au nanostructure displayed superior activity and selectivity for catalytic hydrogenation of cinnamaldehyde than corresponding monometallic counterparts. On the other hand, when Pd@Au used as co-catalyst after deposition on the surface of as-prepared TiO_2 nanosphere (NS), the resultant Pd@Au-TiO_2 showed superior improvement in the yield and

selectivity for cinnamaldehyde under solar radiation. Therefore, this study reveals that photocatalytic hydrogenation of unsaturated carbonyls using plasmonic Pd@Au-TiO_2 hetero-junction could be a promising and greener approach in comparison to the traditionally used harsh catalytic conditions.

4.2 Experimental details

4.2.1 Materials

$PdCl_2$ (Palladium Chloride), $HAuCl_4$ (Chloroauric acid), and PVP (Polyvinylpyrrolidone) were acquired from Sigma Aldrich India. Cinnamaldehyde (CAL-C_9H_8O), Crotonaldehyde (COAL-C_4H_6O), Cinnamyl alcohol ($C_9H_{10}O$), Ascorbic acid ($C_6H_8O_6$), Isopropyl alcohol (IPA), KBr (Potassium bromide) were purchased from Spectrochem, India and titanium dioxide (P25) from Degussa. All these chemicals were used as they received without any further modification.

4.2.2 Synthesis of Pd@Au core-shell nanostructure

The core-shell nanostructures of Pd-Au were synthesized via the co-reduction method which involves the galvanic replacement reaction between two different metal atoms. In the typical procedure, 8.5 ml aqueous solution of $PdCl_2$ (2 mM) was transferred into 50 ml round bottom flask. To this 10 ml aqueous solution containing ascorbic acid (100 mg), 66.6 mg of PVP, 60 mg of KBr was added. The resulting mixture was preheated at 110 ^oC for 1 hour under continuous magnetic stirring. 3 ml aqueous solution of $HAuCl_4$ (3 mM) was added into preheated solution. After the introduction of $HAuCl_4$ in the reaction mixture, reaction temperature was ramped to 200 ^oC and was kept at 200 ^oC for another 1h using refluxing method (**Scheme-4.1**).

A similar procedure was followed to fabricate the monometallic Pd and Au nanoparticles. The formation of nanoparticles was predicted from the variation in the color of the reaction mixture. In the case of Pd nanoparticles, the solution color changes from dark yellow to black suggesting the formation of Pd nanoparticles and the color changes from light yellow to pink for Au nanoparticles. The final product was centrifuged, washed and re-dispersed in a known amount of DI water.

4.2.3 Synthesis of TiO_2 nanosphere (NS)

The nanospheres of titanium dioxide were synthesized using a hydrothermal approach. 2g of commercial available P25 was added to the aqueous solution of NaOH (80 ml, 10 M). The resulting solution was transferred to autoclave (Teflon-lined, 100 ml) and was kept in a muffle furnace at 120 ^oC for 24 hours. After heating treatment, the final product was washed with

distilled water until the pH of the solution reached 10. About 1g of as-prepared titanium dioxide precipitates was dispersed in 50 ml of distilled water. The solution was transferred in the autoclave and was kept at 200 ^{o}C for another 24 h resulting in the formation of titanium dioxide nanosphere. The prepared TiO_2 nanospheres were centrifuged, washed and finally dried at 60 ^{o}C.

4.2.4 Formation of Pd@Au-TiO_2 nanocomposites

Scheme-4.1 represents the schematic description of the formation of Pd@Au-TiO_2 nanocomposites synthesized by the wet impregnation method. The known amount (200 mg) of the as-prepared TiO_2 nanosphere was dispersed in deionized water (30 ml). The solution was maintained under continuous magnetic stirring for 24 h, after the addition of one weight percent (with respect to titanium dioxide nanosphere) of mono/bimetallic nanostructure to form desired Pd/Au-TiO_2 heterostructure. The Pd@Au nanostructure having different Pd:Au weight ratio (1:1,1:2, and 1:3) after the deposition on the surface of TiO_2 represented as APT-1(Pd_1@Au_1-TiO_2), APT-2 (Pd_1@Au_2-TiO_2), and APT-3 (Pd_1@Au_3-TiO_2).

4.2.5 Catalytic/Photocatalytic activity

The as-prepared Pd@Au nanostructures and their TiO_2 nanocomposites were examined for the selective hydrogenation of cinnamaldehyde (CAL) under both catalytic and photocatalytic reaction conditions. The catalytic hydrogenation reaction was carried out using a 10 mM solution of CAL in 10 ml of IPA (isopropyl alcohol). The reaction mixture was transferred into 25 ml RB (round bottom flask) followed by the addition of 10 mg of mono/bimetallic nanocatalyst (Pd and Au). The reaction temperature was kept constant (60 ^{o}C) under continuous magnetic stirring and under inert atmosphere for 4 hours.

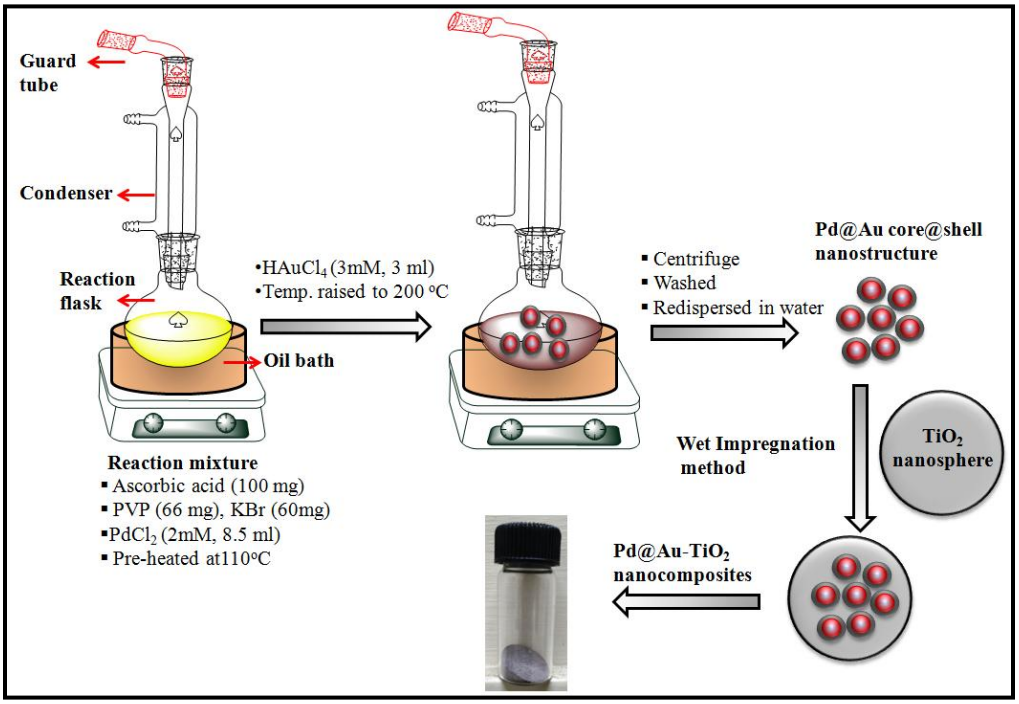

Scheme-4.1: Schematic representation of synthesis of bimetallic Pd@Au-TiO_2 nanocomposite.

The photocatalytic hydrogenation of CAL performed in a 20 ml Pyrex reaction tube containing 10 mM solution of CAL in 10 ml of IPA and 5 mg of Au/Pd-TiO_2 photocatalyst. To sustain the inert atmosphere inside the reaction tube, the reaction mixture was purged with argon/nitrogen for 20 minutes and exposed to direct solar radiation under continuous magnetic stirring for 4 hours. The average solar intensity during the reaction period (June 2019) was found to be ~657 Wm^{-2}. The identification of the hydrogenated product was done by GC-MS and further quantified with GC-FID.

4.3 Results and discussion

Fig. 4.1 shows the optical absorption properties of as-synthesized mono/bimetallic nanoparticles. The monometallic Au nanoparticles showed an intense absorption peak at 529 nm due to its enhanced surface plasmon resonance (SPR) effect and Pd nanoparticles showed an absorption edge at 378 nm. The absorption peak of Au was somewhat blue-shifted from 529 to 518 nm in bimetallic Pd@Au nanostructure having Pd:Au (1:1) weight ratio. Moreover, with increase in the shell thickness or weight ratio of Au, the intensity of the absorption band or SPR band also increased intensively in Pd@Au nanostructure having (1:2) and (1:3) of Pd:Au weight ratio respectively.

The measurement of hydrodynamic size of mono/bimetallic nanostructures was carried out by dispersing 2 mg of the catalyst in 5 ml of deionized water (**Fig. 4.2**). The average hydrodynamic size of monometallic Pd nanoparticles was found to be 98 nm and for bimetallic Pd@Au having (1:1) weight ratio was found to be 126 nm. The hydrodynamic size increased to 139 nm and 157 nm with the increase in shell thickness in Pd@Au (1:2) and Pd@Au (1:3) respectively.

Fig. 4.3 (a,b) represents the TEM images of as-prepared Pd@Au (1:2) core-shell nanostructures. The morphology of these core-shell nanoparticles was found to be hexagonal type structures. The average particle size of Pd@Au nanostructure was within 35-38 nm range. In co-reduction method, difference in electrochemical potential value played an important role in designing the final architecture. The galvanic replacement reaction between Pd and Au resulted in the formation of a core-shell nanostructure consisting of Pd core and Au as a shell. The structural features Pd@Au core-shell nanostructures were further confirmed by STEM and EDS elemental mapping (**Fig. 4.4**).

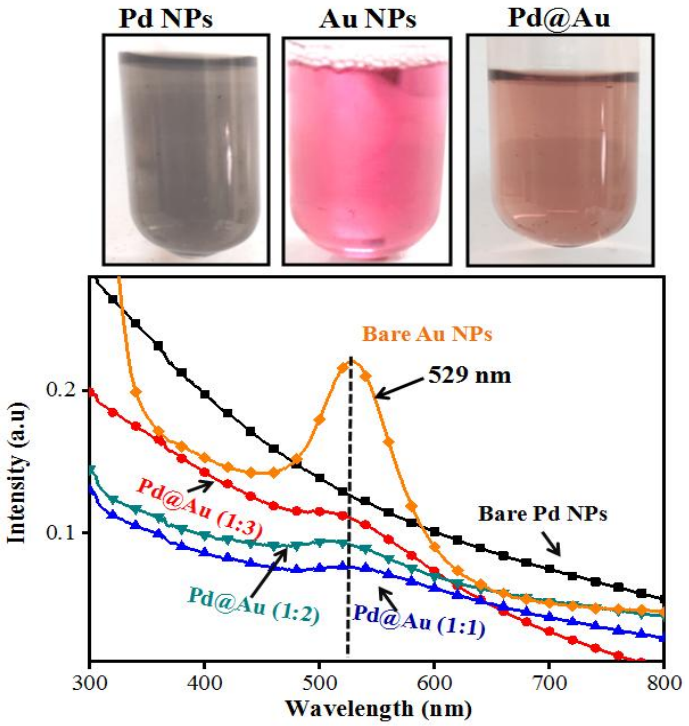

Fig. 4.1: UV-Visible absorption spectra of Pd, Au, and Pd@Au nanostructures in aqueous dispersion and their corresponding color intensity.

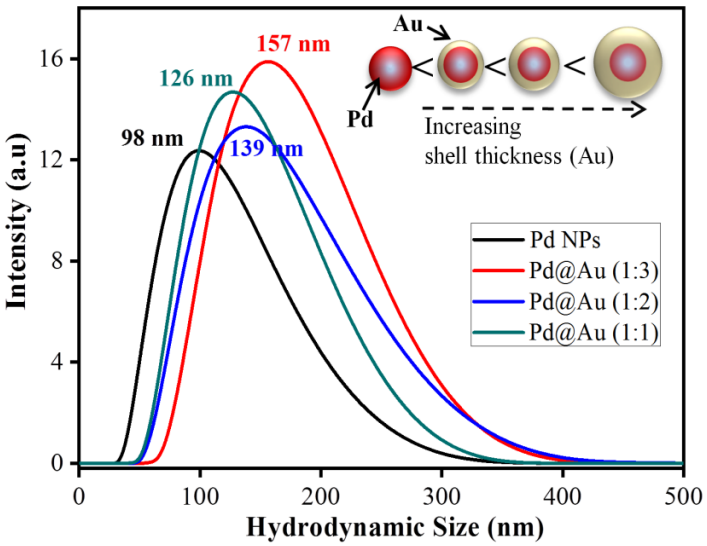

Fig. 4.2: The average hydrodynamic size of bimetallic Pd@Au nanostructures as a function of Au shell thickness.

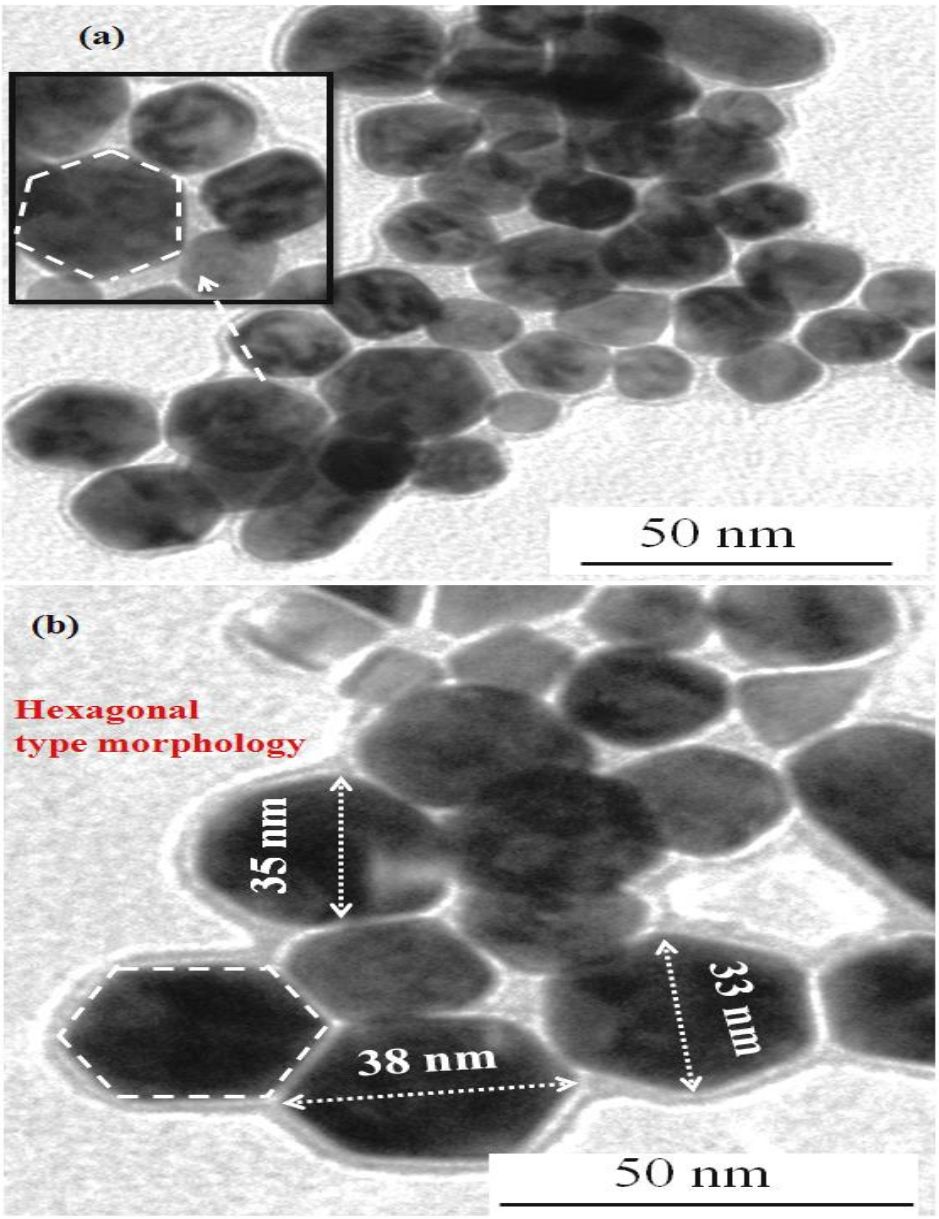

Fig. 4.3: (a-b) TEM images of bimetallic Pd@Au (1:2) core-shell nanostructure.

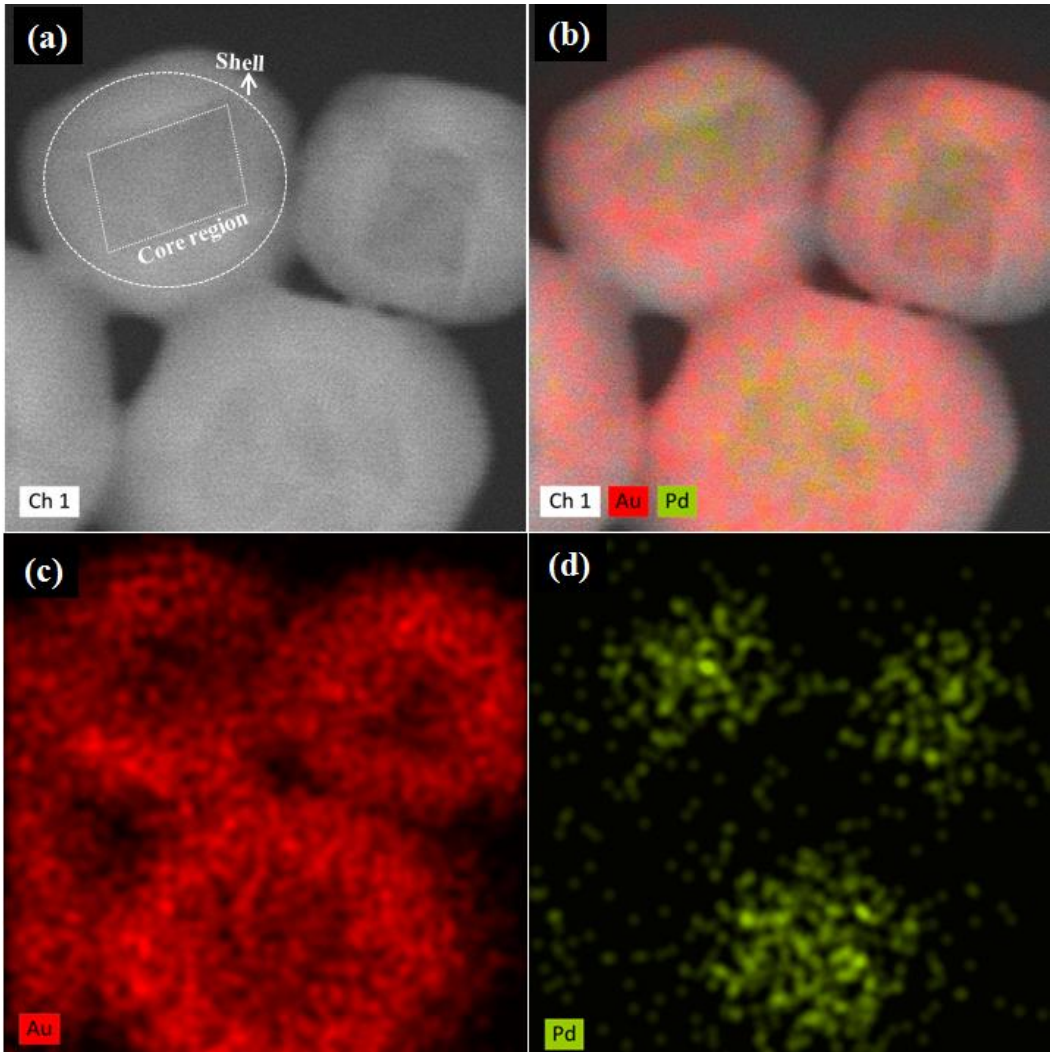

Fig. 4.4: Scanning transmission electron microscopy (STEM) and Energy-dispersive X-ray spectroscopy (EDS) mapping of Pd@Au core-shell nanostructure.

The STEM images (**Fig. 4.4 (a,b)**) displayed noticeable luminance contrast showing the separate boundary for the Pd core and Au shell. Since the atomic density of Au is much higher than Pd. **Fig. 4.4 (c)** showed high intensity of Au over the shell region (shown in red color) and Pd showed the higher intensity in the core region (shown in green color, **Fig. 4.4 (d)**) indicating the formation of Pd@Au nanostructure. The synthesized mono/bimetallic (Pd, Au) nanoparticles were deposited on the surface of titanium dioxide nanosphere (NS) to examine

their co-catalytic activity under both catalytic and photocatalytic conditions. **Fig. 4.5** shows the FESEM images of bare TiO_2 nanospheres.

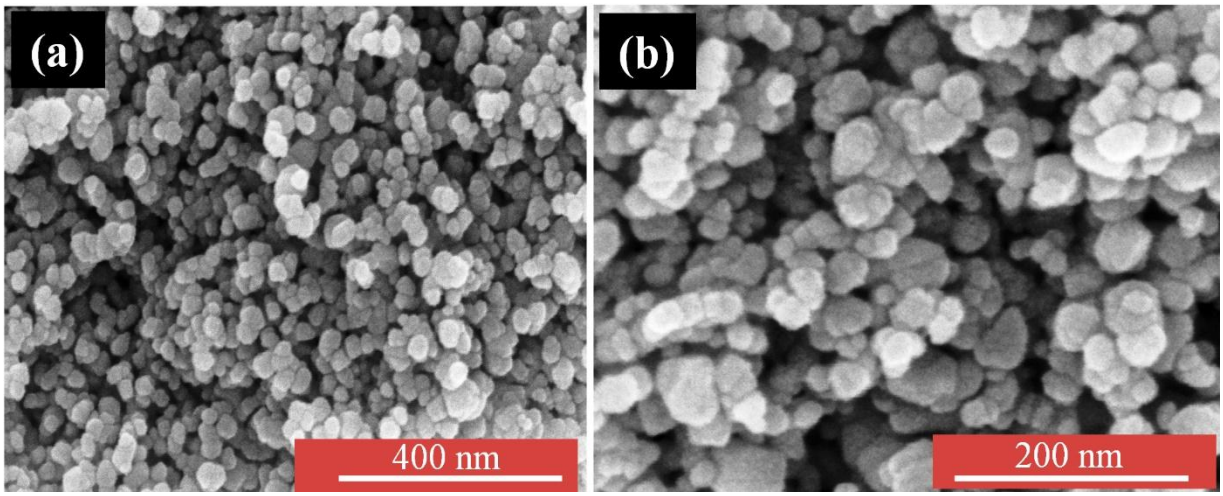

Fig. 4.5: (a-b) FESEM images of as-prepared TiO_2 nanospheres.

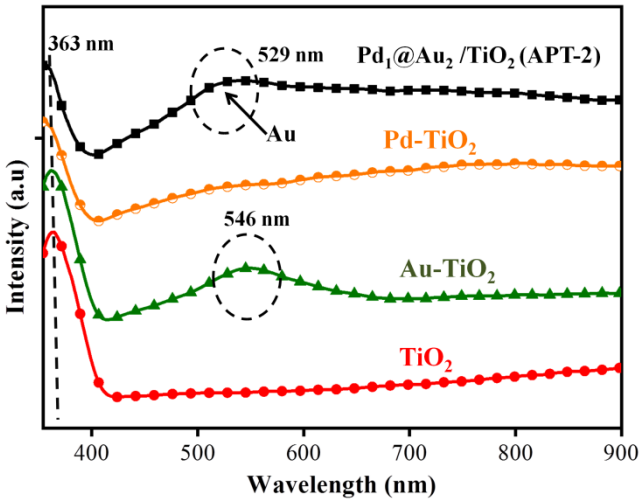

Fig. 4.6: DRS analysis of mono (Pd, Au) and bimetallic ($Pd_1@Au_2$)-TiO_2 (APT-2).

The optical properties of bare and mono/bimetallic-TiO_2 nanocomposites were determined with diffused reflectance spectroscopy (DRS). The intense absorption peak at 363 nm occurred due to the intrinsic bandgap absorption of TiO_2 nanosphere (NS) (**Fig. 4.6**). Comparing with bare TiO_2 NS, the Au nanoparticles show an absorption edge at 546 nm which is blue-shifted to 529 nm in case of bimetallic-TiO_2 nanocomposite (APT-2). Using Tauc plots the band gap energy of bare TiO_2 nanosphere was found to be 3.0 eV. The SPR effect of Au nanoparticles resulted in the reduction of band gap energy to 2.9 eV and 2.94 eV for Au-TiO_2 and bimetallic APT-1 nanocomposite respectively. It was found that with the increase in Au content the band energy was reduced to 2.88 eV and 2.86 eV for APT-2 and APT-3 respectively.

Fig. 4.7 (a-b) shows the SEM-EDS spectrum after deposition of Pd@Au (1:2) on the surface of TiO_2. The existence of different elements in APT-2 ($Pd_1@Au_2$-TiO_2) photocatalyst was confirmed by EDS color mapping (**Fig. 4.67(c-f)**).

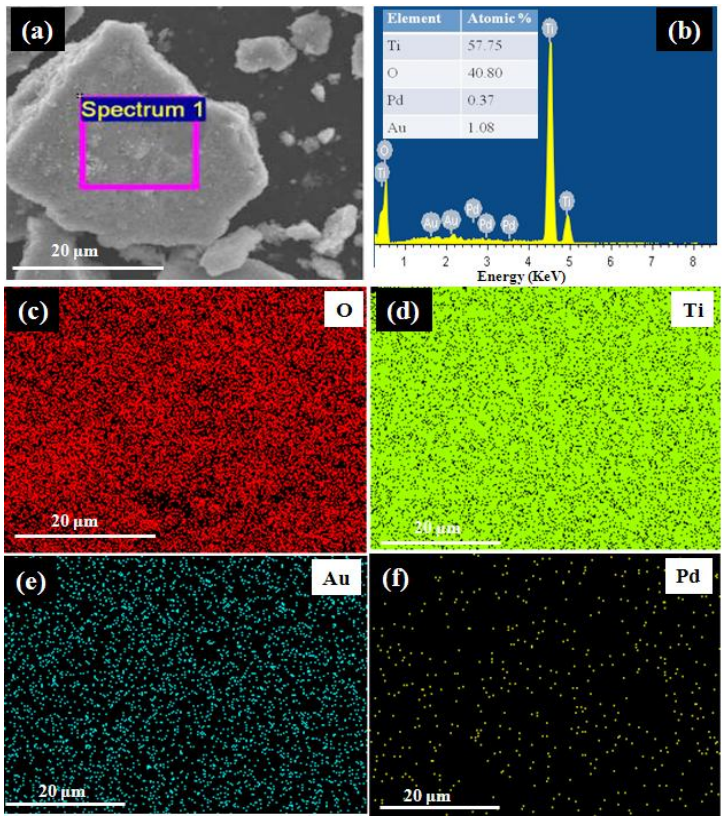

Fig. 4.7: (a-b) SEM-EDS analysis after deposition of Pd@Au on TiO_2 (c-f) Elemental dot mapping of different elements present in APT-2 ($Pd_1@Au_2/TiO_2$) photocatalyst.

The impregnation of Pd, Au, and Pd@Au on the surface of TiO_2 nanospheres (NS) was predicted to suppress the electron-hole recombination that arises due to the effective migration of photoexcited electron form the CB (conduction band) of TiO_2. The PL spectra (**Fig. 4.8**) of bare and mono/bimetallic-TiO_2 photocatalysts were excited at 320 nm. It was observed that bimetallic Pd@Au-TiO_2 displayed a low

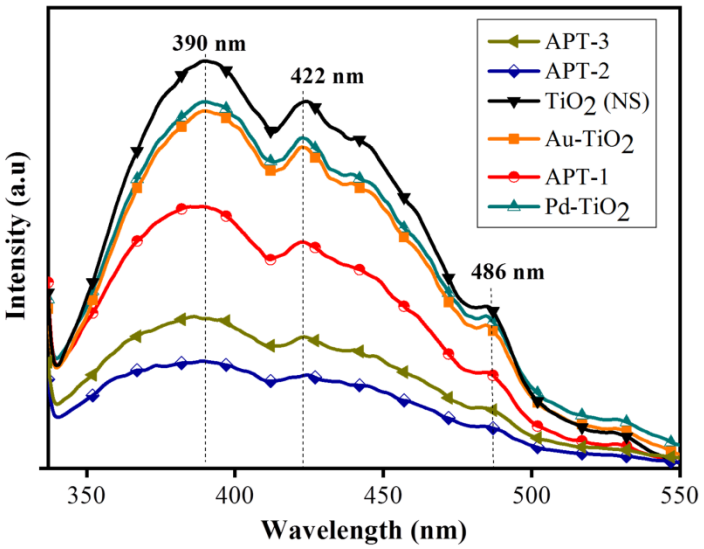

Fig. 4.8: Photoluminescence (PL) spectra of bare TiO_2 and Au/Pd-TiO_2 nanocomposites.

fluorescence signal than Au-TiO_2, and Pd-TiO_2 signifying the effective reduction of barrier height and transfer of photoelectron from TiO_2 → Pd@Au nanostructure relative to monometallic ones. However, in the case of bimetallic-TiO_2 nanocomposites, the APT-2 ($Pd_1@Au_2$-TiO_2) showed a higher reduction in the PL intensity than APT-1 and APT-3 photocatalysts. The synergistic interaction between Au and Pd nanoparticles in APT-2 nanocomposites significantly increased the lifetime of photoexcited electrons-holes upon TiO_2 excitation and resulted in a higher reduction in the PL intensity.

Fig. 4.9 depicts the diffraction pattern of the amorphous structure of the TiO_2 nanosphere and the Pd@Au-TiO_2 (APT-2) catalyst. The X-ray diffraction pattern of TiO_2 matches with the anatase phase (JCPDS-01-086-1157) with a high intensive peak at $2\Theta = 25.3^o$ corresponding to the lattice plane (101). Some low-intensity peaks were also observed at 38.01^o, 48.6^o, 53.9^o, and 62.8^o which were indexed to (112), (200), (211), and (204) respectively.

It was observed that the deposition of Pd@Au on the surface of the TiO_2 nanosphere increases the crystallinity of titanium dioxide. The characteristic diffraction peaks of Pd (JCPDS-01-080-1965/66, represented with the star) were observed at 38.0^o, 48.19^o, 54.6^o and 70.1^o which were assigned to different lattice planes (202), (114), (312) and (662) respectively. The diffraction peaks of Au are represented with hollow circles (JCPDS-01-089-3697).

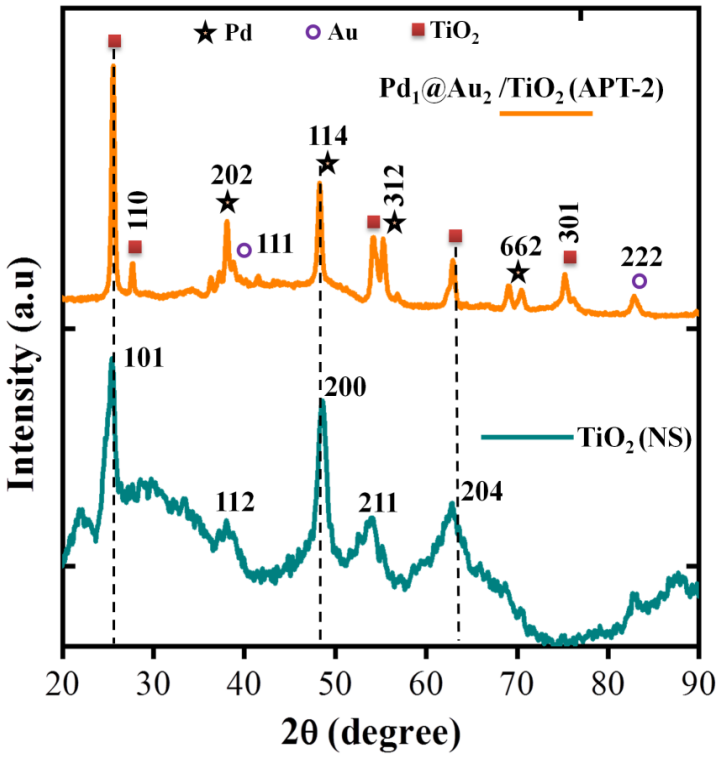

Fig. 4.9: XRD analysis of as-prepared TiO_2 nanospheres (NS) and $Pd_1@Au_2$-TiO_2 (APT-2) nanocomposite.

The presence of diffraction peaks of Au, Pd, and TiO_2 signifies the successful formation of Pd@Au-TiO_2 nanocomposite. The low-temperature nitrogen (N_2) adsorption-desorption isotherms of TiO_2 nanospheres and bimetallic APT-2 nanocomposite are shown in **Fig. 4.10 (a)**.

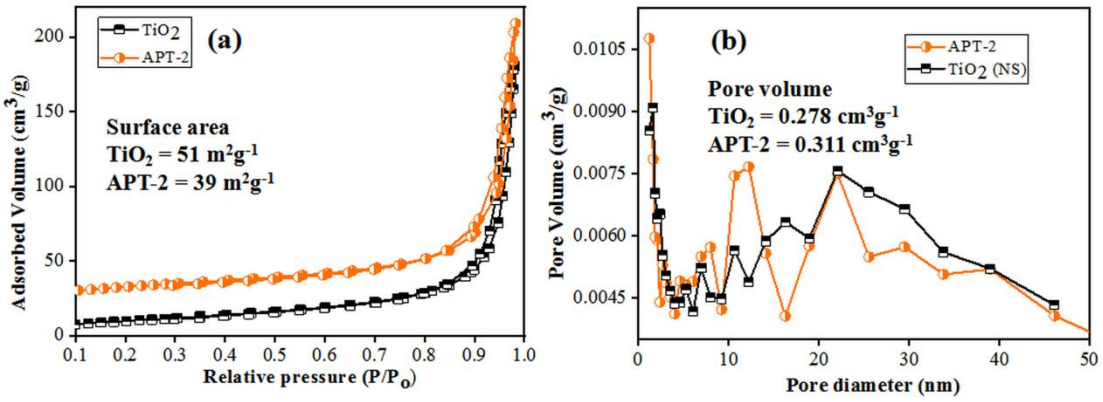

Fig. 4.10: BET surface analysis of TiO_2 and APT-2 catalyst (b) corresponding BJH analysis.

The isotherms strictly obey type four Langmuir hysteresis loop indicating the multilayer and mesoporous behavior of TiO_2 nanospheres having surface area 51 m^2g^{-1} and pore volume 0.278 cm^3g^{-1}. The Barrett-Joyner-Halenda (BJH) analysis curves (**Fig. 4.10 (b)**) indicated that the maximum distribution of pore size took place in the range of 0-15 nm which indicated the presence of mesopores/micropores on the surface of the photocatalyst. The small reduction in the surface area of APT-2 (39 m^2g^{-1}) photocatalyst occurred because the deposition of Pd@Au on the surface of titanium dioxide.

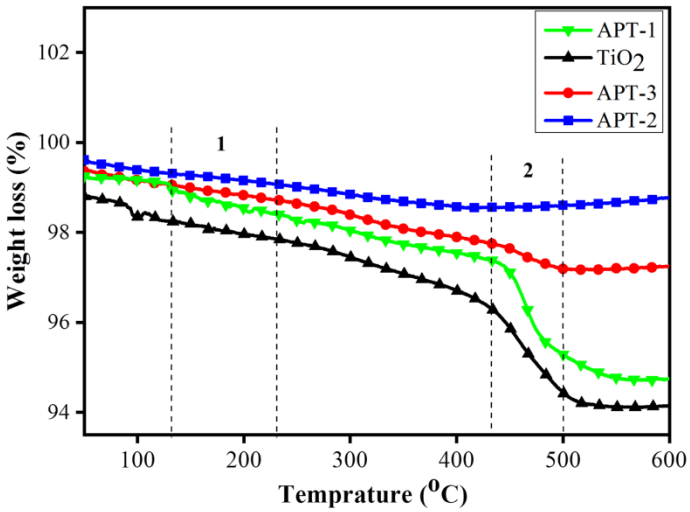

Fig. 4.11: TGA analysis of bare TiO_2 and bimetallic-TiO_2 nanostructures.

The deposition of Pd@Au on the surface of TiO_2 also improved the thermal stability compared to bare titanium dioxide nanospheres. Two mass loss breaks were observed in the TGA curves (**Fig. 4.11**), one curve is due to the moisture loss and the other is assigned to the removal of adsorbed species. The APT-2 ($Pd_1@Au_2$-TiO_2) photocatalyst exhibited higher thermal stability than APT-1 and APT-3. The overall percentage mass loss was found to be ~4.6%, ~4.5%, ~2.2% and ~0.8% for TiO_2, APT-1, APT-3 and APT-2 respectively.

The XPS survey spectrum (**Fig. 4.12**) revealed the presence of different elements Ti, O, Pd, Au and their chemicals states in APT-2 nanocomposite. The core-level Ti 2p spectrum (**Fig. 4.13 (a)**) is deconvoluted in two different peaks centered at 458.2 eV and 464.1 eV respectively [44].

The difference of 5.9 eV between the Ti $2p_{3/2}$ and $2p_{1/2}$ signals is in good agreement with reported valves showing the existence of Ti^{+4} states. The high-resolution XPS spectrum of oxygen (O1s) is fitted into three different signals corresponding to O^{2-} (529.6 eV), O-H binding (531.5 eV) and O_2 (free oxygen, 533.5eV) respectively (**Fig. 4.13 (b)**) [45]. The core-level XPS spectrum of Pd 3d (**Fig. 4.13 (c)**) consist of two dominated signals which are assigned to Pd $3d_{5/2}$ (335.3 eV) and $3d_{3/2}$ (341.9 eV) respectively indicating the existence of palladium in the metallic state ($Pd^{(0)}$). A shoulder peak is also observed at 336.6 eV and deconvoluted into small signals, signify the existence of Pd in the +2 oxidation state also [46]. Similarly, the high-resolution Au 4f spectrum (**Fig. 4.13 (d)**) fitted with two deconvoluted peaks at 82.9 eV ($4f_{5/2}$) and 86.8 eV ($4f_{7/2}$) which are assigned to the metallic state of gold ($Au^{(0)}$) [47].

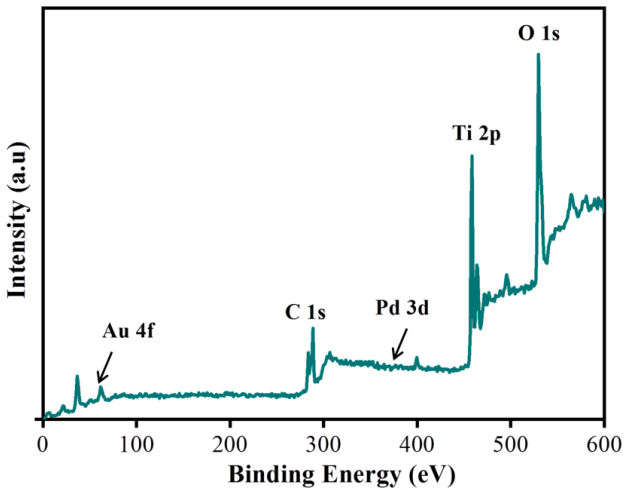

Fig. 4.12: XPS survey spectra of APT-2 (Pd@Au (1:2)/TiO_2) photocatalyst.

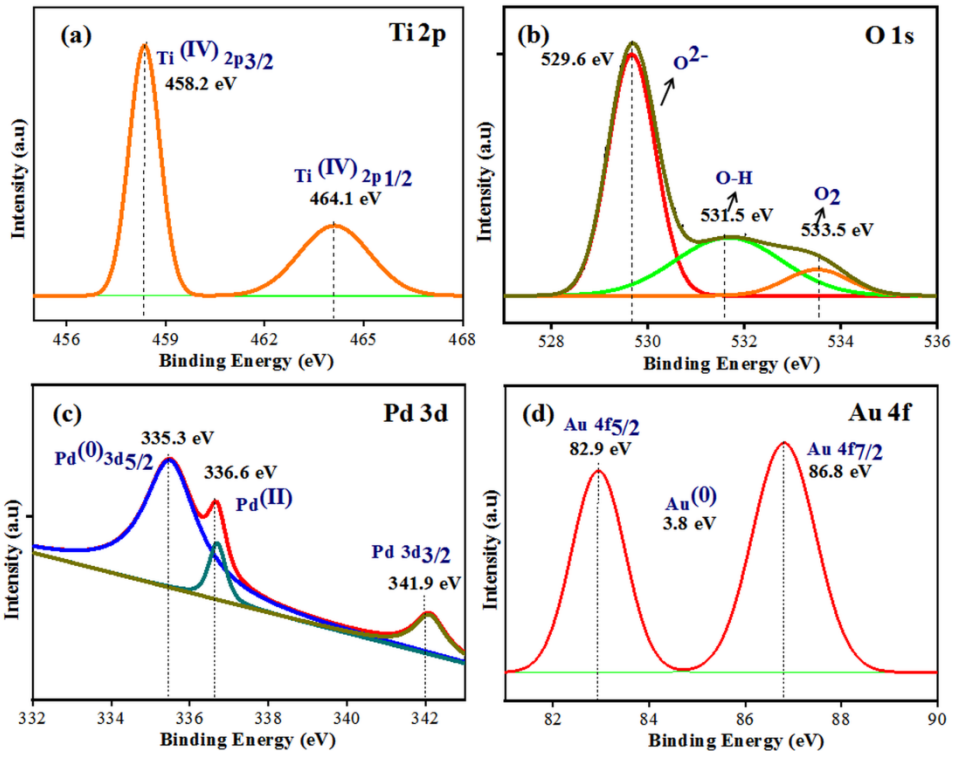

Fig. 4.13: XPS (X-ray photoelectron spectroscopy) analysis of APT-2 (a) Ti, (b) O, (c) Pd, (d) Au.

The hydrogenated products of CAL (cinnamaldehyde) and COAL (crotonaldehyde) were determined via GC-MS and GC-FID by comparing the retention time and the peak area with the standard samples. The selective hydrogenation of CAL was first analyzed using mono/bimetallic Pd@Au nanostructure without titanium dioxide support. It was observed that bimetallic Pd@Au exhibited superior activity and selectivity than their corresponding monometallic analogues. The higher activity of Pd@Au credited to their synergistic interactions and different electronic arrangement as compared to monometallic Pd and Au nanoparticles. Furthermore, these mono/bimetallic nanostructures were deposited on the surface of TiO_2 nanospheres (as a co-catalyst) and examined for selective hydrogenation of cinnamaldehyde (CAL) and crotonaldehyde (COAL) under catalytic/photocatalytic reaction conditions. **Fig. 4.14** shows the photocatalytic reaction scheme for cinnamaldehyde hydrogenation with magnified GC-FID and GC-MS spectra after the hydrogenation of CAL.

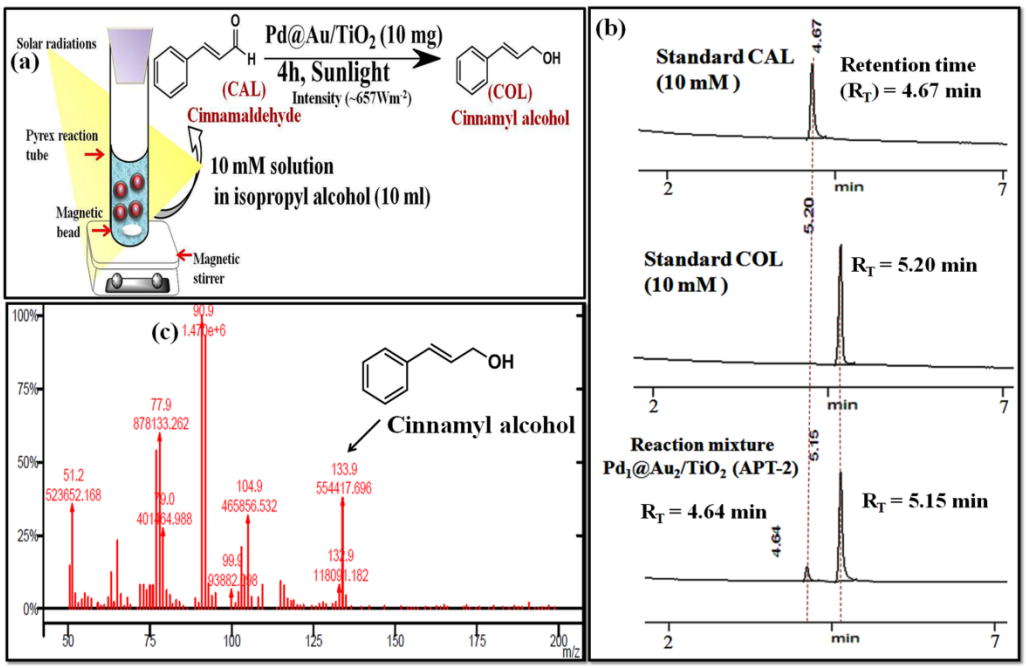

Fig. 4.14: (a) Reaction scheme (b) magnified GC-FID spectra of standard CAL (10 mM), COL (10 mM), and reaction mixture (c) GC-MS analysis after hydrogenation of CAL with APT-2 photocatalyst.

Fig. 4.15 represents the histogram showing the comparative percentage yield obtained for the CAL hydrogenation carried out under catalytic and photocatalytic conditions (solar radiation). The APT-2 ($Pd_1@Au_2/TiO_2$) photocatalyst exhibited a higher percentage yield (98 %) for the selective conversion of cinnamaldehyde to cinnamyl alcohol than APT-1 (67 %) and APT-3 (83 %) under solar radiation. The synergistic and co-catalytic effect of Pd@Au deposited on the surface of TiO_2 prevents the recombination rate of photo-excited electron-hole pairs and improves the effective charge transfer at bimetallic-TiO_2 hetero-junction resulting in the enhanced selectivity and the yield for cinnamaldehyde hydrogenation in comparison with monometallic ones. Moreover, higher activity of bimetallic $Pd_1@Au_2/TiO_2$ (APT-2) nanostructure under catalytic conditions occurred because of an increase in the surface area with TiO_2 support and also due to increase in the gold weight ratio. **Table-4.1** represents the yield and selectivity obtained for CAL hydrogenation using as-prepared different catalysts under sunlight.

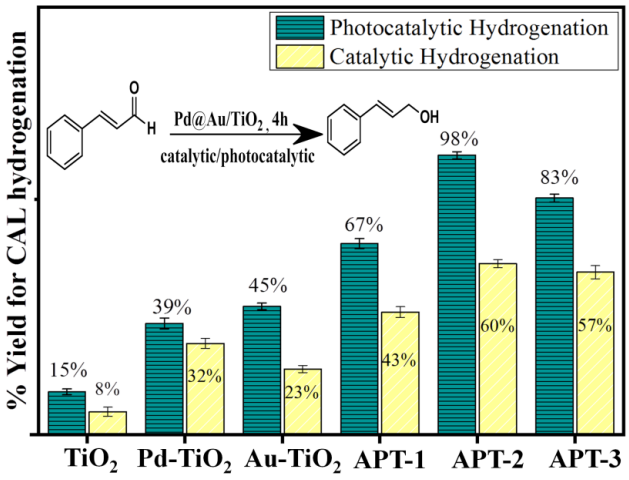

Fig. 4.15: The % yield obtained for cinnamaldehyde hydrogenation (catalytic/photocatalytic) using different catalysts.

Table-4.1: The percentage yield and selectivity obtained for CAL hydrogenation using as-prepared different catalysts under solar radiation.

Sr. No.	Catalyst	Reaction time (h)	% Yield	% Selectivity
1	TiO_2	4	15	21
2	Au-TiO_2	4	39	63
3	Pd-TiO_2	4	45	45
4	APT-1 ($Pd_1@Au_1$-TiO_2)	4	67	100
5	APT-2 ($Pd_1@Au_2$-TiO_2)	4	98	100
6	APT-3 ($Pd_1@Au_3$-TiO_2)	4	83	100

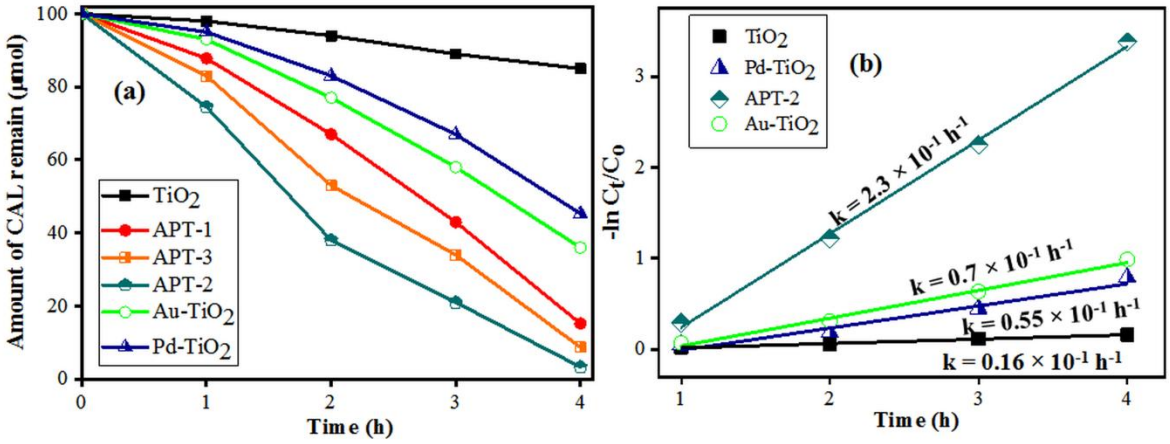

Fig. 4.16: (a) Time course study for the cinnamaldehyde hydrogenation (b) rate constant obtained under solar radiation.

Fig. 4.16 (a) represents the time-dependent hydrogenation of the CAL and remaining amount of CAL (µmol) after performing hydrogenation reaction with mono/bimetallic-TiO_2 photocatalysts under solar radiation. The kinetic studies reveal (**Fig. 4.16 (b)**) that the selective cinnamaldehyde hydrogenation follows the pseudo 1st order kinetics and APT-2 photocatalyst exhibited higher rate constant of $k = 2.3 \times 10^{-1}$ h^{-1} followed by Au-TiO_2 ($k = 0.7 \times 10^{-1}$ h^{-1}), Pd-TiO_2 ($k = 0.55 \times 10^{-1}$ h^{-1}), and bare TiO_2 ($k = 0.16 \times 10^{-1}$ h^{-1}) respectively. The photocatalytic activity of Pd/Au-TiO_2 was further investigated for the selective hydrogenation of crotonaldehyde.

Fig. 4.17 shows the percentage yield and selectivity obtained for photocatalytic hydrogenation of crotonaldehyde under sunlight. It has been found that APT-2 photocatalyst displayed higher yield (96 %) and selectively (100 %) followed by APT-3 and APT-1 nanocomposite. The comparison of the present study using Pd@Au-TiO_2 photocatalyst with the reported catalyst for the cinnamaldehyde hydrogenation is represented in **Table-4.2**

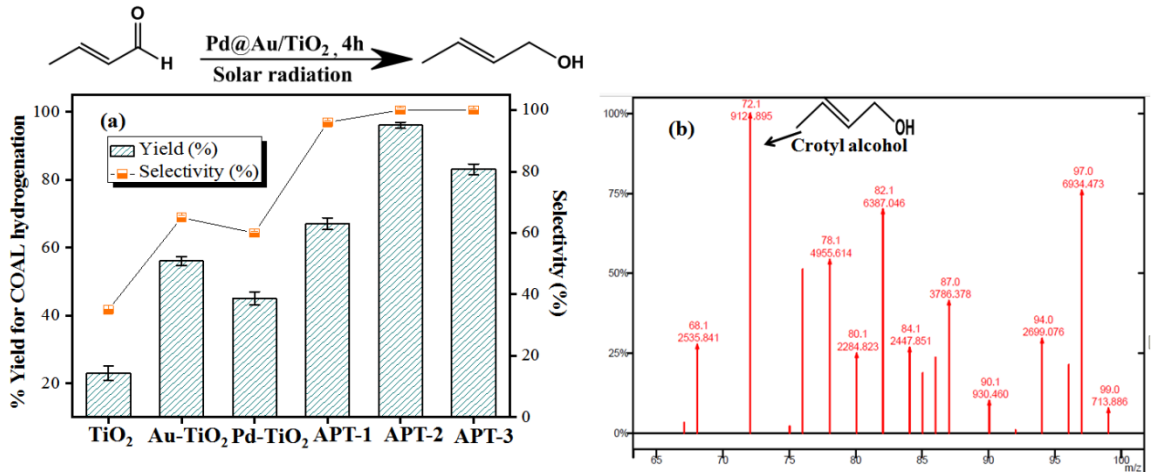

Fig. 4.17: (a) The % yield and selectivity obtained for crotonaldehyde hydrogenation (b) corresponding GS-MS analysis.

Table-4.2: The comparison of the Pd@Au-TiO_2 photocatalyst with the reported catalyst for the cinnamaldehyde hydrogenation.

Sr. No.	Reactant	Catalyst	Temperature	Reaction time (h)	% Yield	Reference
1	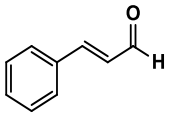	Pd-Sn/C	130 ^oC Under hydrogen pressure	48	88	[21]
2	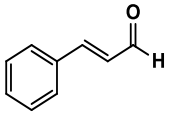	CoPt	100-180 ^oC	3	96	[28]
3	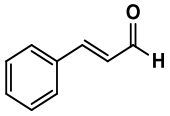	Pd-Ir/SiO_2	50 ^oC Under hydrogen pressure	—	80	[29]
4	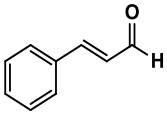	Pt-Re/rGO	120 ^oC Under hydrogen pressure	4	95	[48]
5	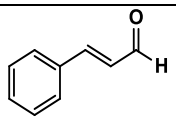	Au/Pt/TiO_2	Visible light	5	95	[49]
6	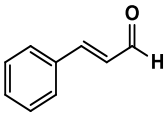	Pd@Au-TiO_2	— Under Sunlight Without H_2	4	98	Present Work

Mechanism for cinnamaldehyde hydrogenation

The sunlight driven photo-induced catalytic process promotes the hydrogenation of cinnamaldehyde (CAL) over the bimetallic Pd@Au-TiO_2 photocatalyst. The expected mechanism for CAL hydrogenation is represented in **Scheme-4.2**. When Pd@Au-TiO_2 is irradiated with solar radiation, the localized surface plasmon resonance (LSPR) of Au promotes the migration of photo-electrons from conduction band (CB) to the valance band (VB) of TiO_2. Based on previous studies [25, 49], the carbonyl group (C=O) present in CAL selectively adsorbed on the electron-rich center of TiO_2. The synergistic interaction between Pd@Au promotes efficient charge transfer process from Pd@Au nanoparticles to the conduction band of TiO_2 and facilitates the conversion of isopropyl alcohol into acetone. Thus, the deposition of bimetallic Pd@Au nanocatalyst on the surface of TiO_2 resulted in higher activity and selectivity for CAL hydrogenation than monometallic Pd/Au-TiO_2 nanocomposites.

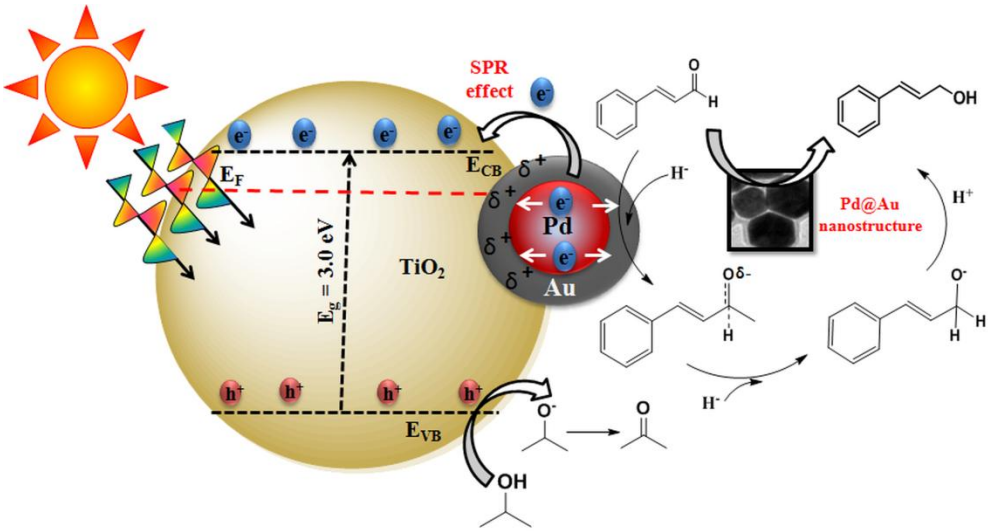

Scheme-4.2: The possible reaction mechanism for the CAL hydrogenation under sunlight.

The key benefit of using these heterogeneous photocatalysts lies in their remarkable stability and consistent catalytic performance. The photocatalytic activity and stability of APT-2 photocatalyst were investigated for CAL hydrogenation by reusing it for five consecutive cycles under the same reaction conditions (**Fig. 4.18**). Comparing with the first cycle, there is a little loss observed in the photocatalytic performance of the catalyst. The minor loss in the activity occurred due to the fact that some amount of catalyst was lost in its recovering process or some blockage in the active sites of the catalyst.

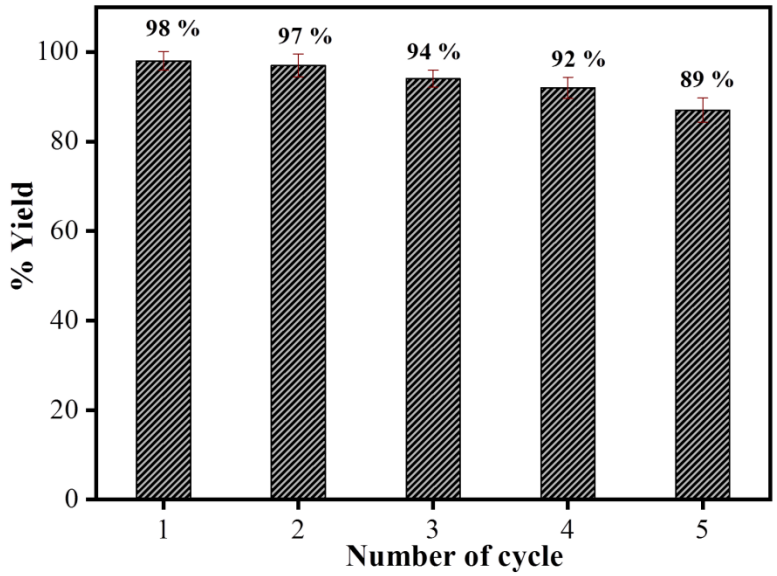

Fig. 4.18: The % yield obtained after reusability test of APT-2 photocatalyst for CAL hydrogenation.

References

[1] I.S. Pieta, A. Rathi, P. Pieta, R. Nowakowski, M. Hołdynski, M. Pisarek, A. Kaminska, M.B. Gawande, R. Zboril, Appl. Catal., B, 244 (2019) 272-283.

[2] B. Seemala, R. Kumar, C.M. Cai, C.E. Wyman, P. Christopher, React. Chem. Eng., 4 (2019) 261-267.

[3] C.M. Olmos, L.E. Chinchilla, A. Villa, J.J. Delgado, A.B. Hungría, G. Blanco, L. Prati, J.J. Calvino, X. Chen, J. Catal., 375 (2019) 44-55.

[4] L. Qin, Z. Zeng, G. Zeng, C. Lai, A. Duan, R. Xiao, D. Huang, Y. Fu, H. Yi, B. Li, Appl. Catal., B, 259 (2019) 118035.

[5] S. Gupta, T.S. Khan, B. Saha, M.A. Haider, Ind. Eng. Chem. Res., (2019).

[6] A. Bathla, B. Pal, J. Ind. Eng. Chem., 67 (2018) 486-496.

[7] H. Miyamura, F. Tobita, A. Suzuki, S. Kobayashi, Angew. Chem. Internat. Ed., (2019).

[8] M.I. Qadir, F. Bernardi, J.D. Scholten, D.L. Baptista, J. Dupont, Appl. Catal., B, 252 (2019) 10-17.

[9] M. Wu, J.-H. Pang, P.-P. Song, J.-J. Peng, F. Xu, Q. Li, X.-M. Zhang, New J. Chem., 43 (2019) 1964-1971.

[10] W. Li, B. Li, M. Meng, Y. Cui, Y. Wu, Y. Zhang, H. Dong, Y. Feng, Appl. Surf. Sci., 487 (2019) 1008-1017.

[11] L. Ma, Q. Zhang, C. Wu, Y. Zhang, L. Zeng, Anal. Chim. Acta, 1055 (2019) 17-25.

[12] P.-J. Tsai, K.-L. Chuang, C.-J. Yang, H.-T. Lee, F.-H. Lu, J. Alloys Compd, 785 (2019) 191-199.

[13] B.S. Sivamaruthi, V.S. Ramkumar, G. Archunan, C. Chaiyasut, N. Suganthy, J. Drug Delivery Sci. Technol., 51 (2019) 139-151.

[14] M.B. Gawande, A. Goswami, T. Asefa, H. Guo, A.V. Biradar, D.-L. Peng, R. Zboril, R.S. Varma, Chem. Soc. Rev., 44 (2015) 7540-7590.

[15] K.D. Gilroy, A. Ruditskiy, H.-C. Peng, D. Qin, Y. Xia, Chem. Rev., 116 (2016) 10414-10472.

[16] M. Wu, X. Wu, L. Zhang, A. Abdelhafiz, I. Chang, C. Qu, Y. Jiang, J. Zeng, F. Alamgir, Electrochim. Acta, 306 (2019) 167-174.

[17] A. Bathla, B. Pal, J. Ind. Eng. Chem., (2019).

[18] Y. Yang, J. Liu, Z.-W. Fu, D. Qin, J. Am. Chem. Soc., 136 (2014) 8153-8156.

[19] C. Vriamont, T. Haynes, E. McCague-Murphy, F. Pennetreau, O. Riant, S. Hermans, J. Catal., 329 (2015) 389-400.
[20] H. Rong, Z. Niu, Y. Zhao, H. Cheng, Z. Li, L. Ma, J. Li, S. Wei, Y. Li, Chem. Eur. J., 21 (2015) 12034-12041.
[21] J. Zhao, X. Xu, X. Li, J. Wang, Catal. Commun., 43 (2014) 102-106.
[22] E. Plessers, D.E. De Vos, M.B. Roeffaers, J. Catal., 340 (2016) 136-143.
[23] A. Yepez, J.M. Hidalgo, A. Pineda, R. Černý, P. Jíša, A. Garcia, A.A. Romero, R. Luque, Green Chem., 17 (2015) 565-572.
[24] M. Kołodziej, A. Drelinkiewicz, E. Lalik, J. Gurgul, D. Duraczyńska, R. Kosydar, Appl. Catal., A, 515 (2016) 60-71.
[25] Y. Zhang, C. Chen, W.-b. Gong, J.-y. Song, Y.-p. Su, H.-m. Zhang, G.-z. Wang, H.-j. Zhao, Chin. J. Chem. Phys., 30 (2017) 467.
[26] S. Cattaneo, S.J. Freakley, D.J. Morgan, M. Sankar, N. Dimitratos, G.J. Hutchings, Catal. Sci. Technol., 8 (2018) 1677-1685.
[27] A. Bathla, B. Pal, ChemistrySelect, 3 (2018) 4738-4744.
[28] T. Yuan, D. Liu, Y. Pan, X. Pu, Y. Xia, J. Wang, W. Xiong, Catalysis Letters, 149 (2019) 851-859.
[29] T. Szumełda, A. Drelinkiewicz, F. Mauriello, M.G. Musolino, A. Dziedzicka, D. Duraczyńska, J. Gurgul, J. Chem., 2019 (2019).
[30] B. Tamami, H. Mahdavi, Tetrahedron, 59 (2003) 821-826.
[31] S. Fleischer, S. Zhou, K. Junge, M. Beller, Angew. Chem. Int. Ed., 52 (2013) 5120-5124.
[32] Z. Guo, C. Xiao, R.V. Maligal-Ganesh, L. Zhou, T.W. Goh, X. Li, D. Tesfagaber, A. Thiel, W. Huang, ACS Catal., 4 (2014) 1340-1348.
[33] R.A. Al-Alawi, K. Laxman, S. Dastgir, J. Dutta, Appl. Surf. Sci., 377 (2016) 200-206.
[34] N. Siddqui, B. Sarkar, C. Pendem, L.S. Konthala, T. Sasaki, A. Bordoloi, R. Bal, Catal. Sci. Technol., 7 (2017) 2828-2837.
[35] L. He, J. Ni, L.C. Wang, F.J. Yu, Y. Cao, H.Y. He, K.N. Fan, Chem. Eur. J., 15 (2009) 11833-11836.
[36] D. Ma, S. Zhai, Y. Wang, A. Liu, C. Chen, Molecules, 24 (2019) 330.
[37] S. Rohani, A. Ziarati, G.M. Ziarani, A. Badiei, T. Bürgi, Catal. Sci. Technol., (2019).

[38] M. Pradenas, J. Yáñez, S. Ranganathan, D. Contreras, P. Santander, H.D. Mansilla, Water Environ. Res., 91 (2019) 157-164.
[39] M. Edelmannová, K.-Y. Lin, J.C. Wu, I. Troppová, L. Čapek, K. Kočí, Appl. Surf. Sci., 454 (2018) 313-318.
[40] B. Boro, B. Gogoi, B. Rajbongshi, A. Ramchiary, Renew. Sust. Energ. Rev., 81 (2018) 2264-2270.
[41] A. Monga, A. Bathla, B. Pal, Sol. Energy, 155 (2017) 1403-1410.
[42] A. Crake, K.C. Christoforidis, R. Godin, B. Moss, A. Kafizas, S. Zafeiratos, J.R. Durrant, C. Petit, Appl. Catal., B, 242 (2019) 369-378.
[43] R.A. Rather, D. Pooja, P. Kumar, S. Singh, B. Pal, J. Cleaner Prod., 175 (2018) 394-401.
[44] N. Chen, D. Deng, Y. Li, X. Liu, X. Xing, X. Xiao, Y. Wang, Sci. Rep., 7 (2017) 7692.
[45] C. Su, L. Liu, M. Zhang, Y. Zhang, C. Shao, CrystEngComm, 14 (2012) 3989-3999.
[46] L. Kibis, A. Titkov, A. Stadnichenko, S. Koscheev, A. Boronin, Appl. Surf. Sci., 255 (2009) 9248-9254.
[47] Z. Jiang, W. Zhang, L. Jin, X. Yang, F. Xu, J. Zhu, W. Huang, J. Phys. Chem. C, 111 (2007) 12434-12439.
[48] Z. Wei, X. Zhu, X. Liu, H. Xu, X. Li, Y. Hou, Y. Liu, Chin. J. Chem. Eng., 27 (2019) 369-378.
[49] Y. Ma, Z. Li, Appl. Surf. Sci., 452 (2018) 279-285.

Conclusion and Future Aspects

Chapter-1: Summarizes a brief introduction about the transition metal nanocatalysis and the importance of bimetallic core-shell nanostructures of Au@Ag, Pd@Au, Au@Cu, Cu@Zn, Pd@Ni, etc. over monometallic counterparts and these have been described in terms of recent literature survey on the subject matter. The research gaps are also identified and are presented in this chapter. The synergistic interaction and role of reduction potential values in the synthesis of core-shell nanostructure via galvanic displacement have been discussed in detail. Since, the conventional hydrogenation of various organic compounds (cinnamaldehyde, crotonaldehyde, quinoline, benzaldehyde) is usually carried out under harsh reaction conditions viz., the use of H_2 under high pressure, high temperature and involving the use of different metal hydrides. This chapter depicts the importance of photocatalytic hydrogenation of unsaturated compounds using bimetallic-TiO_2 nanocomposites under ultra-violet, visible, and solar radiation.

The standard procedure used in the synthesis of bimetallic nanostructures and a short description of different characterization techniques like UV-Visible spectroscopy, Dynamic light scattering, X-ray diffraction, Bruneaur-Emmet-Teller analysis, Morphological analysis, Thermal gravimetrical analysis, and Gas chromatography, etc. which are used to determine the optical and structural properties of bimetallic nanostructures have been represented in this chapter.

Chapter-2: Describes the synthesis of bimetallic Pd@Ni core-shell nanostructures via galvanic replacement reaction which were further deposited over the surface of mesoporous titanium dioxide. The heterogeneous Pd@Ni/mTiO_2 nanocomposite was found to be highly effective photocatalyst for the selective hydrogenation of the carbonyl group compared to monometallic nanostructures. The photocatalytic hydrogenation occurred at room temperature under UV-light using isopropyl alcohol as a scavenger. Mesoporous TiO_2 support provided a larger catalytic surface area, improve selectivity, and yield for the reaction without using a foreign base and high temperature. The Pd@Ni/mTiO_2 nanocatalyst remained active and stable for five consecutive reaction cycles under the same photochemical conditions. The photocatalytic performance of mesoporous titanium dioxide was improved by using a balanced amount of co-

catalyst (Pd and Ni). Moreover, higher surface area, pore distribution, and work function (barrier height) were also observed to have a strong effect on the photocatalytic efficiency of the catalyst.

Chapter-3: This chapter discloses the formation of Cu@Zn nanostructure where Cu act as a core and Zn as a shell imparted to (001) faceted titania nanosheets. The synthesized Cu@Zn nanoparticles via galvanic interactions effectively used as good catalyst/co-catalyst for selective hydrogenation of quinoline under visible light radiation. The synergistic interaction between Cu@Zn-TiO_2 hetero-junction promoted the efficient electron and hydride transfer for quinoline hydrogenation relative to their Zn/Cu-TiO_2 counterparts. It was observed that hydrogenation capacity and co-catalytic activity of Cu@Zn was improved by varying Cu:Zn weight ratio. Under visible light radiation, the optimized ZCT-3 (Cu_3@Zn_1-TiO_2) nanocatalyst showed superior photocatalytic activity and was found to be active for five successive cycles without any significant loss. The larger surface area, mesoporosity, and impregnation of Cu@Zn on the surface of TiO_2 nanosheets facilitated the formation of new catalytic active sites for adsorption, transportation of H_2 and photoelectron in hydrogenation reaction compared to monometallic ones.

Chapter-4: Well-defined bimetallic Pd(core)@Au(shell) has been successfully synthesized via galvanic replacement reaction between $PdCl_2$ and $HAuCl_4$. The as-prepared Pd@Au nanostructure was examined for the selective hydrogenation of cinnamaldehyde (CAL) under catalytic and photocatalytic reaction conditions. It was found that bimetallic Pd@Au nanocatalyst exhibited enhanced activity and selectivity for CAL hydrogenation compared to monometallic (Pd and Au) analogues. Under solar radiation, a significant improvement in the selective hydrogenation of CAL was observed, upon utilizing Pd@Au as co-catalyst after deposition on the surface of TiO_2. The photocatalytic performance of Pd@Au-TiO_2 was also affected by varying the shell thickness (weight ratio of Au) and the optimized APT-2 exhibited a higher rate constant for CAL hydrogenation. The deposition of bimetallic Pd@Au nanocatalyst on the surface of TiO_2 resulted in higher activity and selectivity for photocatalytic CAL hydrogenation in comparison to monometallic Pd/Au-TiO_2 nanocomposites.

Future Aspects

In view of the work reported in this thesis which involved the synthesis of bimetallic core-shell (Pd@Ni, Cu@Zn, and Pd@Au) nanostructures via galvanic displacement reaction, suitable bimetallic core@shell nanostructures can be fabricated for desired catalytic applications by analyzing the reduction potential values of different metals. The incorporation of one metal over another not only improved the functionality, stability, and dispersibility but also reduced the consumption of expensive material. Furthermore, titanium dioxide is a promising, effective material and found numerous applications in the area of catalysis/photocatalysis. This work also reported the viable procedures to synthesize different shaped titanium dioxide like mesoporous TiO_2, (001) faceted titania nanosheets and nanospheres which showed higher photocatalytic performance than commercially available titanium dioxide (P25).

The conventional hydrogenation of different unsaturated organic compounds is usually carried out under harsh reaction conditions viz., the use of H_2 under high pressure, high temperature and involving the use of different metal hydrides i.e. $NaBH_4$, $LiAlH_4$. In order to avoid the use of these explosives, high-cost and tedious reaction conditions, the metal-TiO_2 catalyzed hydrogen transfer under light radiation is a promising alternative technique for the selective hydrogenation reactions. Here, it has been demonstrated that the spectral response and photocatalytic efficiency of titanium dioxide in solar or visible light can be improved by impregnating bimetallic nanostructures. Bimetallic Pd@Ni-TiO_2, Cu@Zn-TiO_2, and Pd@Au-TiO_2 nanocomposites displayed superior catalytic activity for the selective hydrogenation of benzaldehyde, quinoline, and cinnamaldehyde respectively under light radiation. Hence, bimetallic-TiO_2 is a promising catalyst for the selective hydrogenation of different challenging molecules and other industry-relevant compounds that work in an effective, simple, and greener way. In extension to this research work, bimetallic core-shell nanostructures of non-Nobel metals (Rh, Ir, Re, Ni, etc.) and bimetallic nanostructures encapsulated organic framework could be employed for the selective hydrogenation reactions under light radiation.

List of Publications

1. **Aadil Bathla** and Bonamali Pal (2020)**.** Superior co-catalytic activity of Pd(core)@Au(shell) nanocatalyst imparted to TiO_2 for the selective hydrogenation under solar radiations. ***Solar Energy, 205,*** **292-301, IF= 4.6**, **ISSN: 0038-092X**
2. **Aadil Bathla** and Bonamali Pal (2019). Bimetallic Cu(core)@Zn(shell) co-catalyst impregnated TiO_2 nanosheets (001 faceted) for the selective hydrogenation of quinoline under visible light irradiation. ***Journal of Industrial and Engineering Chemistry 79,*** **314-325, IF= 4.97, ISSN: 1226-086X**
3. **Aadil Bathla** and Bonamali Pal (2018). Bimetallic Pd@Ni-mesoporous TiO_2 nanocatalyst for highly improved and selective hydrogenation of carbonyl compounds under UV light radiation. ***Journal of Industrial and Engineering Chemistry, 67,*** **486-496, IF= 4.97, ISSN: 1226-086X**
4. **Aadil Bathla** and Bonamali Pal. Bimetallic Ag@M (M= Zn, Cu, Ni, Pd and Fe) nanostructures for electrochemical hydrogen evolution reaction (**under preparation**).

Other publications

1. Anila Monga, **Aadil Bathla,** and Bonamali Pal (2017). A Cu-Au bimetallic co-catalysis for the improved photocatalytic activity of TiO_2 under visible light radiation. ***Solar Energy, 155,*** **1403-1410, IF= 4.6, ISSN: 0038-092X**
2. **Aadil Bathla,** Deepak Singla, and Bonamali Pal (2019). Highly efficient $CaCO_3$-CaO extracted from tap water distillation for effective adsorption and photocatalytic degradation of malachite green dye. ***Materials Research Bulletin, 116,*** **1-7, IF= 3.3, ISSN: 0025-5408**
3. **Aadil Bathla** and Bonamali Pal (2018). Catalytic Selective Hydrogenation and Cross Coupling Reaction Using Polyvinylpyrrolidone-Capped Nickel Nanoparticles. ***Chemistry Select, 3*** **(17), 4738-4744**, **IF= 1.7, ISSN: 2365-6549**
4. **Aadil Bathla,** Rayees Ahmad Rather, Tamanna Poonia, and Bonamali Pal (2019). Morphology Dependent Photocatalytic Activity of CuO/CuO–TiO_2 Nanocatalyst for Degradation Methyl Orange under Sunlight. ***Journal of nanotechnology and nanoscience.*** **IF= 1.5, ISSN: 1533-4880**

5. **Aadil Bathla**, Davinder Kaur and Bonamali Pal Impact of metal ions (Cr^{+6}/Mn^{+7}) loaded $CaCO_3$ extracted from tap water for adsorption/degradation of toxic pollutants under sunlight. (**under communication**)

Book Chapter

1. **Aadil Bathla** and Bonamali Pal. Enhanced co-catalysis of bimetallic nanostructures for catalytic and photocatalytic applications. (Invited book chapter from Elsevier, **submitted**)

Conferences and Workshops

1. **Aadil Bathla,** and Bonamali Pal, Catalytic vs. Photocatalytic hydrogenation of unsaturated carbonyls using bimetallic Pd@Au core-shell nanostructure. 12th National Conference **CESAI-2020**, held at Punjabi University, Patiala (Poster, **Best poster award**). 19th-20th February, 2020
2. **Aadil Bathla,** and Bonamali Pal, Bimetallic core@shell nanostructure of galvanic metals for selective catalytic/photocatalytic hydrogenation. International conference on advance material (**ICAM-2019**), organized by Jamia Millia Islamia, New Delhi (poster). 06th -07th March, 2019
3. **Aadil Bathla,** and Bonamali Pal, Titanium oxide fabricated bimetallic core@shell nanostructure for the selective catalytic/photocatalytic hydrogenation. 11th National Conference **RTCES-2019** held at Punjabi University, Patiala (Poster). 07th-08th February, 2019
4. **Aadil Bathla,** and Bonamali Pal, Participated in international workshop (**GIAN)** on Nanostructured metal oxides for sensing and environmental applications held at Punjab University, Chandigarh. 06th-10th August, 2018.
5. **Aadil Bathla,** and Bonamali Pal, Participated in national workshop on career awareness for science graduates organized by Thapar Institute of Engineering and Technology, Patiala, 07th March, 2018.
6. **Aadil Bathla,** and Bonamali Pal, Participated in national workshop on intellectual property rights and patenting organized by **PSCST** at Thapar Institute of Engineering and Technology, Patiala, 17th February, 2018.
7. **Aadil Bathla,** and Bonamali Pal, Catalytic selective hydrogenation and cross coupling reaction using polyvinylpyrrolidone caped nickel nanoparticles. 5th international conference on advance nanomaterials and nanotechnology (**ICANN-2017**) organized by IIT-Guwahati, Aasam 18th-21st December, 2017 (poster).
8. **Aadil Bathla,** and Bonamali Pal, Participated in national science day celebration (**NSDC-2017**) held at Thapar Institute of Engineering and Technology, Patiala, 18th February, 2017.

9. **Aadil Bathla,** and Bonamali Pal, Participated in national workshop on hydrogen energy at National institute of solar energy Gurugram, Haryana, 23rd-24th January, 2017.
10. **Aadil Bathla,** and Bonamali Pal, Participated in 2nd international conference on Harnessing Engineering, Technology and Innovation for Sustainable growth (**HETIS**), held at Punjab University, Chandigarh. 29th-30th September, 2016.

Solar Energy 205 (2020) 292–301

Contents lists available at ScienceDirect

Solar Energy

journal homepage: www.elsevier.com/locate/solener

Superior co-catalytic activity of Pd(core)@Au(shell) nanocatalyst imparted to TiO_2 for the selective hydrogenation under solar radiations

Aadil Bathla, Bonamali Pal*

School of Chemistry and Biochemistry, Thapar Institute of Engineering & Technology, Patiala 147004, India

ARTICLE INFO

Keywords:
Pd@Au core–shell nanostructure
Cinnamaldehyde hydrogenation
Pd@Au-TiO_2 co-catalysis
Sunlight photocatalysis
Galvanic replacement reaction

ABSTRACT

The bimetallic core–shell nanostructures of galvanic metals have gained considerable scientific interest in improving the TiO_2 photocatalysis under solar radiations over the monometallic analogues. In the present research work, Pd@Au core–shell supported TiO_2 nanostructures were synthesized via galvanic replacement reaction and were examined for their catalytic/ photocatalytic hydrogenation. Three different types of bimetallic Pd@Au nanostructure were synthesized by varying Pd:Au weight ratio i.e. (1:1), (1:2) and (1:3). DLS measurements revealed that with increasing Au weight ratio, the hydrodynamic size increases from 126 to 157 nm. The optical studies showed a considerable blue shift in the absorption band of Au nanoparticles from 529 to 518 nm in the case of Pd@Au (1:1). The co-existence of absorption characteristic of Pd and Au suggests the successful synthesis of bimetallic nanostructure. STEM and EDS mapping further confirmed the formation of Pd@Au nanostructure with inner Pd core and outer Au shell. Bimetallic Pd@Au nanocatalyst displayed superior activity and selectivity towards hydrogenation of cinnamaldehyde in comparison to monometallic analogues. However, when Pd@Au nanostructures were impregnated on the surface of TiO_2, a significant improvement in the hydrogenation reaction was observed under solar radiations relative to catalytic conditions. The photocatalytic performance of Pd@Au-TiO_2 was found to be varied as a function of shell thickness and the optimized APT-2 (Pd_1@Au_2-TiO_2) photocatalyst exhibited higher rate constant ($2.3 \times 10^{-1}\ h^{-1}$) for cinnamaldehyde hydrogenation. Hence, the plasmonic Pd@Au-TiO_2 hetero-junction could be a promising greener photocatalyst for selective hydrogenation of unsaturated carbonyls for large scale industrial applications.

1. Introduction

Bimetallic nanostructure of galvanic metals (Cu, Zn, Au, Pd, Ni, etc.) with different morphological appearance frequently shows superior catalytic/photocatalytic activities compared to their monometallic analogues (Bathla and Pal, 2018; Gupta et al., 2019; Olmos et al., 2019; Pieta et al., 2019; Qin et al., 2019; Seemala et al., 2019). The tremendous performance of these bimetallic nanoparticles credited to their diverse arrangement/combination and synergistic interaction between two different metal atoms. Among the different forms of bimetallic nanoparticles, core@shell nano-arrangement constructed via co-reduction method (based on galvanic interaction) found numerous applications in different research fields like catalysis, photocatalysis, sensing, and drug delivery (Li et al., 2019; Ma et al., 2019; Miyamura et al., 2019; Qadir et al., 2019; Sivamaruthi et al., 2019; Tsai et al., 2019; Wu et al., 2019a). The electrochemical potential difference between the two metals plays a crucial role in galvanic replacement reaction and also in finalizing the structural design (Gawande et al., 2015; Gilroy et al., 2016). Wu et al. (2019b) reported the synthesis of bimetallic Cu@Pt nanostructure by galvanic replacement reaction and observed that Cu@Pt display superior performance for oxygen reduction reaction relative to monometallic counterparts. Bathla and Pal (2019) reported the formation of Cu@Zn/TiO_2 core–shell nanostructure via galvanic interaction method for the selective quinoline hydrogenation under visible light irradiations. Similarly, Yang *et al.* demonstrated the formation of Ag@Au core–shell nanocubes via galvanic replacement reaction between $AgNO_3$ and $HAuCl_4$ and studied for its enhanced SERS activity (Yang et al., 2014).

The selective hydrogenation of α-β unsaturated aldehydes to their corresponding alcohols is of great interest from the scientifically and industrial point of view. The hydrogenated product of cinnamaldehyde (CAL) i.e. cinnamyl alcohol (COL) is an essential component for the synthesis of fine chemicals, perfumes, and cosmetics (Plessers et al., 2016; Rong et al., 2015; Vriamont et al., 2015; Zhao et al., 2014). The selective hydrogenation of CAL to COL is a challenging task as it involves both C=C and C=O bonds. From the previous studies (Kołodziej

* Corresponding author.
E-mail address: bpal@thapar.edu (B. Pal).

https://doi.org/10.1016/j.solener.2020.05.038
Received 18 November 2019; Received in revised form 11 May 2020; Accepted 14 May 2020

Journal of Industrial and Engineering Chemistry 79 (2019) 314–325

Contents lists available at ScienceDirect

Journal of Industrial and Engineering Chemistry

journal homepage: www.elsevier.com/locate/jiec

Bimetallic Cu(core)@Zn(shell) co-catalyst impregnated TiO_2 nanosheets (001 faceted) for the selective hydrogenation of quinoline under visible light irradiation

Aadil Bathla, Bonamali Pal*

School of Chemistry and Biochemistry, Thapar Institute of Engineering & Technology, Patiala 147004, Punjab, India

ARTICLE INFO

Article history:
Received 5 April 2019
Received in revised form 3 July 2019
Accepted 4 July 2019
Available online 12 July 2019

Keywords:
Cu@Zn nanostructure
Co-catalytic activity
Cu@Zn/TiO_2 co-catalysis
Quinoline hydrogenation
Visible light photocatalysis

ABSTRACT

Bimetallic nanostructures have gained immense importance owing to their enhanced co-catalytic effect in improving photocatalytic activity of TiO_2 for various applications relative to monometallic ones. However, the use of bimetallic core@shell catalyst/nanocatalyst for hydrogenation of important industrial organic is not much explored relative to conventional metal catalysts. In this respect, the present study demonstrated the synthesis of core@shell (Cu@Zn) nanostructure based on their galvanic interactions. TEM analysis confirmed the formation of Cu@Zn nanoparticles with a shell thickness of 195 nm. It was observed that with increasing Cu:Zn weight ratio (1:1, 2:1, and 3:1) the average hydrodynamic size increases from 198 to 267 nm. These Cu@Zn nanostructures showed superior co-catalytic activity after impregnation on (001) faceted titanium nanosheets (surface area = 72.8 $m^2 g^{-1}$) for the selective hydrogenation of quinoline under visible light radiations. The optimized Cu@Zn(3:1)/TiO_2 photocatalyst showed enhanced conversion, selectivity, and higher rate constant ($k = 2.1 \times 10^{-1} h^{-1}$) compared to Cu and Zn-$TiO_2$ nanocomposites. The superior activity of Cu@Zn-TiO_2 photocatalyst was attributed to the synergistic interaction occurring at bimetallic-TiO_2 interface which effectively promotes the transfer of electron and hydride (H^-) for quinoline hydrogenation. The conventional hydrogenation of quinoline required high temperature, solvents, expensive bases and involved multistep procedure. Therefore, the use of Cu@Zn-TiO_2 photocatalyst might be a greener approach for the selective hydrogenation of industrial important unsaturated organic compounds under light radiations.

Introduction

The bimetallic core@shell nanostructures (NS) composed of two different galvanic metals (Pd, Au, Ni, Zn, Cu, and Ag) have aroused tremendous attention in the area of catalysis, photocatalysis, and electronics [1–7]. The core@shell nano-arrangement exhibited fascinating electronic, optical and surface properties [8–12] due to synergistic interaction between two metals relative to their individual monometallic components. A variety of methods have been employed by different researchers, but one pot co-reduction method based on galvanic interaction between the metals is a promising method to synthesized core@shell nanoparticles [13–16]. In this method, reduction potential (E^0 value) of two metals plays a decisive role in the final structural design. In the presence of weak reducing agent (glucose, ascorbic acid etc.) the two metals were reduced in consecutive order based on their reduction potential values. Jiang et al. [17] reported the synthesis of bimetallic Au@Ag NS via galvanic interaction between two soluble metal salts arise due to difference in their E^0 values ($E^0_{Ag+/Ag} = +0.80$ eV Vs SHE; $E^0_{Au3+/Au} = +0.93$ eV Vs SHE). Xu et al. [18] reported the synthesis of nanoporous bimetallic core@shell structure of Cu & Pt based on their galvanic interaction. Similarly, Sarkar and Manthiram [19] reported the synthesis of bimetallic core–shell (Pt@Cu) NS by galvanic displacement between copper and platinum for the oxygen reduction reaction in fuel cells.

The selective hydrogenation of *N*-heteroarenes is a crucial step for various pharmaceutical and petrochemical industries in the manufacturing of different fine products [20–23]. The conversion of quinoline (Qu) to 1,2,3,4-tetrahydroquinoline is a challenging

* Corresponding author.
E-mail address: bpal@thapar.edu (B. Pal).

https://doi.org/10.1016/j.jiec.2019.07.007
1226-086X/

Journal of Industrial and Engineering Chemistry 67 (2018) 486–496

Contents lists available at ScienceDirect

Journal of Industrial and Engineering Chemistry

journal homepage: www.elsevier.com/locate/jiec

Bimetallic Pd@Ni-mesoporous TiO_2 nanocatalyst for highly improved and selective hydrogenation of carbonyl compounds under UV light radiation

Aadil Bathla, Bonamali Pal*

School of Chemistry and Biochemistry, Thapar Institute of Engineering & Technology, Patiala 147004, India

ARTICLE INFO

Article history:
Received 15 May 2018
Received in revised form 10 July 2018
Accepted 19 July 2018
Available online 29 July 2018

Keywords:
Bimetallic-nanocatalyst
Co-catalytic activity
Mesoporous TiO_2
Pd@Ni/mTiO_2 nanocomposites
Photo-catalytic hydrogenation

ABSTRACT

Bimetallic Pd@Ni nanostructure exhibited enhanced co-catalytic activity for the selective hydrogenation of benzaldehyde compare to their monometallic counterparts. Impregnation of these mono/bimetallic nanostructures on mesoporous TiO_2 leads to several surface modifications. The bimetallic PNT-3 (Pd_3@Ni_1/mTiO_2) exhibited large surface area (212 $m^2 g^{-1}$), and low recombination rate of the charge carriers (e^--h^+). The hydrogenation reaction was analyzed under controlled experiments. It was observed that under UV-light irradiations and saturated hydrogen atmosphere the bimetallic PNT-3 photocatalyst display higher rate constant $k = 5.31 \times 10^{-1} h^{-1}$ owing to reduction in the barrier height which leads to efficiently transfer of electron at bimetallic/mTiO_2 interface.

Introduction

Metal nanoparticles are extensively used in hydrogenation, oxidation-reduction reactions, and carbon-carbon cross coupling [1–9] because of their small size and extremely large surface area. Besides the large numbers of catalytic applications, the single metal nanocatalysts still not able to accomplished the activity and selectivity requirements for the reactions. These specific properties of metal nanoparticles are improved by depositing another metal on the surface of first metal. In recent years, bimetallic nanocomposites have gained considerable attention in the area of catalysis [10–13]. Bimetallic nanocatalysts exhibited distinctive electronic and chemical properties compared to their parent metals. The enhancement in their catalytic performance is credited to the synergistic or electronic interaction between the metals, results in higher selectivity and increased yield for the reaction [14–17]. Monga et al. [18] explored that different shape bimetallic Au@Ag nanostructure displayed better photo-activity for the nitro aromatic reduction than monometallic ones. Similarly, Chen et al. [19] reported the bimetallic Au-Pd supported on SBA-15 display superior catalytic activity for the benzyl alcohol oxidation than monometallic (Au & Pd) nanocomposites.

The hydrogenation of carbonyl group (C=O) is the commercially important step for a large number of applications and mostly used in the formation of various drugs, paints, pesticides and polymers [20–23]. Nowadays, many efforts have been made in the preparation of an effective catalyst for the selective hydrogenation of carbonyl compounds to their corresponding alcohol. Although both mono and bimetallic catalyst have been used for this purpose, bimetallic catalyst exhibits a particular interest because of their superior activity, stability, and selectivity [24–26]. Among the bimetallic nanostructure palladium-based catalysts have gain particular interest in the field of hydrogenation. Luo et al. [27] reported that PdAu and PtAu alloy nanostructure for the allyl alcohol hydrogenation and observed that PdAu nanostructure exhibits enhanced activity relative to PtAu alloy nanostructure. Similarly, Zhang et al. [28] reported that bimetallic Pd-Ru supported on gamma alumina exhibited superior activity for hydrogenation of 2-ethylanthraquinone than monometallic nanocatalysts.

Furthermore, heterogeneous semiconductor photocatalyst has been widely employed in various organic transformations like hydrogenation of alkenes, alkynes, ketones and aldehydes [29–32]. Out of various semiconductors, TiO_2 is considered promising material for the various photocatalytic activities despite the fact that titanium dioxide (P25) has certain limitations: low surface area, fast electron-hole pair recombination. Recently, Mesoporous TiO_2 has immerged as an effective material to overcome these obstructions. Large surface area, high porosity and brilliant electronic properties of mesoporous TiO_2 results in efficient

* Corresponding author.
E-mail address: bpal@thapar.edu (B. Pal).

https://doi.org/10.1016/j.jiec.2018.07.023
1226-086X/

Solar Energy 155 (2017) 1403–1410

Contents lists available at ScienceDirect

Solar Energy

journal homepage: www.elsevier.com/locate/solener

A Cu-Au bimetallic co-catalysis for the improved photocatalytic activity of TiO_2 under visible light radiation

Anila Monga, Aadil Bathla, Bonamali Pal *

School of Chemistry and Biochemistry, Thapar University, Patiala 147004, Punjab, India

ARTICLE INFO

Article history:
Received 2 May 2017
Received in revised form 26 July 2017
Accepted 31 July 2017

Keywords:
Au-Cu bimetallic co-catalyst
Au@Cu/TiO_2 nanocomposite
Co-Catalytic activity
Visible light photo-catalysis

ABSTRACT

This study represents the co-catalytic activity of mono/bimetallic loaded titanium dioxide (TiO_2) nanocomposite of copper (Cu) & gold (Au) for the photo-reduction of aromatic nitro compounds and the photo-oxidation of salicylic acid. It was observed that the average hydrodynamic size of Cu (~21 nm) and Au (~25 nm) increased after the formation of core-shell structure (~36 nm and~38 nm for Cu@Au and Au@Cu respectively). The morphological studies revealed the uniform coating of Cu-shell of thickness~2.1 nm over Au core. Moreover, in optical analysis a considerable blue-shift in the absorption band of Cu@Au (600 nm-559 nm) and a red-shift in Au@Cu (528–580 nm) with significant change in color were observed with increasing the amount of Au and Cu, respectively. Under visible light irradiation these bimetallic/TiO_2 nanocomposite showed higher activity for the reduction of 3-nitroacetophenone and 1-chloro-3-nitrobenzene and oxidation of salicylic acid comparative to their monometallic counter parts with a higher rate constant $k = 0.97 \times 10^{-2}\ min^{-1}$ (Au@Cu/TiO_2), $k = 0.65 \times 10^{-2}\ min^{-1}$ (Cu@Au/TiO_2) relative to monometallic ($k = 0.34 \times 10^{-2}\ min^{-1}$ (Cu/TiO_2) and $k = 0.29 \times 10^{-2}\ min^{-1}$)) for the oxidation of salicylic acid. The higher activity of bimetallic/TiO_2 nanocomposite is ascribed to the decrease in work function (4.2 for Au@Cu/TiO_2 & 4.6 for Cu@Au/TiO_2) resulting in the proficient transfer of electrons at bimetallic-TiO_2 interface.

1. Introduction

Bimetallic core-shell nanostructure of two different metals attracts a lot of interest in comparison to their respective monometallic nanoparticles (NPs) because of their strong catalytic, electronic and fascinating optical property (Ma et al., 2010; Pande et al., 2007; Wang and Li, 2011). Since the catalytic performance is highly surface dependent (Kahraman et al., 2009; Yang et al., 2008), the addition of second metal on the surface of another metal alter the interface property and charge transfer process (Sangpour et al., 2010) due to the bifunctional effect (Zhou et al., 2013) (or synergistic effect) resulting in the higher selectivity and yield of a catalytic reaction. Moreover, the bimetallic nanocomposites (NCs) of noble metals (Au, Ag, Cu) (Chimentao et al., 2007; Gerber et al., 2004; Hai et al., 2014; Mancheño-Corvo and Martín-Duque, 2006; Zielińska-Jurek et al., 2011) have been broadly investigate because of another brilliant property possessed by these metals known as localized surface plasmon resonance (LSPR) i.e. the coherent oscillation with concurrent visible region (Gerber et al., 2004; Methadone et al., 2010). It has been reported that bimetallic core-shell of Au/Ag exhibit higher activity for glucose oxidation (Rasmussen et al., 2005) and for reduction of p-nitrophenol(Dong and Zhang, 2014) relative to monometallic Au and Ag. Wang et al. (Wang and Li, 2011) reported the Au@Pt core-shell nanostructure enhance the electrocatalytic activity for methanol oxidation compared to conventional monometallic Pt. The various physicochemical and catalytic properties of bimetallic nanocomposite can also be altered as a function of their size, shape and thickness of core and shell (Glaus et al., 2002; Jayakumar et al., 2010; Ma et al., 2010; Shankar et al., 2004). A recent report (Monga and Pal, 2015) depicted that the Au nanorod$_{core}$-Ag$_{shell}$ exhibit higher selectivity for the reduction of 1,3-dinitrobenzene to 3-nitroaniline relative to Au nanosphere$_{core}$-Ag$_{shell}$ and their respective monometallic counterparts. Similarly Ma and coworkers (Ma et al., 2010) studied the changes occur in optical properties of Au@Ag nanocubes by varying the Ag shell thickness from 1.2 nm to 20 nm. Furthermore, these metal nanoparticles (NPs) show a good co-catalytic behavior when supported on certain metal oxide.

Previous reports have suggested that the impregnation of these monometallic/bimetallic nanoparticles (NPs) on semiconductor (ZnO, WO_3, TiO_2 etc.) (Glaus et al., 2002; Li et al., 2017; Mittal et al., 2014; Primo et al., 2011; Shet and Vidya, 2016; Wang and Li, 2011) enhance the photocatalytic activity of semiconductor.

* Corresponding author.
E-mail address: bpal@thapar.edu (B. Pal).

http://dx.doi.org/10.1016/j.solener.2017.07.084
0038-092X/

ChemPubSoc Europe

DOI: 10.1002/slct.201800699

Chemistry SELECT Full Papers

Catalysis

Catalytic Selective Hydrogenation and Cross Coupling Reaction Using Polyvinylpyrrolidone-Capped Nickel Nanoparticles

Aadil Bathla and Bonamali Pal*[a]

This study signifies the size-dependent catalytic activity of Ni-nanocatalyst for the selective hydrogenation of cinnamaldehyde and Suzuki-Miyaura cross-coupling reaction. A series of polyvinylpyrrolidone capped nickel nanoparticles (NPs) with variation in their size are synthesized by polyol method. The morphological studies revealed that average size of Ni-NPs (Ni-NP1, Ni-NP2, and Ni-NP3) lies in the range of 10–12, 7–9, and 3–5 nm respectively. The optical measurements showed a significant blue shift in the absorption spectra for Ni-NPs with decreasing particle size. The magnetic hysteresis loop revealed that the remanent magnetization (M_R) decreases and coercivity (H_C) increases with the decrease in particle size demonstrating a distinct size effect. The Ni-NP3 was observed to possess higher surface area (79 m^2g^{-1}) and efficient activity for the selective hydrogenation of cinnamaldehyde to cinnamyl alcohol and also in the biphenyl formation via C–C cross-coupling reaction relative to Ni-NP1, Ni-NP2, and commercially available Raney Ni.

Introduction

Over the past few years, metal nanoparticles have attracted a lot of interest for their wide range of application in various fields like catalysis,[1] optoelectronics,[2] and magnetic devices[3] etc. Due to their small size, large surface area and a large fraction of atoms on the surface, they exhibit superior catalytic activity relative to their bulk counterparts.[4] Nickel nanoparticles (NiNP) are widely employed in the catalytic hydrogenation reaction.[1f,5] It has been reported that nanosized nickel catalyst exhibited superior activity, selectivity and thermal stability in comparison to conventional Raney nickel catalyst.[6] Du *et al.* have reported that nickel nanoparticles display higher activity and selectivity for the hydrogenation of p-nitrophenol to p-aminophenol relative to commercial available Raney nickel (RNi).[7] Similarly, Wang *et al.* reported that NiNP exhibit higher catalytic activity in comparison with RNi for the hydrogenation of p-nitrophenol.[8]

The selective hydrogenation of α, ß- unsaturated aldehydes to corresponding alcohols over the heterogeneous catalyst is an important step for the synthesis of fine chemicals particularly for the pharmaceuticals, cosmetics, and perfumes on a larger scale.[9] These unsaturated carbonyl compounds have both C=O, C=C groups and the hydrogenation of C=C occurs more preferentially than C=O group.[10] So, it is highly desirable to fabricate a catalyst that would favor the selective hydrogenation of C=O group which results in the formation of unsaturated alcohol. A number of noble metals like (Au, Pt, and Pd)[11] and non-noble (Fe, Ni, Co)[12] have been used for this purpose. However, the metal nanoparticles are found to be thermodynamically unstable, resulting in the aggregation of nanoparticles and reduction in their catalytic efficiency and selectivity for various reactions. A number of stabilizing agents like polymers, dendrimers, tetraalkylammonium salts, and surfactants have been used to prevent the metal nanoparticles from sintering.[13] The polyvinylpyrrolidone (PVP) is well known stabilizing agent which is catalytically inert and have no considerable effect on the catalytic activity of metal nanoparticles.[14] The PVP molecules bind weakly with nanoparticles so as to prevents the metal nanoparticle from the aggregation and provide the maximum exposed surface for various catalytic reactions.

Furthermore, the transition metal based cross-coupling such as Suzuki-Miyaura,[15] Heck,[16] Sonogashira[17] reactions are important for the development of C–C bonds. These coupling reactions have attracted a lot of interest in the area of material science, medicinal and natural product synthesis and are applied in pharmaceutical and fine chemical industries.[18] Among these, Suzuki-Miyaura involving the coupling between aryl halides and aryl boronic acids has been thoroughly investigated. There are many reports on the Pd nanoparticles catalyzed cross-coupling reaction. M. Lorenzo *et al.* reported the effect of size and shape of Pd-NP for the C–C bond formation.[19] Similarly, El-Sayed *et al.* reported that PVP stabilized Pd nanoparticles is the effective catalyst for the coupling reaction.[20]

In this paper we report the synthesis of PVP stabilized three different size Ni-nanoparticles (Ni-NP) by varying PVP to Ni weight ratio. It has been well known that the rate of reaction per unit catalyst surface vary with particle size. The prepared Ni-nanoparticles were investigated for the selective hydro-

[a] *A. Bathla, Dr. B. Pal*
School of Chemistry and Biochemistry, Thapar Institute of Engineering & Technology, Patiala-147004, India
Fax: +91-175-236-4498
Tel.: +91-175-239-3443
E-mail: bpal@thapar.edu

Supporting information for this article is available on the WWW under https://doi.org/10.1002/slct.201800699

Materials Research Bulletin 116 (2019) 1–7

Contents lists available at ScienceDirect

Materials Research Bulletin

journal homepage: www.elsevier.com/locate/matresbu

Highly efficient $CaCO_3$-CaO extracted from tap water distillation for effective adsorption and photocatalytic degradation of malachite green dye

Aadil Bathla, Deepak Singla, Bonamali Pal*

School of Chemistry and Biochemistry, Thapar Institute of Engineering & Technology, Patiala, 147004, Punjab, India

ARTICLE INFO

Keywords:
Extraction of $CaCO_3$
Water hardness minerals
Adsorption behavior
Photodegradation of malachite green dye
Sun-light photocatalysis

ABSTRACT

The present work demonstrated the extraction, characterization, adsorption and photocatalytic properties of hardness causing minerals obtained from tap water distillation. The resulting white powder material is sintered at different temperature. XRD and EDS analysis revealed that powder residue consists of mainly calcium carbonate ($CaCO_3$) having surface area 35.4 m^2g^{-1} that decomposed to CaO after sintering at 900°C for 4h. This $CaCO_3$ powder displayed effective adsorption and photocatalytic degradation of malachite green dye under sunlight relative to the commercial sample. The impact of different parameters like concentration of dye, amount of catalyst on adsorption and photodegradation was studied in details. The adsorption behavior follows the Freundlich adsorption isotherm and photodegradation process exhibited a higher rate constant of k = 5.1 x 10^{-2} min^{-1}. Therefore, the use of this material could be a greener approach for effective removal and degradation of toxic effluent in wastewater for large-scale industrial applications.

1. Introduction

Water hardness is one of the crucial aspects while designing any sort of industrial or research applications. The different household activities like cooking, washing, and drinking are also affected with water hardness [1–5]. Survey analysis shows [6–10] that the tap water which is mostly used in household activities contains carbonate, bicarbonate, oxides, chlorides, phosphates and sulfates of different metal ions such as Fe^{2+}, Ca^{2+}, Mg^{2+} and Si^{2+}. This results in temporary and permanent hardness of water. After boiling tap water, this hardness causing materials (HCM) get converted to carbonates or mostly deposited as permanent precipitates which lead to scale or slag formation [11–16]. As a consequence, this material clogged water pipes, boilers or containers and badly affects many household and industrial applications. Although this material has several disadvantages, it can be used in various fruitful applications like adsorption, degradation, catalytic and photocatalytic activities [17–19]. Since, this material contains oxides and carbonates of calcium and magnesium which can act as a good adsorbing material for removal or degradation of various organic and inorganic contaminants present in waste water [20–25].

Zhao et *al.* [26] utilized core-shell $CaCO_3$ microspheres as an adsorbent for the removal of anionic dyes from aqueous solution. Zhang et al. [27] reported the degradation of methylene blue and congo red dye using calcium carbonate modified with bentonite (CCB). It was found that CCB exhibited higher adsorption capacity in pH range of 8–10. Similarly, Ameta et al. [28] examined the photocatalytic efficiency of calcium oxide (CaO) for methylene blue degradation and optimized the various parameters like concentration of dye, pH, and light intensity. Owing to their non-toxic nature and abundance, these compounds can potentially serve as precursor material for various applications such as the production of refractory bricks, cosmetics, paper, paints, plastics fireproofing, fire extinguishing compositions, chalk powder, and toothpaste [29–33]. The tap water used in our laboratory (TIET, Patiala, Punjab) also contain a huge amount of HCM powder (0.5–1 g/L) which deposited in the distillation flask is considered as waste and discarded as such. In this context, the present work is designed for beneficial uses of this HCM powder to study its physiochemical properties, adsorption and photocatalytic degradation of malachite green (MG) dye under sunlight radiation. The use of HCM powder for above-mentioned applications can be an economical substitute of currently used photoactive materials as well as a solution for discard related problems.

2. Materials and methods

2.1. Materials

Ethanol (C_2H_5OH), methanol (CH_3OH), and Distilled water were

* Corresponding author.
E-mail address: bpal@thapar.edu (B. Pal).

https://doi.org/10.1016/j.materresbull.2019.04.010
Received 1 January 2019; Received in revised form 4 April 2019; Accepted 4 April 2019
Available online 05 April 2019
0025-5408/

Article

Journal of
Nanoscience and Nanotechnology
Vol. 20, 1–8, 2020
www.aspbs.com/jnn

Morphology Dependent Photocatalytic Activity of CuO/CuO–TiO_2 Nanocatalyst for Degradation Methyl Orange Under Sunlight

Aadil Bathla[1], Rayees Ahmad Rather[2], Tamanna Poonia[1], and Bonamali Pal[1,*]

[1] School of Chemistry and Biochemistry, Thapar Institute of Engineering and Technology, Patiala, India
[2] Department of Chemical Engineering, Hong Kong University of Science and Technology, Hong Kong, China

CuO nanoparticles have been extensively used as a photocatalyst because of their superior activity, selectivity and stability properties. The catalytic efficiency of these oxide nanoparticles can be improved by varying the size and shape of nanoparticles. Here, we report the synthesis of different shaped CuO nanoparticles and their impregnation on TiO_2. Optical analysis revealed that a considerable red shift (420 nm to 550 nm) in absorption spectra of CuO–TiO_2 nanocomposites was observed compared to bare CuO nanoparticles. DLS measurements showed that the average hydrodynamic size of CuO nanostars was increased from 160 nm to 584 nm after deposition on TiO_2. These nanocomposites were examined for photocatalytic degradation of methyl orange under sunlight radiation. It was observed that CuO–TiO_2 nanostars exhibited superior photocatalytic efficiency compared to CuO-nanoneedles, nanocrumbles and bare CuO nanoparticles. The CuO nanoparticles act as co-catalyst on the surface of TiO_2 and alter the physicochemical properties of TiO_2. The higher activity arises due to the fact that the doping of CuO reduces the recombination of charge carries ($e^- - h^+$) and creates the intra-gap states which result in higher absorption of light radiations. Therefore, CuO nanoparticles impregnated on TiO_2 found to be an effective and ideal catalyst for the photodegradation of methyl orange dye.

Keywords: CuO Nanoparticles, Shape-Dependent Photoactivity, CuO–TiO_2 Nanocomposites, Photodegradation of Methyl Orange.

1. INTRODUCTION

Copper oxide (CuO) nanoparticles have attracted considerable attention because of their optical, catalytic, and thermal properties. CuO is a *p*-type semiconductor and widely employed as a promising material for solar cells, bio-sensors, gas-sensors, catalytic and photocatalytic degradation of organic pollutants [1–11]. The physicochemical properties of CuO nanoparticles extremely depend on the size and morphology of the nanostructure. Thus, a small variation in the synthesis and fabrication of CuO leads to enhancement in their photo-catalytic efficiency. Numerous efforts have been employed for the synthesis of CuO of different morphology like nanoflowers, rods, tubes, hollow spheres, and nanowires. Irudayaraj et al. [12] reported the synthesis of CuO nanoneedles by precipitation method using ammonium hydroxide as a complexing agent. Yang et al. [13] reported the formation of hierarchical CuO nanoflowers using one pot water/ethanol solution phase precipitation method and study their application as a glucose biosensor. Wang et al. [14] studied the comparative photocatalytic efficiency of commercial copper oxide and as prepared CuO-nanowires for the degradation of Rhodamine-B (Rh-B) under UV-light irradiations. It was observed that 95% Rhodamine-B was degraded using CuO-nanowires and with commercial CuO the degradation percentage was very small (39%). Similarly, Liu et al. [15] reported the synthesis of CuO-nanoflowers incorporated on reduced graphene oxide and found that CuONF/rGO nanocatalyst exhibited superior photocatalytic activity for the degradation of Rh-B compared to bare CuO-nanoflowers.

Nowadays, the removal of dyes from water sources becomes a major concern because these dyes are carcinogenic in nature. These dyes are main constitutes of

*Author to whom correspondence should be addressed.